1993

Acoustically driven integrated microstrip antennas and electromagnetic radiation from piezoelectric devices

Charles Forrest Campbell
Iowa State University

INFORMATION TO USERS

This manuscript has been reproduced from the microfilm master. UMI films the text directly from the original or copy submitted. Thus, some thesis and dissertation copies are in typewriter face, while others may be from any type of computer printer.

The quality of this reproduction is dependent upon the quality of the copy submitted. Broken or indistinct print, colored or poor quality illustrations and photographs, print bleedthrough, substandard margins, and improper alignment can adversely affect reproduction.

In the unlikely event that the author did not send UMI a complete manuscript and there are missing pages, these will be noted. Also, if unauthorized copyright material had to be removed, a note will indicate the deletion.

Oversize materials (e.g., maps, drawings, charts) are reproduced by sectioning the original, beginning at the upper left-hand corner and continuing from left to right in equal sections with small overlaps. Each original is also photographed in one exposure and is included in reduced form at the back of the book.

Photographs included in the original manuscript have been reproduced xerographically in this copy. Higher quality 6" x 9" black and white photographic prints are available for any photographs or illustrations appearing in this copy for an additional charge. Contact UMI directly to order.

U·M·I

University Microfilms International
A Bell & Howell Information Company
300 North Zeeb Road. Ann Arbor, MI 48106-1346 USA
313/761-4700 800/521-0600

Order Number 9405069

Acoustically driven integrated microstrip antennas and electromagnetic radiation from piezoelectric devices

Campbell, Charles Forrest, Ph.D.

Iowa State University, 1993

U·M·I
300 N. Zeeb Rd.
Ann Arbor, MI 48106

Acoustically driven integrated microstrip antennas and electromagnetic radiation from piezoelectric devices

by

Charles Forrest Campbell

A Dissertation Submitted to the
Graduate Faculty in Partial Fulfillment of the
Requirements for the Degree of
DOCTOR OF PHILOSOPHY

Department: Electrical Engineering and Computer Engineering
Major: Electrical Engineering (Microelectronics)

Approved:

Signature was redacted for privacy.

In Charge of Major Work

Signature was redacted for privacy.

For the Major Department

Signature was redacted for privacy.

For the Graduate College

Iowa State University
Ames, Iowa

1993

TABLE OF CONTENTS

Page

CHAPTER 1. INTRODUCTION

Statement of Problem

As electronics systems become more complex, there will be an increasing need to develop receiver systems that can be completely integrated onto a single semiconductor wafer in order to reduce size and weight, and to enhance reliability. For a receiver system to be considered integrated, both the antenna and the electronic circuitry must be fabricated on the same semiconductor wafer. However, to avoid electromagnetic interference (EMI) problems the electronics would have to be somehow shielded from the antenna. The question then becomes how does one transfer energy between the antenna and circuitry in an integrated system and realize the required electromagnetic shielding. A possible solution is to acoustically couple energy from an antenna on one side of a semiconductor wafer through a conducting ground plane to the electronics on the other side [1]. This could be accomplished with the use of piezoelectrically active thin films that are compatible with integrated circuit processing such as aluminum nitride or zinc oxide. Using this technology, fully integrated receiver systems could be developed where the circuitry is electromagnetically shielded by the ground plane from the environment where the antenna resides. Possible integrated receiver topologies are shown in Fig. 1-1 and Fig. 1-2. The structure shown in Fig. 1-1 is overmoded because of the intervening non-piezoelectric semiconductor layer between the two piezoelectric layers. This arrangement requires a ground plane on both sides of the wafer, and a seal ring at the edge of the wafer to electrically connect the ground planes. A pit has been etched in the structure shown in Fig. 1-2 to remove the intervening semiconductor layer, and the device is therefore fundamental mode. Note that for the arrangement shown in Fig. 1-2 only one ground plane is required.

The theory of operation is as follows: the received signal excites a potential difference between the microstrip antenna and the ground plane which generates an acoustic wave in the piezoelectric material. The sound wave propagates through the ground plane and semiconductor into the second piezoelectric layer on the electronics side. Via the piezoelectric effect, a potential difference will be formed between the conductor which is connected to the circuitry and the ground

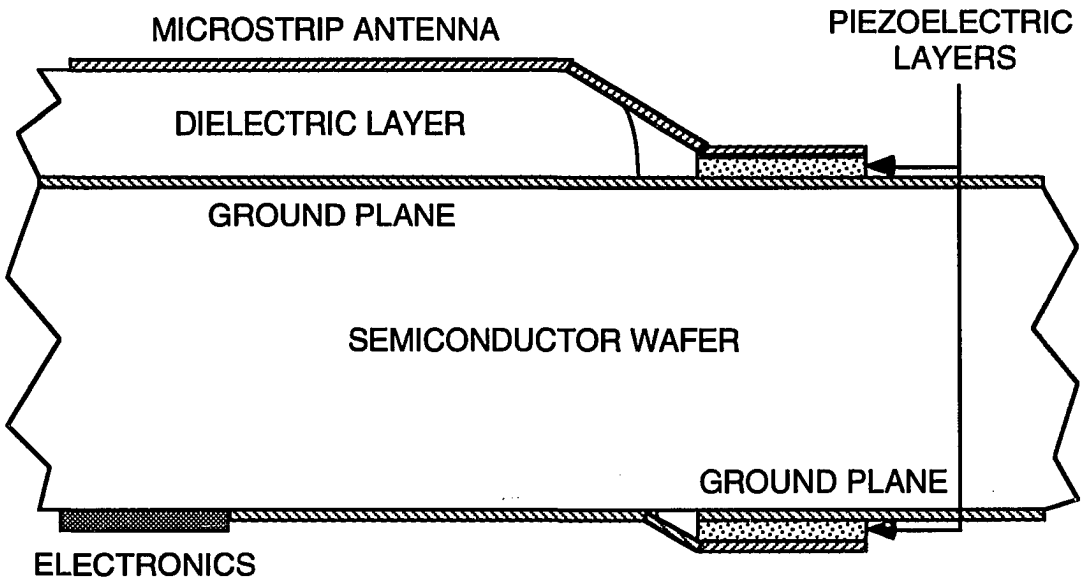

Figure 1-1. Overmoded integrated receiver system concept

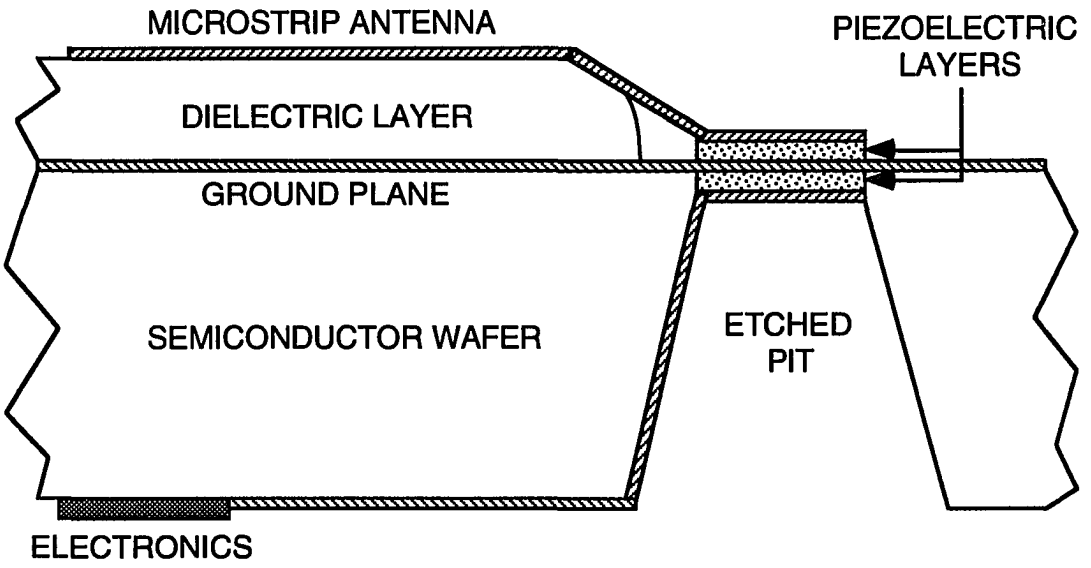

Figure 1-2. Fundamental mode integrated receiver system concept.

plane on the electronics side of the wafer. Thus, energy is transferred from the antenna to the electronics acoustically. However, the signal will only be strongly transmitted through the wafer at frequencies where the acoustic path length is an integer multiple of a half acoustic wavelength long. So the arrangements shown in Fig. 1-1 and Fig. 1-2 not only transmit the signal through the wafer but also realize the narrow bandpass filter which is required after the antenna for many types of receiver systems [2]. This type of filter structure is called a stacked crystal filter (SCF) and is manufactured at the Microelectronics Research Center (MRC) at microwave frequencies [3,4,5,6].

On the radiating side of the structure resides a microstrip antenna and a bulk acoustic wave (BAW) piezoelectric transducer. To study the feasibility of such a system, the performance of microstrip antennas with thin substrates and metalizations needs to be investigated. Like the microstrip antenna, the piezoelectric transducer is a resonant device and its electromagnetic radiation characteristics must also be determined. The topology of the piezoelectric transducer is similar to that of a microstrip antenna. Thus, the structure to be used to study electromagnetic radiation from bulk acoustic wave devices is essentially a microstrip antenna with a piezoelectric substrate as shown in Fig. 1-3.

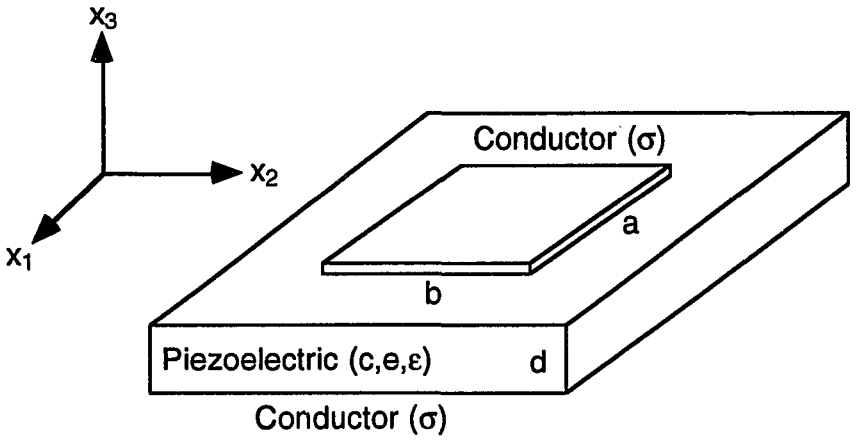

Figure 1-3. Bulk acoustic wave device.

The purpose of this work is therefore two fold, first, to investigate electromagnetic radiation from the structure shown in Fig. 1-3, and second, to study the feasibility and optimum configuration of the integrated antenna topologies shown in Fig. 1-1 and Fig. 1-2.

Review of Past Work

Piezoelectric devices have been analyzed by a variety of methods. For devices which may be considered one dimensional, the displacement fields are restricted to three modes; one longitudinal and two shear. Seven-port network models have been developed to describe this situation. One of the ports is electrical and the remaining six mechanical; an input and output port for each mode [3,4,5]. This model consists of transmission lines, ideal transformers and capacitors, and is equivalent to solving the coupled boundary value problem. If only one mode exists, the seven-port network model reduces to the well known Mason model for a piezoelectric layer [7,8]. Higher dimensional devices have been analyzed with finite difference methods [9,10,11,12] , Green's functions [13], variational techniques [13,14] , and finite element methods [15,16,17,18]. These methods, however, assume no electromagnetic radiation, require substantial computer power, and are just now starting to become practical for the analysis of useful devices. See Appendix A for a reprint of a paper presented at the *1992 IEEE Ultrasonics Symposium* which describes a two dimensional finite difference method for the analysis of piezoelectric devices [12].

Microstrip antennas have been modeled by many methods with varying degrees of success. Probably the simplest model is the transmission line model where the microstrip antenna is assumed to behave like a section of transmission line [19,20,21]. The radiation losses are modeled by impedances that load the line, fringing is accounted for by slightly lengthening the line, and mutual coupling between the ends is represented by feedback networks. The model can predict the input impedance of the antenna for modes that are effectively one dimensional (TM_{01} or TM_{02} ,etc.). However, the model does not predict the radiated fields for the antenna nor can it handle two dimensional modes or circular polarization. Therefore, the transmission line model is not sufficient for the purposes of this study.

An exact representation may be obtained from the mixed potential integral equation for stratified media where the Green's functions involve Sommerfeld type integrals that must be evaluated on the real axis [19,20]. To actually obtain numerical results the integral equation must be approximated numerically by moment methods. This method, though very accurate, is difficult to implement and provides more information than is required to solve the problem at hand.

A good compromise between accuracy and ease of implementation is provided by the cavity model [19,21,22,23]. The cavity model is two dimensional, capable of handling circular polarization and predicting the radiated fields of the antenna. In the cavity model it is assumed that the antenna can be replaced by a cavity of the same size with perfect magnetic walls on the sides and perfect electric walls along the top and the bottom. The fields inside of the cavity may be solved for by planar circuit techniques and the surface equivalence principle is applied to compute the radiated fields [24,25,26]. The cavity model will be used in this work to analyze the radiation and impedance characteristics of the antennas to be investigated.

Some prior work of note has been done on radiation from piezoelectric crystals. Mindlin and Lee computed the radiated power from rotated quartz plates at thickness mode frequencies [27,28,29]. In the calculation, a quartz plate of infinite lateral extent is subjected to a lateral AC electric field or harmonic stress. The electric fields in the plate are then computed assuming no radiation, and traveling wave electric fields are assumed to exist in the free space above and below the plate. The amplitudes of the traveling wave fields are found by matching boundary conditions at the free space-piezoelectric interface. The purpose of the study was to compute the power lost to electromagnetic radiation from the face of a bare piezoelectric crystal in order to find the rotated crystal cut with the least radiation. The results would be useful for predicting the radiated power loss from surface acoustic wave (SAW) devices. The calculations involve no conductors and cannot be used to predict the radiation characteristics of bulk acoustic wave (BAW) devices. The work being proposed here therefore differs from the prior work of Mindlin and Lee in that a bulk acoustic wave device is being analyzed as a microstrip antenna with a piezoelectric substrate.

CHAPTER 2. PIEZOELECTRIC DEVICE THEORY

Coupled Wave Theory

The analysis of a microstrip antenna with a piezoelectric substrate requires the calculation of both electromagnetic and acoustic fields under the conducting patch. Since in a piezoelectric material these quantities are coupled, strictly speaking the coupled wave equations would have to be rigorously solved. This would require a numerical method and large amounts of computer power. Fortunately, due to the large differences between the velocity of sound and the velocity of light in the medium, greatly simplifying approximations may be made without seriously affecting the accuracy of the results. In this section the formal coupled wave theory of piezoelectricity is presented, and simplifying assumptions are stated and justified.

The fundamental laws of acoustics in matrix form are [8]

$$\text{Newton's law :} \quad \nabla \cdot \mathbf{T} = \rho \frac{\partial \mathbf{v}}{\partial t} \tag{2.1}$$

$$\text{Definition of strain :} \quad \nabla_s \mathbf{v} = \frac{\partial \mathbf{S}}{\partial t} \tag{2.2}$$

where the acoustic field variables are defined as

$$\text{Stress } (N/m^2): \quad \mathbf{T} = [\, T_1 \quad T_2 \quad T_3 \quad T_4 \quad T_5 \quad T_6 \,]^T$$

$$\text{Displacement (m)}: \quad \mathbf{u} = [\, u_1 \quad u_2 \quad u_3 \,]^T$$

$$\text{Strain (m/m)}: \quad \mathbf{S} = \nabla_s \mathbf{u} = [\, S_1 \quad S_2 \quad S_3 \quad S_4 \quad S_5 \quad S_6 \,]^T$$

$$\text{Velocity (m/S)}: \quad \mathbf{v} = \frac{\partial \mathbf{u}}{\partial t} = [\, v_1 \quad v_2 \quad v_3 \,]^T$$

The superscript T indicates transpose and the mass density is ρ (kg/m^3). The matrix divergence and gradient operators in rectangular coordinates are

$$(\nabla\cdot)^T = \nabla_s = \begin{bmatrix} \frac{\partial}{\partial x_1} & 0 & 0 \\ 0 & \frac{\partial}{\partial x_2} & 0 \\ 0 & 0 & \frac{\partial}{\partial x_3} \\ 0 & \frac{\partial}{\partial x_3} & \frac{\partial}{\partial x_2} \\ \frac{\partial}{\partial x_3} & 0 & \frac{\partial}{\partial x_1} \\ \frac{\partial}{\partial x_2} & \frac{\partial}{\partial x_1} & 0 \end{bmatrix}. \tag{2.3}$$

The governing equations of electromagnetism are Maxwell's equations which for source-free lossless media are as follows:

$$\text{Faraday's law :} \quad \nabla \times \mathbf{E} = -\frac{\partial \mathbf{B}}{\partial t} \tag{2.4}$$

$$\text{Ampere's law :} \quad \nabla \times \mathbf{H} = \frac{\partial \mathbf{D}}{\partial t} \tag{2.5}$$

$$\text{Gauss's law :} \quad \nabla\cdot\mathbf{D} = 0 \tag{2.6}$$

$$\text{Gauss's law :} \quad \nabla\cdot\mathbf{B} = 0 \tag{2.7}$$

where the electromagnetic field variables are

Electric field (V/m) : $\mathbf{E} = [\, E_1 \quad E_2 \quad E_3 \,]^T$

Electric flux density (C/m^2) : $\mathbf{D} = [\, D_1 \quad D_2 \quad D_3 \,]^T$

Magnetic field (A/m) : $\mathbf{H} = [\, H_1 \quad H_2 \quad H_3 \,]^T$

Magnetic flux density (Wb/m^2) : $\mathbf{B} = [\, B_1 \quad B_2 \quad B_3 \,]^T$.

The curl matrix operator in rectangular coordinates is

$$\nabla x = \begin{bmatrix} 0 & -\frac{\partial}{\partial x_3} & \frac{\partial}{\partial x_2} \\ \frac{\partial}{\partial x_3} & 0 & -\frac{\partial}{\partial x_1} \\ -\frac{\partial}{\partial x_2} & \frac{\partial}{\partial x_1} & 0 \end{bmatrix}. \tag{2.8}$$

In a piezoelectric medium the acoustic and electromagnetic laws are coupled through the constitutive relations

$$\mathbf{T} = \mathbf{c}^E : \mathbf{S} - \mathbf{e}^T : \mathbf{E} \tag{2.9}$$

$$\mathbf{D} = \varepsilon^S : \mathbf{E} + \mathbf{e} : \mathbf{S} \tag{2.10}$$

$$\mathbf{B} = \mu\, \mathbf{H}$$

where the colons indicate a matrix multiplication. The tensors which characterize the material in contracted notation are

Piezoelectric stress matrix (C/m^2) : $\mathbf{e} = \begin{bmatrix} e_{11} & e_{12} & e_{13} & e_{14} & e_{15} & e_{16} \\ e_{21} & e_{22} & e_{23} & e_{24} & e_{25} & e_{26} \\ e_{31} & e_{32} & e_{33} & e_{34} & e_{35} & e_{36} \end{bmatrix}$

$$\text{Stiffness matrix (N/m}^2\text{)}: \quad \mathbf{c}^E = \begin{bmatrix} c_{11} & c_{12} & c_{13} & c_{14} & c_{15} & c_{16} \\ c_{21} & c_{22} & c_{23} & c_{24} & c_{25} & c_{26} \\ c_{31} & c_{32} & c_{33} & c_{34} & c_{35} & c_{36} \\ c_{41} & c_{42} & c_{43} & c_{44} & c_{45} & c_{46} \\ c_{51} & c_{52} & c_{53} & c_{54} & c_{55} & c_{56} \\ c_{61} & c_{62} & c_{63} & c_{64} & c_{65} & c_{66} \end{bmatrix}$$

$$\text{Permittivity matrix (F/m)}: \quad \varepsilon^S = \begin{bmatrix} \varepsilon_{11} & \varepsilon_{12} & \varepsilon_{13} \\ \varepsilon_{21} & \varepsilon_{22} & \varepsilon_{23} \\ \varepsilon_{31} & \varepsilon_{32} & \varepsilon_{33} \end{bmatrix}.$$

Since the material is assumed to be non-magnetic; $\mu = 4\pi \times 10^{-7}$ H/m. The superscripts E and S mean under constant electric field and constant strain respectively.

From these relations the following wave equations may be derived:

$$-\nabla \times \nabla \times \mathbf{E} = \mu \varepsilon^S : \frac{\partial^2 \mathbf{E}}{\partial t^2} + \mu \mathbf{e} : \nabla_s \left(\frac{\partial \mathbf{v}}{\partial t} \right) \tag{2.11}$$

$$\nabla \cdot \mathbf{c}^E : \nabla_s \mathbf{v} = \rho \frac{\partial^2 \mathbf{v}}{\partial t^2} + \nabla \cdot \mathbf{e}^T : \frac{\partial \mathbf{E}}{\partial t} . \tag{2.12}$$

It is convenient to apply Helmholtz's theorem and separate the electric field into rotational and irrotational parts [8]

$$\mathbf{E} = \mathbf{E}^r - \nabla \phi \tag{2.13}$$

where the rotational part satisfies the Coulomb gauge.

$$\nabla \cdot \mathbf{E}^r = 0$$

Substituting Eq. (2.13) into the wave equations (2.11) and (2.12):

$$- \nabla \times \nabla \times \mathbf{E}^r = \mu \overset{S}{\varepsilon} : \frac{\partial^2 \mathbf{E}^r}{\partial t^2} - \mu \overset{S}{\varepsilon} : \nabla \frac{\partial^2 \phi}{\partial t^2} + \mu \mathbf{e} : \nabla_s \left(\frac{\partial \mathbf{v}}{\partial t} \right) \tag{2.14}$$

$$\nabla \cdot \mathbf{c}^E : \nabla_s \mathbf{v} = \rho \frac{\partial^2 \mathbf{v}}{\partial t^2} + \nabla \cdot \mathbf{e} : \frac{\partial \mathbf{E}^r}{\partial t} - \nabla \cdot \mathbf{e}^T : \nabla \frac{\partial \phi}{\partial t} . \tag{2.15}$$

The wave equations (2.14) and (2.15) precisely describe wave phenomena in piezoelectric material.

The first simplification one normally uses in piezoelectric device analysis is called the quasi-static approximation. To illustrate this, assume that constant amplitude fields are traveling in the x_1-direction in a 6mm hexagonal crystal such that the fields are proportional to

$$e^{j(\omega t - kx_1)}$$

and the partial derivative operators become

$$\frac{\partial}{\partial x_1} = - jk \qquad \frac{\partial}{\partial t} = j\omega \qquad \frac{\partial}{\partial x_3} = \frac{\partial}{\partial x_2} = 0 .$$

Materials such as aluminum nitride and zinc oxide crystallize in this lattice, and the material tensors are of the form

$$\mathbf{c}^E = \begin{bmatrix} c_{11} & c_{12} & c_{13} & 0 & 0 & 0 \\ c_{12} & c_{11} & c_{13} & 0 & 0 & 0 \\ c_{13} & c_{13} & c_{33} & 0 & 0 & 0 \\ 0 & 0 & 0 & c_{44} & 0 & 0 \\ 0 & 0 & 0 & 0 & c_{44} & 0 \\ 0 & 0 & 0 & 0 & 0 & c_{66} \end{bmatrix}$$

$$\mathbf{e} = \begin{bmatrix} 0 & 0 & 0 & 0 & e_{15} & 0 \\ 0 & 0 & 0 & e_{15} & 0 & 0 \\ e_{31} & e_{31} & e_{33} & 0 & 0 & 0 \end{bmatrix}$$

$$\varepsilon^{S} = \begin{bmatrix} \varepsilon_{11} & 0 & 0 \\ 0 & \varepsilon_{11} & 0 \\ 0 & 0 & \varepsilon_{33} \end{bmatrix}.$$

Carrying out the indicated operations the wave equations in matrix form are

$$\begin{bmatrix} \omega^2 \mu \varepsilon_{11} & 0 & 0 \\ 0 & \omega^2 \mu \varepsilon_{11} - k^2 & 0 \\ 0 & 0 & \omega^2 \mu \varepsilon_{33} - k^2 \end{bmatrix} \mathbf{E}^r = -j\omega^2 \mu k \begin{bmatrix} \varepsilon_{11} \phi \\ 0 \\ 0 \end{bmatrix} + \omega k \mu \begin{bmatrix} e_{15} v_3 \\ 0 \\ e_{31} v_1 \end{bmatrix}$$

$$\begin{bmatrix} \omega^2 \rho - c_{11} k^2 & 0 & 0 \\ 0 & \omega^2 \rho - c_{66} k^2 & 0 \\ 0 & 0 & \omega^2 \rho - c_{44} k^2 \end{bmatrix} \mathbf{v} = \omega k \begin{bmatrix} e_{31} E_3^r \\ 0 \\ e_{15} E_1^r \end{bmatrix} + j\omega k^2 \begin{bmatrix} 0 \\ 0 \\ e_{15} \phi \end{bmatrix}.$$

From the Coulomb gauge

$$E_1^r = 0$$

and from the first wave equation

$$\phi = \frac{e_{15}}{j\omega \varepsilon_{11}} v_3 \quad . \tag{2.16}$$

The remaining components of the wave equations yield the following dispersion relations:

$$(\omega^2 \mu \varepsilon_{11} - k^2) E_2^r = 0$$

$$(\omega^2 \rho - c_{66} k^2) v_2 = 0$$

$$(\omega^2 \rho - c_{44}k^2)\, v_3 = j\omega\, k^2 e_{15}\, \phi \quad \rightarrow \text{Eq. (2.16)} \rightarrow \quad (\omega^2 \rho - [c_{44} + e_{15}^2 / \varepsilon_{11}]\, k^2)\, v_3 = 0$$

$$(\omega^2 \rho - c_{11}k^2)\, v_1 = (e_{31}\, \omega\, k)\, E_3^r$$

$$(\omega\, k\, \mu\, e_{31})\, v_1 = (\omega^2 \mu\, \varepsilon_{33} - k^2)\, E_3^r \,.$$

The first two dispersion relations are for a purely electromagnetic wave and purely acoustic wave respectively. Piezoelectricity does not have an effect on these waves. The third equation is a purely acoustic wave, however the elastic constant has been replaced by a "piezoelectrically stiffened" elastic constant inside of the square brackets. The hybrid waves described by the remaining dispersion equations are called quasi-acoustic and quasi-electromagnetic waves. The piezoelectric coupling causes the wave numbers of these waves to be perturbed. Eliminating one of the variables gives

$$(\omega^2 \rho - c_{11}\, k^2)\, (\omega^2 \mu\, \varepsilon_{33} - k^2) = \mu\, e_{31}^2\, \omega^2 k^2 \,. \qquad (2.17)$$

This equation has two roots for k^2 which are the wave numbers of the quasi-acoustic and quasi-electromagnetic waves. For example, the relevant material constants for aluminum nitride are [30]:

$$c_{11} = 345 \times 10^9 \ \text{N/m}^2$$
$$e_{31} = -0.58 \ \text{C/m}^2$$
$$\varepsilon_{33} = 9.5 \times 10^{-11} \ \text{F/m}$$
$$\rho = 3270 \ \text{kg/m}^3 \,.$$

The wave numbers for the hybrid waves are found to be

$$k_{QA}^2 = 3.74186740820 \times 10^{11} \ (\text{rad/m})^2$$
$$k_{QE}^2 = 4.7129540548 \times 10^3 \ (\text{rad/m})^2 \,.$$

The wave numbers for pure acoustic and electromagnetic waves are

$$k_A^2 = 3.74186740772 \times 10^{11} \text{ (rad/m)}^2$$
$$k_E^2 = 4.7129540554 \times 10^{3} \text{ (rad/m)}^2 .$$

Note that difference between the hybrid wave numbers and pure wave numbers is very small which means that piezoelectricity has a negligible effect on EM and acoustic wave propagation. This is an important result because electromagnetic wave propagation can then be handled with electromagnetic theory and acoustic wave propagation with acoustic theory provided that the piezoelectrically stiffened constants are used where required. In other words, the rotational part of the electric field may be assumed to be zero when computing acoustic fields. This is the quasi-static approximation for piezoelectric device analysis [7,8]. The acoustic waves and potential field ϕ are piezoelectrically coupled through Eq. (2.16).

One Dimensional Piezoelectric Device Analysis

Under the quasi-static approximation discussed in the coupled wave theory section, the acoustic problem may be solved separately from the electromagnetic problem. For actual device analysis, engineering notation is usually easier to work with than the matrix form of the fundamental laws. The AC steady-state, quasi-static equations of linear piezoelectricity in engineering notation are:

$$\text{Newton's law}: \quad \frac{\partial T_{ij}}{\partial x_i} = -\rho\omega^2 u_j \tag{2.18}$$

$$\text{Gauss's law}: \quad \frac{\partial D_i}{\partial x_i} = 0 \tag{2.19}$$

and the constitutive relations

$$T_{ij} = c_{ijkl}\frac{\partial u_k}{\partial x_l} + e_{kij}\frac{\partial \phi}{\partial x_k} \tag{2.20}$$

$$D_i = e_{ikl}\frac{\partial u_k}{\partial x_l} - \varepsilon_{ik}\frac{\partial \phi}{\partial x_k}\,. \tag{2.21}$$

The repeated subscripts imply summation (i,j,k,l = 1,2,3), and the connection between engineering notation and matrix notation is summarized in Table 2-1.

Table 2-1. Relationship between engineering and matrix notation

Engineering	Matrix
11	1
22	2
33	3
23,32	4
13,31	5
12,21	6

Using 2D and 3D finite element methods, Lerch determined that for a piezoelectric resonator if a dimension was at least 10 times larger than any other dimension, it would not significantly change the resonant frequency of the device and could be neglected [16]. Thus, If the x_1 and x_2 dimensions are much greater then the x_3 dimension, the device may be assumed to be one dimensional. In other words, no variation of the fields is permitted in the x_1 and x_2 directions and all derivatives in those directions will be zero. Under these assumptions the piezoelectric device equations reduce to the following:

$$\frac{dT_{3j}}{dx_3} = -\rho\omega^2 u_j \tag{2.22}$$

$$\frac{dD_3}{dx_3} = 0 \tag{2.23}$$

$$T_{3j} = c_{3jk3} \frac{du_k}{dx_3} + e_{33j} \frac{d\phi}{dx_3} \tag{2.24}$$

$$D_3 = e_{3k3} \frac{du_k}{dx_3} - \varepsilon_{33} \frac{d\phi}{dx_3} . \tag{2.25}$$

Substituting Eq. (2.25) into Eq. (2.23) and integrating twice, the potential is

$$\phi = \frac{e_{3k3}}{\varepsilon_{33}} u_k + \Gamma x_3 + \Delta \tag{2.26}$$

where Γ and Δ are arbitrary constants of integration. From Eq. (2.24) and Eq. (2.26) the stress may be written as

$$T_{3j} = \bar{c}_{3jk3} \frac{du_k}{dx_3} + e_{33j} \Gamma \tag{2.27}$$

where the stiffened elastic constant is

$$\bar{c}_{3jk3} = c_{3jk3} + \frac{e_{33j} e_{3k3}}{\varepsilon_{33}} .$$

Substituting Eq. (2.27) into Eq. (2.22) and expanding j,k=1,2,3 results in the following set of coupled wave equations:

$$\bar{c}_{3113} \frac{d^2u_1}{dx_3^2} + \bar{c}_{3123} \frac{d^2u_2}{dx_3^2} + \bar{c}_{3133} \frac{d^2u_3}{dx_3^2} + \rho\omega^2 u_1 = 0 \tag{2.28a}$$

$$\bar{c}_{3213}\frac{d^2u_1}{dx_3^2}+\bar{c}_{3223}\frac{d^2u_2}{dx_3^2}+\bar{c}_{3233}\frac{d^2u_3}{dx_3^2}+\rho\omega^2 u_2=0 \tag{2.28b}$$

$$\bar{c}_{3313}\frac{d^2u_1}{dx_3^2}+\bar{c}_{3323}\frac{d^2u_2}{dx_3^2}+\bar{c}_{3333}\frac{d^2u_3}{dx_3^2}+\rho\omega^2 u_3=0 \tag{2.28c}$$

Expanding Eq. (2.26) for k=1,2,3, the potential is equal to

$$\phi=\frac{e_{313}}{\varepsilon_{33}}u_1+\frac{e_{323}}{\varepsilon_{33}}u_2+\frac{e_{333}}{\varepsilon_{33}}u_3+\Gamma x_3+\Delta \tag{2.29}$$

Substituting Eq. (2.29) into (2.25) the electric flux density is a constant given by

$$D_3=-\varepsilon_{33}\Gamma \tag{2.30}$$

The arbitrary constants Γ and Δ will be nonzero only in the presence of an externally applied potential. If there is no externally applied potential then Γ and Δ will be equal to zero, and the relationship between the potential and acoustic fields Eq. (2.29) will then be of the same form as Eq. (2.16). In other words there will be a nonzero electric field traveling along with the acoustic wave, but the electric flux density will vanish because Γ=0. To be more specific, the dot product of the acoustically generated electric field and electric flux density is zero. However, a nonzero electric flux density vector may exist orthogonal to the acoustically generated electric field. This means that the electric energy density is zero, and that energy may not be transferred between the acoustic and electric field unless an external electric flux density field is applied parallel to the acoustically generated electric field [7].

As can be seen from Eq. (2.28), the one dimensional wave equations predict the existence of three propagating modes: one longitudinal and two shear. Eq. (2.28) is the set of differential equations that must be solved in one dimensional piezoelectric device analysis. In the following sections comprising this chapter, the one dimensional equations will be solved for device geometries

of interest. These solutions are required to facilitate the analysis of the structures discussed in the introduction of this thesis.

Fundamental Mode Resonator Analysis

A fundamental mode resonator consists of a one dimensional slab of piezoelectric material and perfectly conducting electrodes of area A. The conductors, assumed to be massless and of zero thickness, are applied to each face of the device as shown in Fig. 2-1. The acoustic wave is assumed to travel in the x_3 direction, and the device is a thickness mode resonator. An x_3-directed external field is applied via the conductors. Since the acoustic wave travels in the same direction as the externally applied field and the acoustically generated electric flux density field must be zero; the electric flux density in the device must be totally supplied by the applied field.

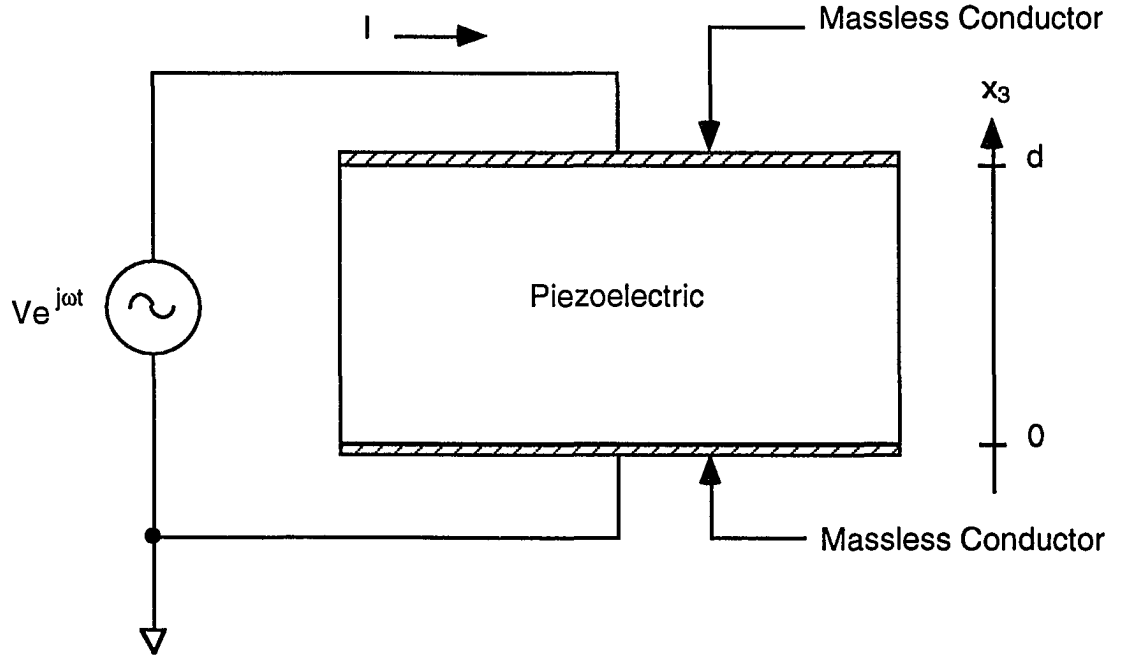

Figure 2-1. Fundamental mode bulk acoustic wave resonator

The current flowing into the device is related to the electric flux density by

$$I = \int_A \mathbf{J}\cdot d\mathbf{S} = -j\omega \int_A D_3 \, dS = j\omega\varepsilon_{33}A\Gamma \tag{2.31}$$

where the minus sign appears because differential vector $d\mathbf{S}$ is directed normally out of the top surface. Solving for Γ one obtains

$$\Gamma = \frac{I}{j\omega\varepsilon_{33}A} . \tag{2.32}$$

Thus, in a thickness mode resonator, the independent variable is the input current and the dependent variable is the potential difference across the device [7]. Eq. (2.32) is a boundary condition equation for the resonator problem. The remaining boundary conditions required to uniquely describe the device are ascertained from the assumption that the resonator is surrounded by air. Air provides a negligibly small restoring force, and traction-free boundary conditions may be applied to the top and bottom surfaces of the device. Mathematically, to satisfy the traction-free boundary conditions

$$T_{3j} = 0 \tag{2.33}$$

must be enforced at the top and bottom surfaces of the resonator.

In a one dimensional bulk acoustic wave resonator, one is normally interested in the characteristics of only one of the three possible propagating modes. Assuming that the modes are non-degenerate and weakly coupled, the coupled set of wave equations given in Eq. (2.28) may be approximately decoupled as

$$-c_{55}\frac{d^2u_1}{dx_3^2} + \rho\omega^2 u_1 = 0 \tag{2.34a}$$

$$\bar{c}_{44} \frac{d^2 u_2}{dx_3^2} + \rho\omega^2 u_2 = 0 \tag{2.34b}$$

$$\bar{c}_{33} \frac{d^2 u_3}{dx_3^2} + \rho\omega^2 u_3 = 0 \tag{2.34c}$$

where the matrix notation has again been employed. The stress equations reduce to

$$T_{31} = \bar{c}_{55} \frac{du_1}{dx_3} + e_{35}\,\Gamma \tag{2.35a}$$

$$T_{32} = \bar{c}_{44} \frac{du_2}{dx_3} + e_{34}\,\Gamma \tag{2.35b}$$

$$T_{33} = \bar{c}_{33} \frac{du_3}{dx_3} + e_{33}\,\Gamma \tag{2.35c}$$

For example, assume that the only mode excited is the longitudinal thickness mode. For this mode, the governing differential equation is Eq. (2.34c) and the stress field is given by Eq. (2.35c). To simplify the notation drop the subscripts and define the following:

$$u = u_3$$
$$x = x_3$$
$$e = e_{33}$$
$$\varepsilon = \varepsilon_{33}$$
$$c = \bar{c}_{33}$$

from which the acoustic wave number is given by

$$k^2 = \rho\omega^2 / c \tag{2.36}$$

The governing differential equation is then

$$\frac{d^2u}{dx^2} + k^2 u = 0 \tag{2.37}$$

and the potential function is

$$\phi = (e / \varepsilon)\, u + \Gamma x + \Delta \,. \tag{2.38}$$

Since the bottom plate is grounded,

$$\phi(0) = 0 \,. \tag{2.39}$$

The general wave solutions to Eq. (2.37) are

$$u(x) = A \cos kx + B \sin kx \tag{2.40}$$

$$\phi(x) = (e/\varepsilon)\, A \cos kx + (e/\varepsilon)\, B \sin kx + \Gamma x + \Delta \tag{2.41}$$

$$T(x) = -ck\, A \sin kx + ck\, B \cos kx + e\, \Gamma \tag{2.42}$$

where A, B and Δ are arbitrary constants and are found from the boundary conditions. For an input current I, Γ is given by Eq. (2.32), and by applying the boundary condition equations at x=0 and x=d one obtains the following system of equations for the arbitrary constants:

$$\phi(0) = (e/\varepsilon)\, A + \Delta = 0$$

$$T(0) = ck\, B + e\, \Gamma = 0$$

$$T(d) = -\, ck\, A \sin kd + ck\, B \cos kd + e\, \Gamma = 0 \,.$$

The solution to this system is

$$A = \frac{el \tan \theta}{j\omega\varepsilon Ack} \tag{2.43a}$$

$$B = -\frac{el}{j\omega\varepsilon Ack} \tag{2.43b}$$

$$\Delta = -\frac{\kappa^2 \tan \theta}{k} \,. \tag{2.43c}$$

The electromechanical coupling coefficient is defined as

$$\kappa^2 = \frac{e^2}{\varepsilon c} \tag{2.44}$$

and the half phase across the device is

$$\theta = \frac{kd}{2} \,.$$

Solutions for the variables of state are then

$$u(x) = -\frac{el}{j\omega\varepsilon Ack}\left[\frac{\sin (kx - \theta)}{\cos \theta}\right] \tag{2.45a}$$

$$\phi(x) = \frac{l}{j\omega\varepsilon A}\left[x - \frac{\kappa^2}{k}\frac{\sin (kx - \theta) + \sin \theta}{\cos \theta}\right] \tag{2.45b}$$

$$E(x) = -\nabla\phi = \frac{-l}{j\omega\varepsilon A}\left[1 - \kappa^2 \frac{\cos (kx - \theta)}{\cos \theta}\right] . \tag{2.45c}$$

The potential difference across the resonator is found from Eq. (2.45b).

$$V = \phi(d) = \frac{Id}{j\omega\varepsilon A}\left[1 - \kappa^2 \frac{\tan\theta}{\theta}\right]. \tag{2.46}$$

The impedance of the resonator is then

$$Z = \frac{V}{I} = \frac{1}{j\omega C_o}\left[1 - \kappa^2 \frac{\tan\theta}{\theta}\right] \tag{2.47}$$

where C_o is the parallel plate capacitance of the device.

$$C_o = \frac{\varepsilon A}{d}$$

Series resonance is defined as the frequencies where Eq. (2.47) is equal to zero and may be found by solving the transcendental equation

$$\theta = \kappa^2 \tan\theta \,. \tag{2.48}$$

Parallel resonance is where Eq. (2.47) becomes infinite which occurs when

$$\theta = \frac{n\pi}{2} \qquad n = 1,3,5,... \tag{2.49}$$

Note that the impedance of the resonator is capacitive until series resonance and then is inductive for the region between series and parallel resonance. This inductive region is where the device is most useful generating large amounts of inductance for high-Q applications. Shown in Fig. 2-2 is the measured impedance locus for a fundamental mode aluminum nitride resonator that was fabricated at the MRC. The device consists of 400μm x 400μm aluminum

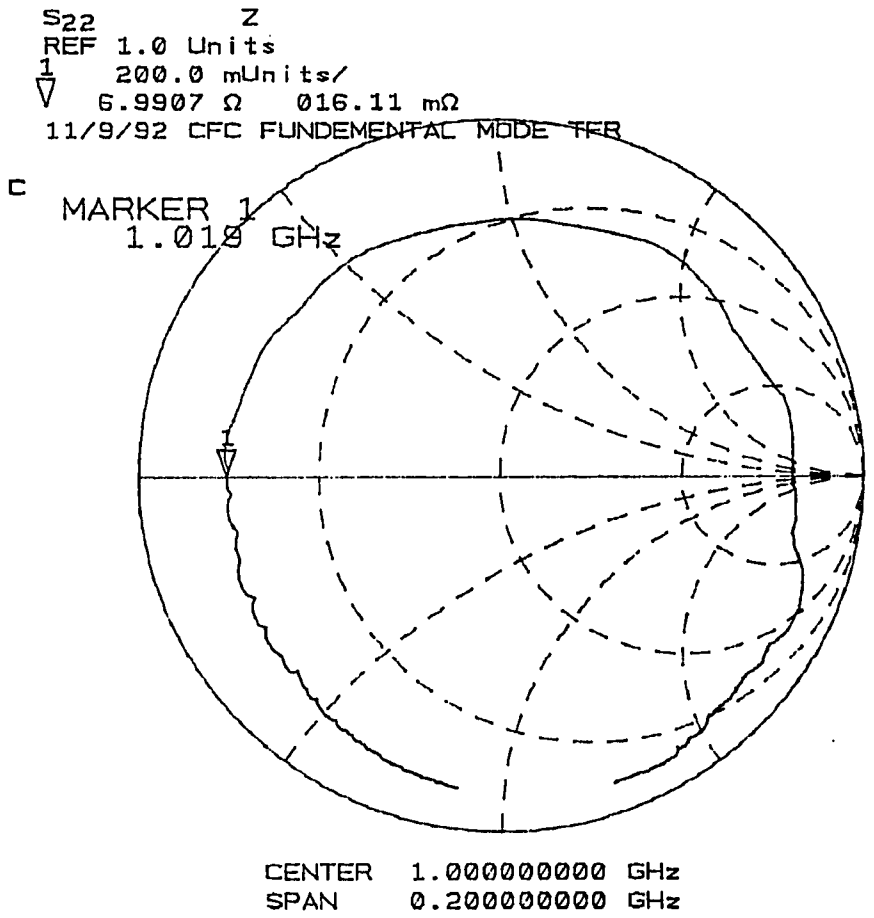

Figure 2-2. Measured fundamental mode AlN resonator impedance

conductors and a c-axis directed aluminum nitride film of a nominal thickness of 5μm. The series and parallel resonances were measured to be 1.0190 GHz and 1.0485 GHz respectively. Upon inspection of Fig. 2-2, some features of the measured data differ from what would be predicted by Eq. (2.47). First, if the material were lossless the impedance would be purely imaginary and the impedance locus would follow the edge of the Smith chart. In reality there are losses which may be represented by allowing the permittivity and elastic constants to become complex [13].

$$\hat{\varepsilon} = \varepsilon (1 - j\tan\delta) \tag{2.50}$$

$$\hat{c} = c + j\omega\eta \tag{2.51}$$

The dielectric loss tangent is $\tan\delta$ and η is the viscosity of the medium. Also evident in Fig. 2-2 are the small resonances which give the curve a rough appearance. These spurious resonances appear due to the finite width dimensions of the device, and will not be predicted by a one dimensional theory. The two and three dimensional numerical techniques discussed in Chapter 1 and Appendix A do however predict the phenomena.

With the exception of the spurious resonances, this device may still be modeled with the one dimensional theory presented in this section. The aluminum nitride material constants required to characterize the longitudinal, x_3-dependent thickness mode are [30]:

$$c_{33} = 395 \times 10^9 \text{ N/m}^2$$
$$e_{33} = 1.55 \text{ C/m}^2$$
$$\varepsilon_{33} = 9.5 \times 10^{-11} \text{ F/m}$$
$$\rho = 3270 \text{ Kg/m}^3$$

To improve the agreement with the experimentally observed resistance of 466Ω at parallel resonance, the elastic and permittivity constants were given the following imaginary parts.

$$\hat{c}_{33} = (395 + j1.0) \times 10^{9} \text{ N/m}^2$$
$$\hat{\varepsilon}_{33} = (9.5 - j0.25) \times 10^{-11} \text{ F/m}$$

From Eq. (2.49) with n=1 and the measured parallel resonance at 1.0485 GHz, the effective thickness of the device is about 5.41μm. From the location of the series resonance at 1.0190 GHz and Eq. (2.48), the electromechanical coupling constant is found to be about κ^2=0.068. This compares well with the value of κ^2=0.060 computed from Eq. (2.44). The devices fabricated at the MRC are characterized with Cascade Microtech coplanar waveguide wafer probes, and the electrical connection to the ground plane is via capacitive coupling. The fringing capacitance between the center conductor which connects to the top plate of the resonator and the surrounding ground plane may be accounted for by increasing the resonator area. It was found that agreement between measurement and theory could be improved by increasing the resonator size from 400μm to 424μm and adding 4.3Ω of series resistance. The need to add series resistance is probably associated with the metalization of the fabricated device. The computed impedance of the resonator using the corrected parameters is shown in Fig. 2-3 superimposed on the measured data. Note that the agreement between experiment and theory is good, however the spurious responses are not predicted.

Fundamental Mode Stacked Crystal Filter Analysis

A fundamental mode stacked crystal filter consists of two piezoelectric plates that are bonded together back to back as shown in Fig. 2-4. Being a two-port device, the two-port network parameters can be calculated to determine the transfer function. The y-parameters are probably the easiest to compute because they impose homogeneous Dirichlet boundary conditions for the potential on the region 2 plate, and this boundary condition may be used directly when solving the piezoelectric device equations. The basic operating principle of the device is as follows. One of the plates is driven by a voltage source which generates an acoustic wave in region 1. This wave propagates through the center conductor generating a nonzero potential in region 2.

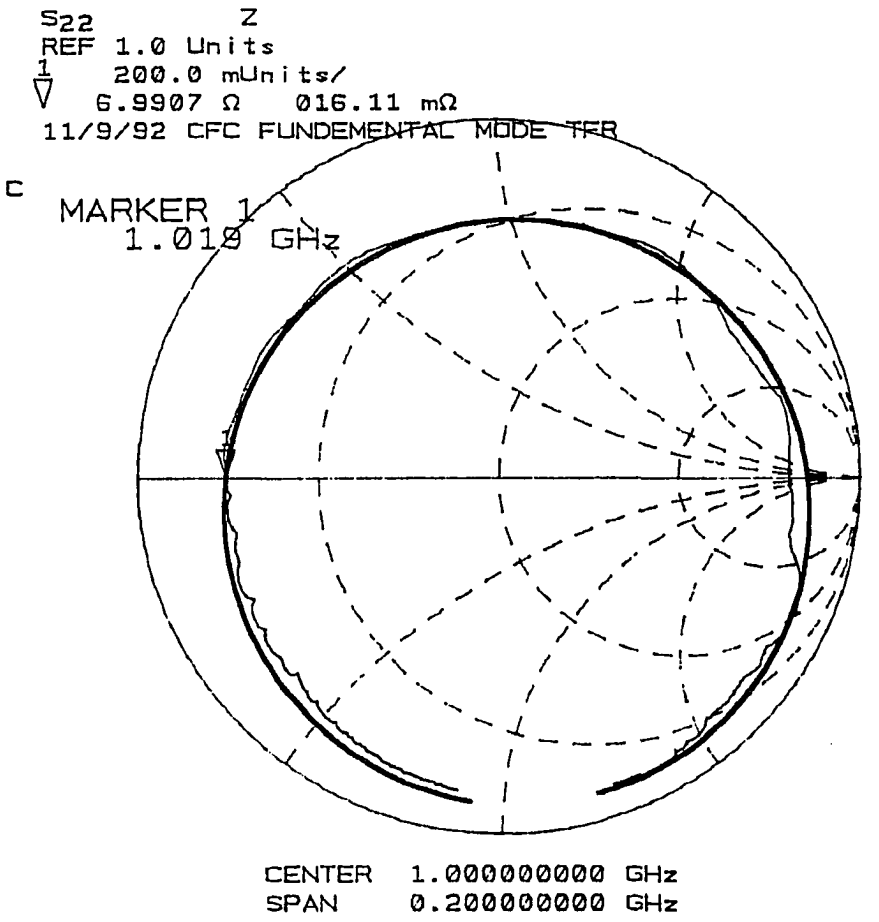

Figure 2-3. Predicted and measured AlN resonator impedance

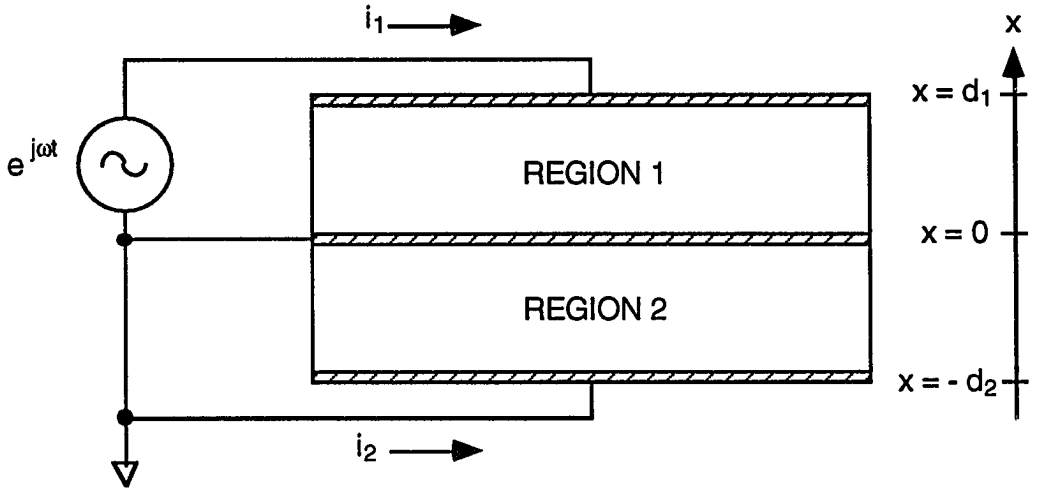

Figure 2-4. Fundamental mode stacked crystal filter

Consider the same assumptions that were used for the resonator analysis, and assume that material in regions 1 and 2 have the same crystallographic orientation. If one of the plates is twisted with respect to the other, the displacements in the x_1 and x_2 directions will no longer be zero and the coupled wave equations Eq. (2.28) will need to be solved. The governing differential equation is given by Eq. (2.37), and the potential is given by Eq. (2.38). The boundary conditions at the air-piezoelectric interfaces are the following:

$$\phi_1(d_1) = 1$$

$$\phi_1(0) = \phi_2(0) = \phi_2(-d_2) = 0$$

$$T_1(d_1) = T_2(-d_2) = 0$$

where the subscripts refer to region 1 and region 2 in Fig. 2-4. The continuity conditions at the region 1 - region 2 interface are

$$T_1(0) = T_2(0)$$

$$u_1(0) = u_2(0) .$$

Region 1 solutions are given by

$$u_1(x) = A_1 \cos kx + B_1 \sin kx \qquad (2.52a)$$

$$\phi_1(x) = (e/\varepsilon)\, A_1 \cos kx + (e/\varepsilon)\, B_1 \sin kx + \Gamma_1 x + \Delta_1 \qquad (2.52b)$$

$$T_1(x) = - ck\, A_1 \sin kx + ck\, B_1 \cos kx + e\, \Gamma_1 \qquad (2.52c)$$

and region 2 solutions are

$$u_2(x) = A_2 \cos kx + B_2 \sin kx \qquad (2.53a)$$

$$\phi_2(x) = (e/\varepsilon)\, A_2 \cos kx + (e/\varepsilon)\, B_2 \sin kx + \Gamma_2 x + \Delta_2 \qquad (2.53b)$$

$$T_2(x) = - ck\, A_2 \sin kx + ck\, B_2 \cos kx + e\, \Gamma_2 . \qquad (2.53c)$$

Applying the boundary conditions at the boundaries of region 1 gives

$$\phi_1(0) = (e/\varepsilon)\, A_1 + \Delta_1 = 0$$

$$\phi_1(d_1) = (e/\varepsilon)\, A_1 \cos kd_1 + (e/\varepsilon)\, B_1 \sin kd_1 + \Gamma_1 d_1 + \Delta_1 = 1$$

$$T_1(d_1) = - ck\, A_1 \sin kd_1 + ck\, B_1 \cos kd_1 + e\, \Gamma_1 = 0 .$$

Applying the boundary conditions at the boundaries of region 2 gives

$$\phi_2(0) = (e/\varepsilon)\, A_2 + \Delta_2 = 0$$

$$\phi_2(-d_2) = (e/\varepsilon)\, A_2 \cos kd_2 - (e/\varepsilon)\, B_2 \sin kd_2 - \Gamma_2 d_2 + \Delta_2 = 0$$

$$T_2(-d_2) = ck\, A_2 \sin kd_2 + ck\, B_2 \cos kd_2 + e\, \Gamma_2 = 0 .$$

The continuity conditions at the interface between region 1 and region 2 are as follows:

$$ck\,B_1 + e\,\Gamma_1 = ck\,B_2 + e\,\Gamma_2$$

$$A_1 = A_2 .$$

Defining

$$\theta_1 = kd_1$$

$$\theta_2 = kd_2$$

the system may be written as a matrix equation as shown in Fig. 2-5. The solution of this matrix equation gives the unknown constants for the fields in Eqs. (2.52) and (2.53). It is important to note that these field solutions are valid only for the short circuit condition shown in Fig. 2-4. These fields would be different for some other excitation. To compute the y-parameters the currents i_1 and i_2 need to be evaluated. From the resonator analysis section these currents are

$$i_1 = \int_S \mathbf{J}_1 \cdot d\mathbf{S} = -j\omega \int_S D_1 dS = j\omega\varepsilon\Gamma_1 A \qquad (2.54a)$$

$$i_2 = \int_S \mathbf{J}_2 \cdot d\mathbf{S} = -j\omega \int_S D_2 dS = j\omega\varepsilon\Gamma_2 A \; . \qquad (2.54b)$$

Since the voltage applied to port 1 is unity, for the case of equal thickness plates the y-parameters are symmetric and equal to the port currents.

$$y_{11} = y_{22} = i_1 \qquad (2.55a)$$

$$y_{21} = y_{12} = i_2 \qquad (2.55b)$$

$$\begin{bmatrix} \cos\theta_1 & 0 & \sin\theta_1 & 0 & \varepsilon d_1/e & 0 & \varepsilon/e & 0 \\ 0 & \cos\theta_2 & 0 & -\sin\theta_2 & 0 & -\varepsilon d_2/e & 0 & \varepsilon/e \\ -\sin\theta_1 & 0 & \cos\theta_1 & 0 & e/ck & 0 & 0 & 0 \\ 0 & \sin\theta_2 & 0 & \cos\theta_2 & 0 & e/ck & 0 & 0 \\ 0 & 0 & 1 & -1 & e/ck & -e/ck & 0 & 0 \\ 1 & -1 & 0 & 0 & 0 & 0 & 0 & 0 \\ \varepsilon/e & 0 & 0 & 0 & 0 & 0 & 1 & 0 \\ 0 & \varepsilon/e & 0 & 0 & 0 & 0 & 0 & 1 \end{bmatrix} \begin{bmatrix} A_1 \\ A_2 \\ B_1 \\ B_2 \\ \Gamma_1 \\ \Gamma_2 \\ \Delta_1 \\ \Delta_2 \end{bmatrix} = \begin{bmatrix} \varepsilon/e \\ 0 \\ 0 \\ 0 \\ 0 \\ 0 \\ 0 \\ 0 \end{bmatrix}$$

Figure 2-5. Fundamental mode stacked crystal filter matrix equation

If the plates are not of equal thickness, the excitation voltage will need to be applied to port 2 with port 1 short circuited and the calculation repeated. For a given source and load impedance Z_o the S-parameters may now be computed with the following:

$$S_{11} = \frac{(1 - y_{11} Z_o)(1 + y_{22} Z_o) + y_{12} y_{21} Z_o^2}{(1 + y_{11} Z_o)(1 + y_{22} Z_o) - y_{12} y_{21} Z_o^2} \tag{2.56a}$$

$$S_{12} = \frac{-2 y_{12} Z_o}{(1 + y_{11} Z_o)(1 + y_{22} Z_o) - y_{12} y_{21} Z_o^2} \tag{2.56b}$$

$$S_{21} = \frac{-2 y_{21} Z_o}{(1 + y_{11} Z_o)(1 + y_{22} Z_o) - y_{12} y_{21} Z_o^2} \tag{2.56c}$$

$$S_{22} = \frac{(1 + y_{11} Z_o)(1 - y_{22} Z_o) + y_{12} y_{21} Z_o^2}{(1 + y_{11} Z_o)(1 + y_{22} Z_o) - y_{12} y_{21} Z_o^2} . \tag{2.56d}$$

Plots of the S-parameters for a fundamental mode aluminum nitride stacked crystal filter that was fabricated at the MRC are shown in Fig. 2-6 and Fig. 2-7. The electrode plates are 400μm x 400μm in size and the aluminum nitride layers are nominally 5μm thick. Note the multiple passbands in the insertion loss plot. The first passband occurs where the entire structure is one half of an acoustic wavelength thick while the next two passbands occur when the device is one wavelength, and one and one half wavelengths thick respectively. Superimposed on the measured data are the S-parameters predicted by the theoretical one dimensional analysis presented in this section. Loss has been included in the analysis by using the following complex stiffness and dielectric constants:

$$\hat{c}_{33} = (395 + j3.3) \times 10^9 \text{ N/m}^2$$
$$\hat{\varepsilon}_{33} = (9.5 - j0.25) \times 10^{-11} \text{ F/m} .$$

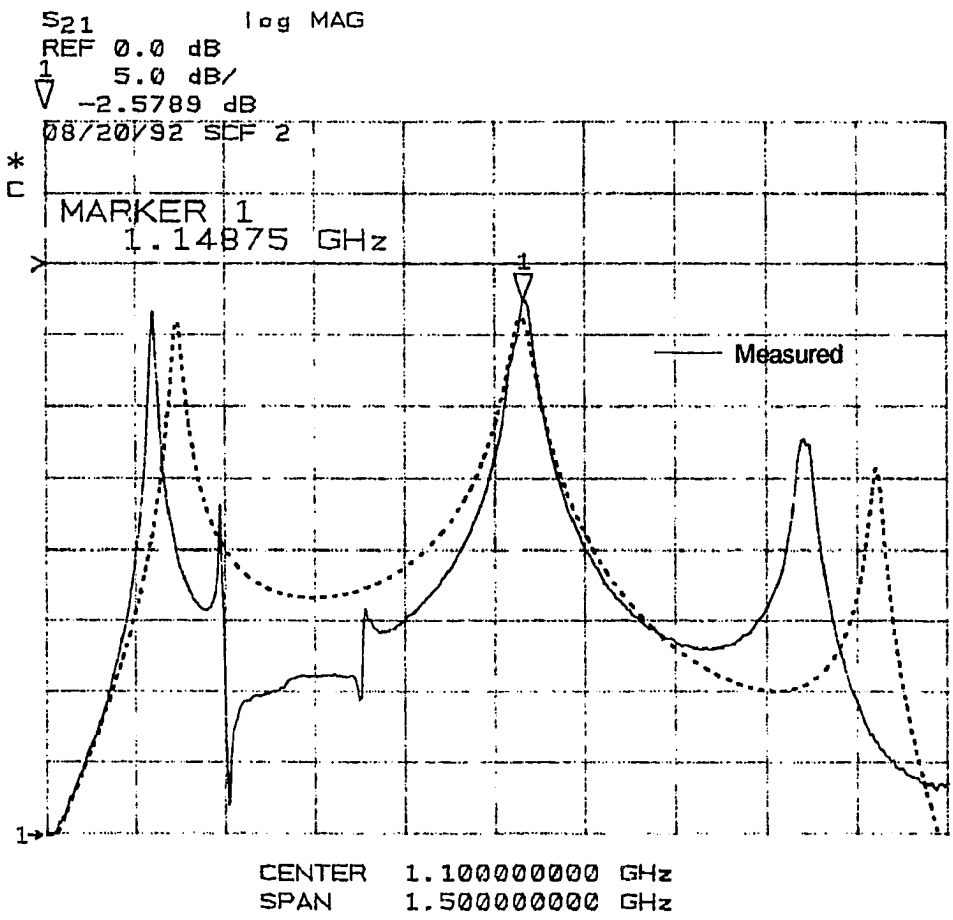

Figure 2-6. Measured fundamental mode AlN stacked crystal filter insertion loss response

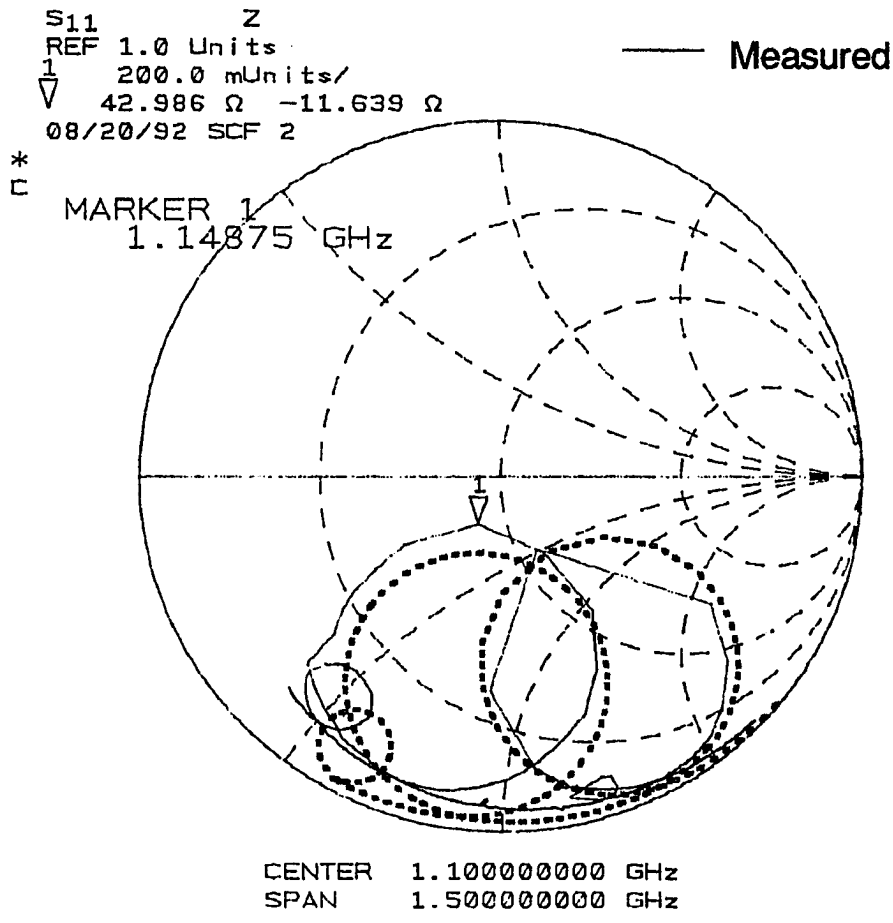

Figure 2-7. Measured fundamental mode AlN stacked crystal filter impedance

To obtain agreement between experiment and theory for the insertion loss of the filter, the imaginary part of the complex elastic constant had to be increased substantially over the values used in the resonator analysis sections. Since the dielectric loss tangent is unchanged, the additional observed loss is being lumped into the complex elastic constant. Processing differences in the AlN film deposition or poor quality metalization would necessitate an increase in the imaginary part of the elastic constant. The optimized aluminum nitride film thickness was found to be 4.88μm. The agreement with theory is excellent except for the spurious passbands which are due to the finite width dimensions of the device.

Overmoded Stacked Crystal Filter Analysis

An overmoded stacked crystal filter is similar to a fundamental mode device except an intervening layer of non-piezoelectric material is between the piezoelectric layers as shown in Fig. 2-8. Under the same assumptions as those used in the fundamental mode filter analysis, the fields in the piezoelectric regions 1 and 2 are given by Eqs. (2.52) and (2.53). Due to the shielding of the ground planes, the fields in the non-piezoelectric region 3 are just acoustic. These are given by

$$u_3(x) = A_3 \cos \hat{k}x + B_3 \sin \hat{k}x \tag{2.57a}$$

$$T_3(x) = - c_s \hat{k} A_3 \sin \hat{k}x + c_s \hat{k} B_3 \cos \hat{k}x \, . \tag{2.57b}$$

where c_s is the elastic constant for the longitudinal thickness mode of the non-piezoelectric medium. The wave number in the non-piezoelectric medium is related to its elastic constant and density ρ_s by

$$\hat{k} = \omega \sqrt{\frac{\rho_s}{c_s}} \, .$$

The boundary conditions for the problem are

$$\phi_1(d_1) = 1$$

$$\phi_1(0) = \phi_2(-h) = \phi_2(-h - d_2) = 0$$

$$T_1(d_1) = T_2(-h - d_2) = 0$$

$$T_1(0) = T_3(0)$$

$$T_2(-h) = T_3(-h)$$

$$u_1(0) = u_3(0)$$

$$u_2(-h) = u_3(-h) \,.$$

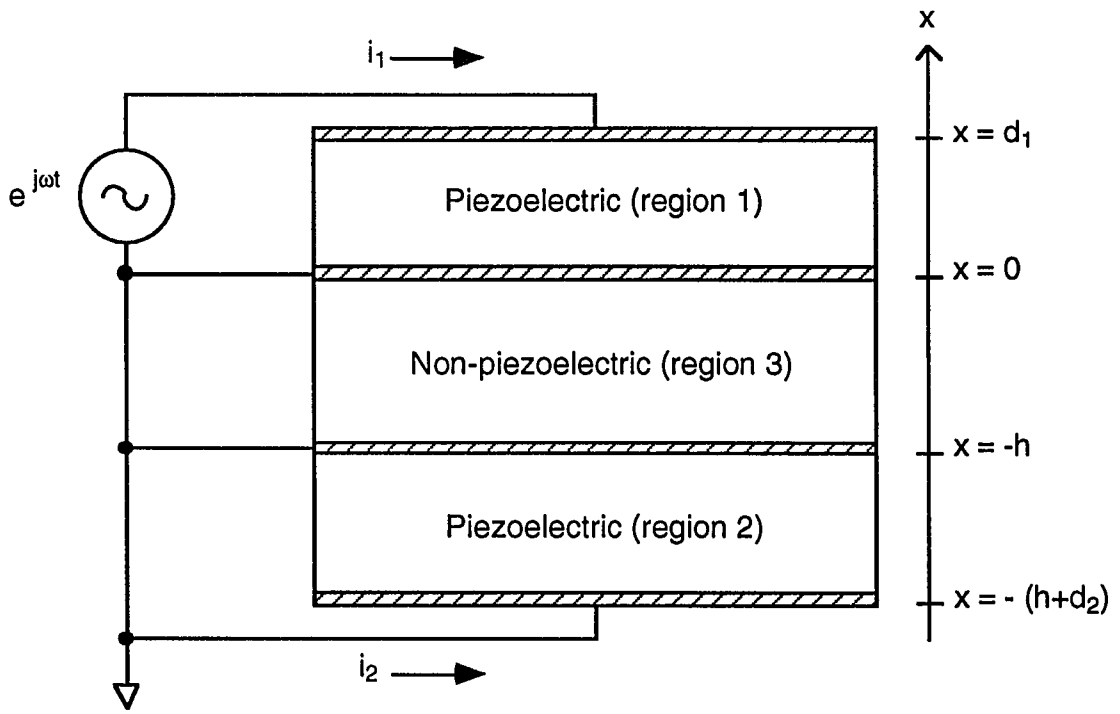

Figure 2-8. Overmoded stacked crystal filter

Applying these boundary conditions one obtains the following system of simultaneous equations:

$$\phi_1(0) = (e/\varepsilon)\, A_1 + \Delta_1 = 0$$

$$\phi_1(d_1) = (e/\varepsilon)\, A_1 \cos kd_1 + (e/\varepsilon)\, B_1 \sin kd_1 + \Gamma_1 d_1 + \Delta_1 = 1$$

$$T_1(d_1) = -\, ck\, A_1 \sin kd_1 + ck\, B_1 \cos kd_1 + e\, \Gamma_1 = 0$$

$$\phi_2(-h) = (e/\varepsilon)\, A_2 \cos kh - (e/\varepsilon)\, B_2 \sin kh - \Gamma_2 h + \Delta_2 = 0$$

$$\phi_2(-h - d_2) = (e/\varepsilon)\, A_2 \cos k(h + d_2) - (e/\varepsilon)\, B_2 \sin k(h + d_2) - \Gamma_2 (h + d_2) + \Delta_2 = 0$$

$$T_2(-h - d_2) = ck\, A_2 \sin k(h + d_2) + ck\, B_2 \cos k(h + d_2) + e\, \Gamma_2 = 0$$

$$A_1 = A_3$$

$$ck\, B_1 + e\, \Gamma_1 = \hat{k}\, c_s\, B_3$$

$$A_2 \cos kh - B_2 \sin kh = A_3 \cos \hat{k}h - B_3 \sin \hat{k}h$$

$$ck\, A_2 \sin kh + ck\, B_2 \cos kh + e\, \Gamma_2 = \hat{k}c_s\, A_3 \sin \hat{k}h + \hat{k}c_s\, B_3 \cos \hat{k}h$$

To simplify the expressions define the following:

$$\theta_2 = kh$$

$$\theta_3 = k(h + d_2)$$

$$\hat{\theta} = \hat{k}h$$

$$\alpha = \frac{\hat{k}c_s}{kc}$$

These expressions may be arranged into a matrix equation for the unknown constants as shown in Fig. 2-9. The port currents, y-parameters, and S-parameters for the device are computed with the same equations as for the fundamental mode stacked crystal filter. The response for an overmoded stacked crystal filter is shown in Fig. 2-10 and Fig. 2-11. This device consists of the same piezoelectric layers and conductor topology as the fundamental mode filter from the previous section, however a 315μm thick intervening layer of silicon has been included. Note that the response of this device is overmoded resembling that of a comb filter, and the passbands are narrowband. An overmoded stacked crystal filter where the intervening non-piezoelectric layer is between the piezoelectric layers has not yet been fabricated at the MRC, and experimental data is not available for comparison with theory. This type of filter is, however, what feeds the microstrip antenna in Fig. 1-1, and fabrication efforts are underway.

$$
\begin{bmatrix}
\cos\theta_1 & 0 & 0 & \sin\theta_1 & 0 & 0 & \varepsilon d_1/e & 0 & \varepsilon/e & 0 \\
0 & \cos\theta_2 & 0 & 0 & -\sin\theta_2 & 0 & 0 & -\varepsilon h/e & 0 & \varepsilon/e \\
-\sin\theta_1 & 0 & 0 & \cos\theta_1 & 0 & 0 & e/ck & 0 & 0 & 0 \\
0 & \sin\theta_3 & 0 & 0 & \cos\theta_3 & 0 & 0 & e/ck & 0 & 0 \\
0 & 0 & 0 & 1 & 0 & -\alpha & e/ck & 0 & 0 & 0 \\
1 & 0 & -1 & 0 & 0 & 0 & 0 & 0 & 0 & 0 \\
1 & 0 & 0 & 0 & 0 & 0 & 0 & 0 & \varepsilon/e & 0 \\
0 & \cos\theta_3 & 0 & 0 & -\sin\theta_3 & 0 & 0 & -\varepsilon(h+d_2)/e & 0 & \varepsilon/e \\
0 & \sin\theta_2 & -\alpha\sin\hat{\theta} & 0 & \cos\theta_2 & -\alpha\cos\hat{\theta} & 0 & e/ck & 0 & 0 \\
0 & \cos\theta_2 & -\cos\hat{\theta} & 0 & -\sin\theta_2 & \sin\hat{\theta} & 0 & 0 & 0 & 0
\end{bmatrix}
\begin{bmatrix} A_1 \\ A_2 \\ A_3 \\ B_1 \\ B_2 \\ B_3 \\ \Gamma_1 \\ \Gamma_2 \\ \Delta_1 \\ \Delta_2 \end{bmatrix}
=
\begin{bmatrix} \varepsilon/e \\ 0 \\ 0 \\ 0 \\ 0 \\ 0 \\ 0 \\ 0 \\ 0 \\ 0 \end{bmatrix}
$$

Figure 2-9. Overmoded stacked crystal filter matrix equation

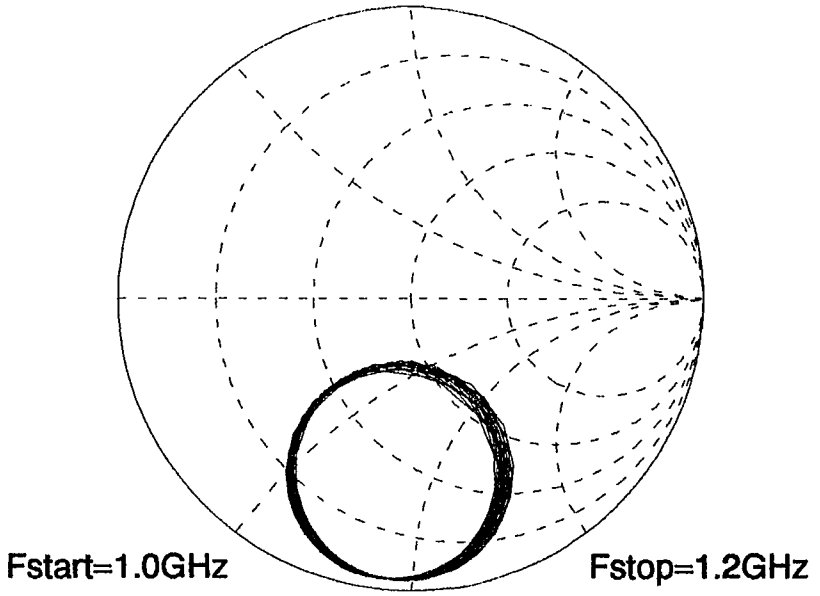

Figure 2-10. Predicted overmoded AlN/Si stacked crystal filter impedance

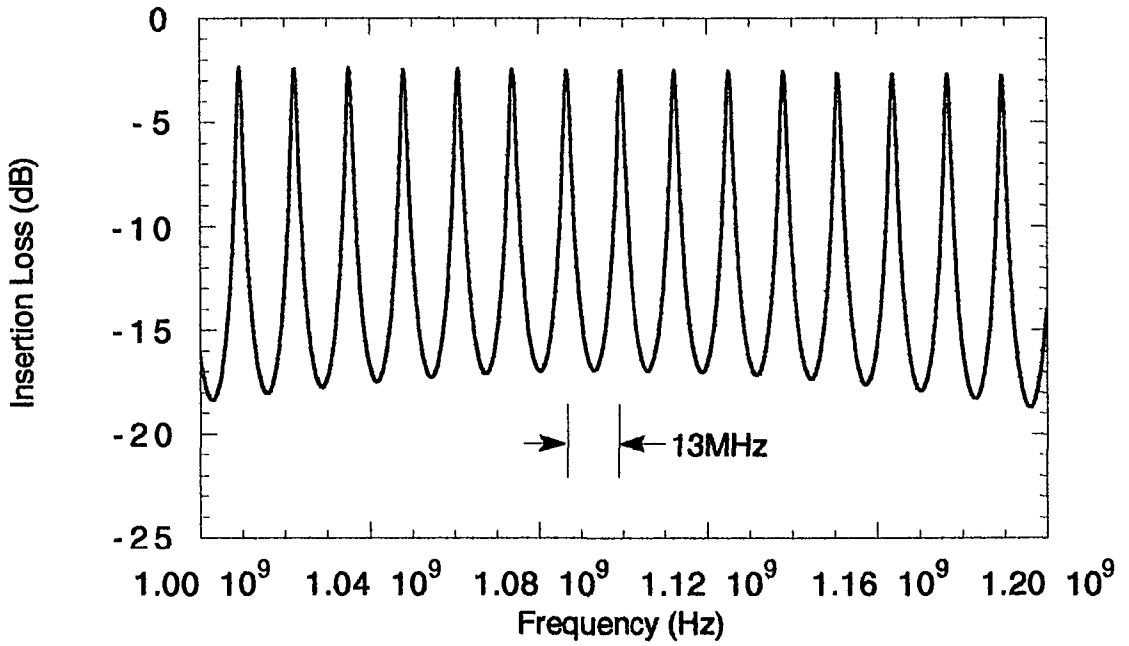

Figure 2-11. Predicted overmoded AlN/Si stacked crystal filter insertion loss

CHAPTER 3. MICROSTRIP ANTENNA THEORY

Planar Circuit Analysis

A typical microstrip antenna consists of a radiating element fed by a z-directed current, a dielectric slab and a conducting ground plane as illustrated in Fig. 3-1. The conductors are characterized by a finite conductivity σ, and the dielectric by its permittivity ε. The ground plane and dielectric layer are assumed to extend to infinity in the x and y directions, and the radiating element has dimensions, a x b. The dielectric layer is of thickness $d << \lambda$, and for the moment the radiating element is assumed to have negligible thickness yet be thicker than a skin depth. Since the thickness of the dielectric layer separating the antenna from the ground plane is much smaller than a wavelength, the electric field can be assumed to be z-directed and have no z-dependence [24,25]. Under these assumptions, the electric field will obey the Helmholtz equation.

$$\frac{\partial^2 E_z}{\partial x^2} + \frac{\partial^2 E_z}{\partial y^2} + \omega^2 \mu\varepsilon E_z = j\omega\mu J_z(x,y) \tag{3.1}$$

The magnetic field under the patch is found from Faraday's law Eq. (2.4).

$$\mathbf{H} = \frac{-1}{j\omega\mu} \nabla \times \hat{z} E_z = \frac{-1}{j\omega\mu} \left[\hat{x} \frac{\partial E_z}{\partial y} - \hat{y} \frac{\partial E_z}{\partial x} \right] \tag{3.2}$$

The magnetic field will excite surface currents on the bottom surface of the patch

$$\mathbf{J_s} = \hat{x} J_{sx} + \hat{y} J_{sy} = \hat{n} \times \mathbf{H}(d) = \frac{1}{j\omega\mu} \left[\hat{x} \frac{\partial E_z}{\partial x} + \hat{y} \frac{\partial E_z}{\partial y} \right] \tag{3.3}$$

where the normal vector is directed in the negative z-direction as shown in Fig. 3-1a. Since the patch edge is an open circuit one may assume that the surface currents do not flow off the edge of the patch, and the component of the current

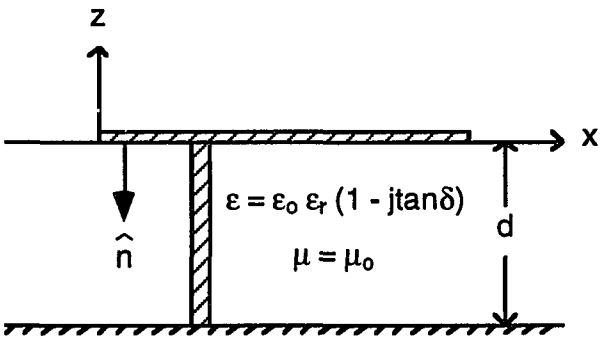

(a) Side view of a microstrip antenna

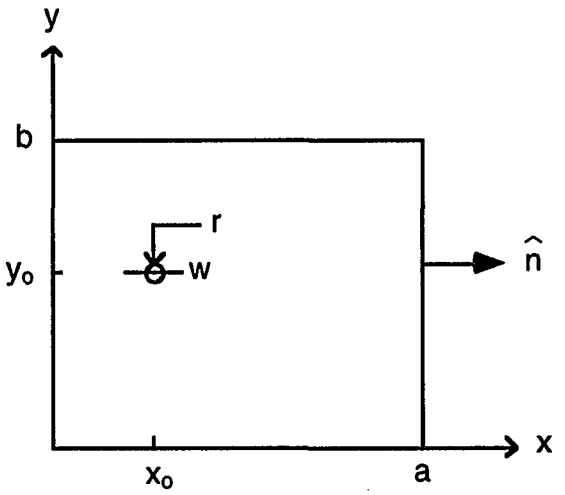

(b) Top view of a microstrip antenna

Figure 3-1. Coaxially fed microstrip antenna

normal to the edge of the patch must then be zero. This is effectively a no fringing fields approximation where at the patch edges

$$\hat{n} \cdot \mathbf{J}_s = 0 \quad . \tag{3.4}$$

The normal vector in Eq. (3.4) is now outwardly directed from the patch edge as shown in Fig. 3-1b. Substituting Eq. (3.3) into Eq. (3.4), the boundary condition in terms of the electric field at the patch edge is

$$\frac{\partial E_z}{\partial n} = 0 \quad . \tag{3.5}$$

This boundary condition states that the tangential magnetic field at the patch edges must be zero which is the same condition obtained if the patch edges were perfect magnetic conductors; hence the term magnetic wall boundary condition. In reality the fields do fringe at the patch edges, and this may be accounted for by the use of effective dimensions and dielectric constant. For a circuit of width W and length L, the dielectric constant is replaced by an effective dielectric constant and the length dimension is extended.

$$L \rightarrow L + 2\Delta L$$

$$\varepsilon_r \rightarrow \varepsilon_{eff}$$

Defining the parameter

$$\alpha = W/d$$

the effective dielectric constant may be estimated with [20]

$$\varepsilon_{eff} = \frac{\varepsilon_r + 1}{2} + \frac{\varepsilon_r - 1}{2} (1 + 10/\alpha)^{-\Sigma\Lambda}$$

$$\Sigma = 1 + \frac{1}{49} \ln\left[\frac{\alpha^4 + (\alpha/52)^2}{\alpha^4 + 0.432}\right] + \frac{1}{18.7} \ln\left[1 + (\alpha/18.1)^3\right]$$

$$\Lambda = 0.564 \left[\frac{\varepsilon_r - 0.9}{\varepsilon_r + 3}\right]^{0.053}$$

An approximate length extension equation is given by [20]

$$\Delta L = d \frac{\xi_1 \xi_3 \xi_5}{\xi_4}$$

where

$$\xi_1 = 0.434907 \left[\frac{\varepsilon_{eff}^{0.81} + 0.26}{\varepsilon_{eff}^{0.81} - 0.189}\right]\left[\frac{\alpha^{0.8544} + 0.236}{\alpha^{0.8544} + 0.87}\right]$$

$$\xi_2 = 1 + \frac{\alpha^{0.371}}{2.358\varepsilon_r + 1}$$

$$\xi_3 = 1 + \frac{0.5274 \tan^{-1}\left[0.084\, \alpha^{1.9413/\xi_2}\right]}{\varepsilon_{eff}^{0.9236}}$$

$$\xi_4 = 1 + 0.0377 \tan^{-1}\left[0.067\, \alpha^{1.456}\right]\left[6 - 5\, e^{0.036(1 - \varepsilon_r)}\right]$$

$$\xi_5 = 1 - 0.218\, e^{-7.5\alpha} .$$

The fringing fields at the edge of the patch have the effect of changing the resonant frequency of the microstrip antenna, and through the use of the effective parameters the resonant frequency of the structure may be accurately predicted.

The solution of Eq. (3.1) under the boundary conditions given by Eq. (3.5) is planar circuit analysis [24,25]. The most general solution of this equation is

$$E_z(x,y) = \int_{feed} G(x,y \mid x_o,y_o)\, J_z(x_o,y_o)\, dx_o dy_o \quad . \tag{3.6}$$

The Green's function for a rectangular patch under the perfect magnetic wall boundary condition is given by

$$G(x,y \mid x_o,y_o) = \frac{-j\omega\mu}{ab} \sum_{m=0}^{\infty} \sum_{n=0}^{\infty} \frac{\alpha_n \alpha_m \cos(k_x x) \cos(k_y y) \cos(k_x x_o) \cos(k_y y_o)}{k_x^2 + k_y^2 - k^2} \tag{3.7}$$

$$k_x = \frac{m\pi}{a} \qquad k_y = \frac{n\pi}{b} \qquad k^2 = \omega^2 \mu\varepsilon$$

$$\alpha_i = 2 - \delta_{i0} \quad .$$

and δ_{i0} is the Kronecker delta function. Green's functions exist for other canonical shapes such as triangles, circles, etc. Structures for which Green's functions do not exist may be analyzed with the segmentation-desegmentation method or the contour integral method [24,25]. Solutions obtained with Eq. (3.6) require the evaluation of a double summation resulting in long computation times.

It can be shown that a small coaxial feed or a transmission line feed may be approximated by a z-directed constant current strip of width w as shown in Fig. 3-1b. The current strip for the microstrip transmission line feed is of the physical width and location of the line. For a coaxial feed of radius r an equivalent strip feed of width

$$w = 4.482\, r \tag{3.8}$$

is centered on the location of the coaxial feed as shown in Fig. 3-1b. Whether the current strip is oriented in the x or y direction was not found to change the result

obtained for the input impedance of the antenna. Since a current strip is one dimensional, the solution to the Helmholtz equation may be obtained with the mode matching method and written in terms of a single summation, which is more rapidly convergent then the double summation in the Green's function solution. The result obtained with the mode matching method is mathematically equivalent to the Green's function solution, and may be considered as summing in closed form the inner summation [22].

Solutions for the electric field under the patch which satisfy the Helmholtz equation and the magnetic wall boundary conditions may be expressed as

$$E_z(x,y) = \sum_{m=0}^{\infty} A_m \cos(k_x x) \cos(\beta_m y) \quad , \quad 0 \le y \le y_o \tag{3.9a}$$

$$E_z(x,y) = \sum_{m=0}^{\infty} B_m \cos(k_x x) \cos\beta_m(y-b) \quad , \quad y_o \le y \le b \tag{3.9b}$$

$$\beta_m = \sqrt{k^2 - k_x^2} \ .$$

The presence of the feed at $y=y_o$ requires the separation of the solutions in Eq. (3.9), and A_m and B_m are arbitrary constants to be found by matching the boundary conditions at the feed. The boundary conditions at the feed position are the continuity of the tangential electric field and a jump condition of the tangential magnetic field.

$$E_z(x,y_o^+) = E_z(x,y_o^-) \tag{3.10}$$

$$\hat{n} \times \left[\mathbf{H}(x,y_o^+) - \mathbf{H}(x,y_o^-)\right] = \hat{z}\, J_z(x) \tag{3.11}$$

The jump condition for the magnetic field leads to

$$\hat{y} \times \hat{x}\left[H_x(x,y_o^+) - H_x(x,y_o^-)\right] = \hat{z}\, J_z(x) \quad \Rightarrow \quad H_x(x,y_o^+) - H_x(x,y_o^-) = -J_z(x) \ . \tag{3.12}$$

The source current density may be expanded as a Fourier series of resonant modes.

$$J_z(x) = \sum_{m=0}^{\infty} j_m \cos(k_x x) \tag{3.13}$$

$$j_m = \frac{2 - \delta_{m0}}{a} \int_0^a J_z(x) \cos(k_x x)\, dx \tag{3.14}$$

For the 1A (rms) constant current strip feed model the Fourier constants are

$$j_m = \frac{2 - \delta_{m0}}{a\, w} \int_{x_o - w/2}^{x_o + w/2} \cos(k_x x)\ dx = \frac{2 - \delta_{m0}}{a} \cos(k_x x_o)\ \mathrm{sinc}(k_x w / 2) \tag{3.15}$$

To preserve the continuity of the electric field, match the resonant modes at $y=y_o$

$$\sum_{m=0}^{\infty} A_m \cos(k_x x) \cos(\beta_m y_o) = \sum_{m=0}^{\infty} B_m \cos(k_x x) \cos\beta_m(y_o - b)$$

which leads to

$$B_m = A_m \frac{\cos(\beta_m y_o)}{\cos\beta_m(y_o - b)}\ .$$

The x-component of the magnetic field is found from Eq. (3.2).

$$H_x(x,y) = \frac{1}{j\omega\mu} \sum_{m=0}^{\infty} A_m \beta_m \cos(k_x x) \sin(\beta_m y)\ ,\quad 0 \le y \le y_o$$

$$H_x(x,y) = \frac{1}{j\omega\mu} \sum_{m=0}^{\infty} B_m \beta_m \cos(k_x x) \sin\beta_m(y - b)\ ,\quad y_o \le y \le b$$

To satisfy the jump condition for the magnetic field, match the resonant modes.

$$\frac{1}{j\omega\mu}\sum_{m=0}^{\infty}\left[B_m\,\beta_m\cos(k_x x)\sin\beta_m(y_o-b) - A_m\,\beta_m\cos(k_x x)\sin(\beta_m y_o)\right] = -\sum_{m=0}^{\infty} j_m\cos(k_x x)$$

Solving for the mode amplitudes one obtains

$$A_m = j_m\left[\frac{j\omega\mu\cos\beta_m(y_o-b)}{\beta_m\sin(\beta_m b)}\right] \tag{3.16}$$

$$B_m = j_m\left[\frac{j\omega\mu\cos(\beta_m y_o)}{\beta_m\sin(\beta_m b)}\right]. \tag{3.17}$$

Eqs. (3.9), (3.16) and (3.17) constitute approximate solutions for the electric field of a rectangular patch over a conducting ground plane, and these results are used in order to predict the characteristics of the microstrip antenna.

Far Field Radiation

In order to estimate the far field radiation pattern and radiated power for the antenna, the radiated far fields must be found. One way to approximate the far fields is to apply the equivalence principle to the structure as shown in Fig. 3-2. The idea behind the equivalence principle is to surround the source by a closed surface S and to place equivalent sources on the closed surface.

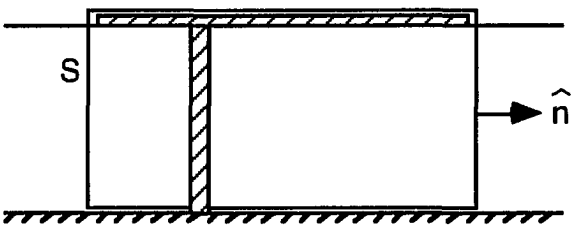

Figure 3-2. Application of the equivalence principle

The equivalent sources produce the same fields outside of the closed surface as did the original source, but produce null fields inside the surface. The equivalent sources are found by the following [26]:

$$\mathbf{M}_s = \mathbf{E} \times \hat{n} \tag{3.18}$$

$$\mathbf{J}_s = \hat{n} \times \mathbf{H} \tag{3.19}$$

where the fields are approximated by planar circuit analysis. Due to the magnetic wall boundary condition, the tangential magnetic field and thus electric surface current will be zero on the sides. Similarly, assuming the ground plane and patch to be perfect electric conductors the tangential electric field and thus the magnetic surface current density is zero on the top and bottom surfaces. If the top conductor is much thicker than a skin depth, then the electric current density will reside mostly on the bottom of the patch and the current on the top of the patch will be approximately zero. If the conducting patch is not much thicker than a skin depth, then the amount of tangential magnetic field that tunnels through the conductor will have to be computed, and some electric surface current will exist on the top surface. The magnetic surface current density on the sides is given by Eq. (3.18), and is the main source of the radiated fields. Thus, the radiation model for the microstrip antenna is shown in Fig. 3-3 where the circle with a dot indicates a vector directed out of the page.

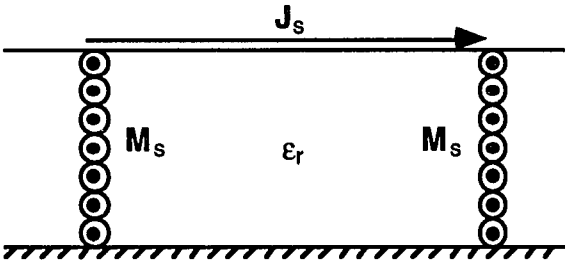

Figure 3-3. Radiation model for the microstrip antenna

The model consists of a sheet of electric current density on top of a grounded infinite dielectric slab and a ribbon of magnetic current density embedded in the dielectric slab. The total magnetic current **K** that exists at the periphery of the surface is found by integrating the magnetic current density over the thickness of the substrate.

$$\mathbf{K} = \int_{-d}^{0} \mathbf{M}_s \, dz = \mathbf{M}_s d \tag{3.20}$$

The approach to finding the far field radiation from the model in Fig. 3-3 is to first find the radiated far fields from infinitesimal horizontal Hertzian dipoles of electric and magnetic current. To illustrate this point, consider Fig. 3-4. Shown in Fig. 3-4a is an x-directed infinitesimal electric current dipole of unit strength residing on a grounded dielectric. Expressions for the Hertzian dipole far fields are available in the literature, and are found by using reciprocity and applying the transmission line model for plane waves impinging on a dielectric at oblique incidence [19,26]. The radiated far fields for the electric current dipole are

$$E_\theta^{hex}(r,\theta,\varphi) = - A(\theta) \frac{j\omega\mu_o}{4\pi r} e^{-jk_o r} \cos\theta \cos\varphi \tag{3.21a}$$

$$E_\varphi^{hex}(r,\theta,\varphi) = B(\theta) \frac{j\omega\mu_o}{4\pi r} e^{-jk_o r} \sin\varphi \tag{3.21b}$$

where the factors $A(\theta)$ and $B(\theta)$ account for the presence of the grounded dielectric. These factors are given by

$$A(\theta) = \frac{2 \tan \beta d}{\tan \beta d - j\varepsilon_r (k_o / \beta)\cos\theta} \tag{3.22a}$$

$$B(\theta) = \frac{2 \tan \beta d}{\tan \beta d - j(\beta / k_o)\sec\theta} \tag{3.22b}$$

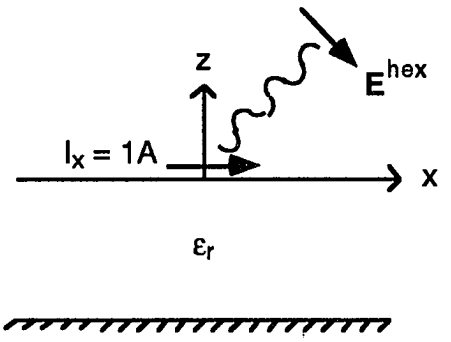

(a) Infinitesimal electric current dipole

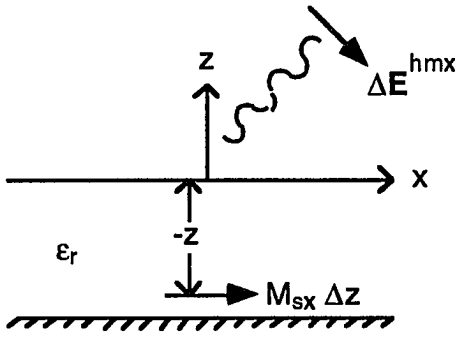

(b) Differential magnetic current element

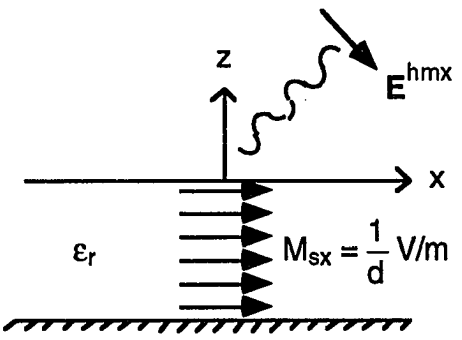

(c) Normalized infinitesimal magnetic current ribbon

Figure 3-4. Calculation of the infinitesimal dipole far fields

where

$$\beta = k_o\sqrt{\varepsilon_r - \sin^2\theta} \ .$$

Similarly, the expressions for a y-directed electric current dipole of unit strength are given by

$$E_\theta^{hey}(r,\theta,\varphi) = - A(\theta)\frac{j\omega\mu_o}{4\pi r} e^{-jk_o r}\cos\theta \sin\varphi \qquad (3.23a)$$

$$E_\varphi^{hey}(r,\theta,\varphi) = - B(\theta)\frac{j\omega\mu_o}{4\pi r} e^{-jk_o r}\cos\varphi \ . \qquad (3.23b)$$

The calculation of the dipole fields for the magnetic current ribbon embedded in a grounded dielectric substrate is slightly more complicated. Shown in Fig. 3-4b is an x-directed differential magnetic current element of strength $M_{sx}\,\Delta z$. The differential radiated far fields for the current element embedded in a grounded dielectric substrate at position -z are [19]

$$\Delta E_\theta^{hmx} = \left[2 - A(\theta)\right]\frac{j\omega\mu_o}{4\pi\eta_o r} e^{-jk_o r}\sin\varphi \frac{\cos\beta(z+d)}{\cos\beta d} M_{sx}\,\Delta z \qquad (3.24a)$$

$$\Delta E_\varphi^{hmx} = \left[2 - B(\theta)\right]\frac{j\omega\mu_o}{4\pi\eta_o r} e^{-jk_o r}\cos\theta\cos\varphi \frac{\cos\beta(z+d)}{\cos\beta d} M_{sx}\,\Delta z \qquad (3.24b)$$

where the free space impedance is equal to

$$\eta_o = \sqrt{\frac{\mu_o}{\varepsilon_o}} \ .$$

The radiation model for the microstrip antenna, however, requires the calculation of the radiated far fields from a ribbon of magnetic current density

flowing on the sides of the closed surface S. A ribbon of magnetic current density may be constructed from differential current elements as shown in Fig. 3-4c. Let the magnetic current density be normalized such that the total magnetic current is of unity strength. From Eq. (3.20) the magnetic current density is then equal to

$$K_x = \int_{-d}^{0} M_{sx}\, dz = M_{sx} d = 1 \quad \Rightarrow \quad M_{sx} = \frac{1}{d}$$

The radiated far fields from the infinitesimal magnetic current ribbon are found by integrating the differential fields over the substrate thickness. In the far field the source to observer distance r, and polar angles θ and φ are approximately constant over the substrate thickness, and may be left out of the integration. Performing the integration, the radiated far fields from the normalized x-directed magnetic current ribbon are

$$E_\theta^{hmx}(r,\theta,\varphi) = \int_{-d}^{0} \Delta E_\theta^{hmx} = i_d \left[2 - A(\theta)\right] \frac{j\omega\mu_o}{4\pi\eta_o r} e^{-jk_o r} \sin\varphi \qquad (3.25a)$$

$$E_\varphi^{hmx}(r,\theta,\varphi) = \int_{-d}^{0} \Delta E_\varphi^{hmx} = i_d \left[2 - B(\theta)\right] \frac{j\omega\mu_o}{4\pi\eta_o r} e^{-jk_o r} \cos\theta \cos\varphi \qquad (3.25b)$$

where in limit as Δz approaches dz the integration factor is equal to

$$i_d = \int_{-d}^{0} M_{sx} \frac{\cos\beta(z+d)}{\cos\beta d}\, dz = \frac{1}{d} \int_{-d}^{0} \frac{\cos\beta(z+d)}{\cos\beta d}\, dz = \frac{\tan\beta d}{\beta d} \qquad (3.26)$$

Similarly, the radiated far fields for the normalized y-directed ribbon of magnetic current are equal to

$$E_\theta^{hmy}(r,\theta,\varphi) = -\, I_d \left[2 - A(\theta)\right] \frac{j\omega\mu_o}{4\pi\eta_o r} e^{-jk_o r} \cos\varphi \qquad (3.27a)$$

$$E_{\varphi}^{hmy}(r,\theta,\varphi) = I_d\left[2 - B(\theta)\right]\frac{j\omega\mu_o}{4\pi\eta_o r}e^{-jk_o r}\cos\theta\sin\varphi \quad . \tag{3.27b}$$

The total dipole far fields are just the summation of the vector components.

$$\hat{x}\text{ Electric dipole: } \mathbf{E}_{rad}^{hex}(r,\theta,\varphi) = \hat{\varphi}\,E_{\varphi}^{hex}(r,\theta,\varphi) + \hat{\theta}\,E_{\theta}^{hex}(r,\theta,\varphi) \tag{3.28a}$$

$$\hat{y}\text{ Electric dipole: } \mathbf{E}_{rad}^{hey}(r,\theta,\varphi) = \hat{\varphi}\,E_{\varphi}^{hey}(r,\theta,\varphi) + \hat{\theta}\,E_{\theta}^{hey}(r,\theta,\varphi) \tag{3.28b}$$

$$\hat{x}\text{ Magnetic dipole: } \mathbf{E}_{rad}^{hmx}(r,\theta,\varphi) = \hat{\varphi}\,E_{\varphi}^{hmx}(r,\theta,\varphi) + \hat{\theta}\,E_{\theta}^{hmx}(r,\theta,\varphi) \tag{3.28c}$$

$$\hat{y}\text{ Magnetic dipole: } \mathbf{E}_{rad}^{hmy}(r,\theta,\varphi) = \hat{\varphi}\,E_{\varphi}^{hmy}(r,\theta,\varphi) + \hat{\theta}\,E_{\theta}^{hmy}(r,\theta,\varphi) \tag{3.28d}$$

The next step is to find the radiated fields from the entire current distribution shown in the radiation model. The total fields are the superposition of the infinitesimal dipole far fields integrated over the actual source current distribution. Since the effect of the substrate and ground plane are included in the dipole field expressions through the use of the substrate factors $A(\theta)$ and $B(\theta)$, the substrate and ground plane may be removed. The radiation model valid for the upper half plane reduces to a sheet of electric surface current density $\mathbf{J_S}$ and a loop of magnetic current $\mathbf{K}$ as shown in Fig. 3-5. The radiated far fields for the entire source distribution are equal to the product of the unity strength infinitesimal dipole far fields and the Fourier transforms of the source distributions [26].

$$\mathbf{E}_{rad}^{e} = \mathbf{E}_{rad}^{hex}(r,\theta,\varphi)\,\tilde{J}_{sx}(u,v) + \mathbf{E}_{rad}^{hey}(r,\theta,\varphi)\,\tilde{J}_{sy}(u,v) \tag{3.29a}$$

$$\mathbf{E}_{rad}^{m} = \mathbf{E}_{rad}^{hmx}(r,\theta,\varphi)\,\tilde{K}_{x}(u,v) + \mathbf{E}_{rad}^{hmy}(r,\theta,\varphi)\,\tilde{K}_{y}(u,v) \tag{3.29b}$$

The Fourier transforms are defined by Eq. (3.30) where the path C is around the periphery of the closed surface, and surface A is over the top of the closed surface as shown in Fig. 3-5.

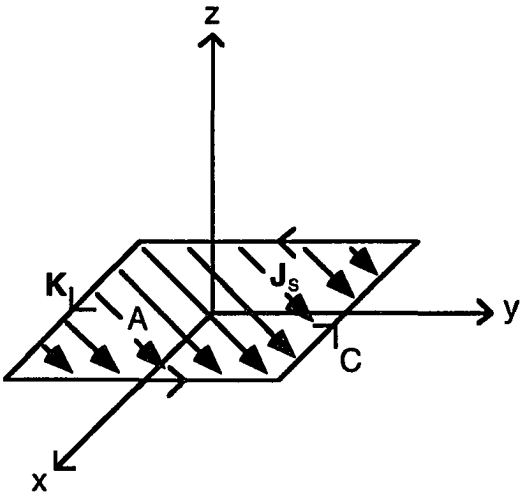

Figure 3-5. Far field radiation model

$$\tilde{J}_{sx}(u,v) = \int_A J_{sx}(x,y)\, e^{j(ux+vy)}\, dx\, dy \tag{3.30a}$$

$$\tilde{J}_{sy}(u,v) = \int_A J_{sy}(x,y)\, e^{j(ux+vy)}\, dx\, dy \tag{3.30b}$$

$$\tilde{K}_x(u,v) = \int_C K_x(x,y)\, e^{j(ux+vy)}\, \hat{x} \cdot dl \tag{3.30c}$$

$$\tilde{K}_y(u,v) = \int_C K_y(x,y)\, e^{j(ux+vy)}\, \hat{y} \cdot dl \tag{3.30d}$$

$$u = k_o \sin\theta \cos\varphi$$

$$v = k_o \sin\theta \sin\varphi$$

$$k_o = \omega\sqrt{\varepsilon_o \mu_o}$$

The total radiated far field for the microstrip antenna is then the superposition of the contributions from the electric and magnetic current source fields.

$$\mathbf{E}_{rad} = \mathbf{E}^{e}_{rad} + \mathbf{E}^{m}_{rad} \tag{3.31}$$

The Cavity Model

The basic principle behind the cavity model is to predict the input impedance of a microstrip antenna by lumping the losses (conductor, dielectric, radiative, etc.) into a quality factor Q [19,21,23]. Once a quality factor is found, an effective loss tangent for the cavity may be computed and results from planar circuit theory applied to predict the input impedance of the lossy cavity. The quality factor of a circuit is defined as

$$Q = \omega \frac{\text{Stored Energy}}{\text{Power Loss}} = \omega \frac{U_s}{P_L} \tag{3.32}$$

where the power loss includes the sum of all the losses in the circuit. The losses for the microstrip antenna are dielectric loss P_d, conductor loss P_c, and radiation loss P_r. The total power loss is then

$$P_L = P_d + P_c + P_r$$

from which the overall quality factor may then be split up into individual quality factors according to

$$\frac{1}{Q} = \frac{1}{Q_d} + \frac{1}{Q_c} + \frac{1}{Q_r} . \tag{3.33}$$

The stored energy in the cavity is given by

$$U_s = \frac{1}{2}\int_V \left[\mathbf{D}\cdot\mathbf{E} + \mathbf{B}\cdot\mathbf{H}\right] dV = \frac{1}{2}\int_V \left[\varepsilon|\mathbf{E}|^2 + \mu|\mathbf{H}|^2\right] dV \tag{3.34}$$

where the integral is over the volume of the cavity. The dielectric loss is

$$P_d = \omega\varepsilon \tan\delta \int_V |\mathbf{E}|^2 \, dV \quad . \tag{3.35}$$

Assuming that the metalization is much thicker than a skin depth the conductor loss is computed with

$$P_c = 2\sqrt{\frac{\omega\mu}{2\sigma}} \int_S |\mathbf{H}(d)|^2 \, dS \tag{3.36}$$

where the integral is over the surface of the conducting patch. The loss due to fields radiating away from the antenna is given by

$$P_r = \frac{1}{\eta_o} \int_0^{2\pi} \int_0^{\pi/2} |\mathbf{E}_{rad}|^2 r^2 \sin\theta \, d\theta \, d\varphi \tag{3.37}$$

Evaluating these integrals, a quality factor may be found from Eq. (3.32). To illustrate how the quality factor is used to compute input impedance consider the cavity being driven at its resonant frequency ω_o. At resonance, the energy stored in the electric field is equal to the energy stored in the magnetic field, and the total energy stored in the cavity may be written as

$$U_s = \varepsilon d \int_S |\mathbf{E}|^2 \, dS \quad . \tag{3.38}$$

Substituting Eq. (3.35) and Eq. (3.38) into Eq. (3.32), the dielectric quality factor is given by the following

$$Q_d = \omega_o \frac{U_s}{P_d} = \omega_o \frac{\varepsilon d \int_S |\mathbf{E}|^2 \, dS}{\omega_o \varepsilon d \tan\delta \int_S |\mathbf{E}|^2 \, dS} = \frac{1}{\tan\delta} \quad . \tag{3.39}$$

Therefore, it is reasonable to approximate the effective loss tangent which includes all of the losses in the cavity by the inverse of the quality factor [21].

$$\tan\delta_{eff} = \frac{1}{Q} \tag{3.40}$$

The effective loss tangent is then used to compute electric field within the cavity with planar circuit theory. Since the input current was assumed to be a 1A (rms) constant current strip, the average voltage over the feed will be equal to the input impedance of the cavity. The average voltage over the feed is given by

$$Z_{in} = V_{ave} = \frac{-d}{w} \int_{x_o - w/2}^{x_o + w/2} E_z(x, y_o) \, dx \quad . \tag{3.41}$$

Microstrip Antenna Examples

To illustrate the use of planar circuit analysis and the cavity model consider the rectangular microstrip antenna geometry shown in Fig. 3-6. Two devices with this topology were fabricated on a Rogers RT/Duroid substrate in order to compare the measured data with that predicted by the cavity model. Flange mount SMA connectors were used for the feed probe driving the antennas. The data for the devices and substrate material are listed in Table 3-1. The first example was designed to be a microstrip antenna with an input impedance of 50Ω at a resonant frequency of 1.15 GHz. The second example was designed to be a half wave resonator of 6.33 cm in length. The resonant frequency would be roughly 1.55 GHz, and any electromagnetic radiation would be undesired.

The skin depth for an imperfect conductor is given by

$$\delta_s = \sqrt{\frac{2}{\omega\sigma\mu}} \tag{3.42}$$

where the conductivity of copper is 5.8×10^7 S/m. At the operating frequencies the skin depths for examples 1 and 2 are 1.95μm and 1.68μm respectively. In both cases the copper plating is many skin depths thick, so only the magnetic current in the radiation model needs to be considered. The equivalent magnetic currents in Fig. 3-6 are found from Eq. (3.20). In the x direction the currents are

$$\mathbf{K}(x,0) = \hat{x}\, d \sum_{m=0}^{\infty} A_m \cos(k_x x) = \hat{x}\, K_x(x,0) \quad , \quad 0 \le x \le a \tag{3.43a}$$

$$\mathbf{K}(x,b) = -\hat{x}\, d \sum_{m=0}^{\infty} B_m \cos(k_x x) = \hat{x}\, K_x(x,b) \quad , \quad 0 \le x \le a \; . \tag{3.43b}$$

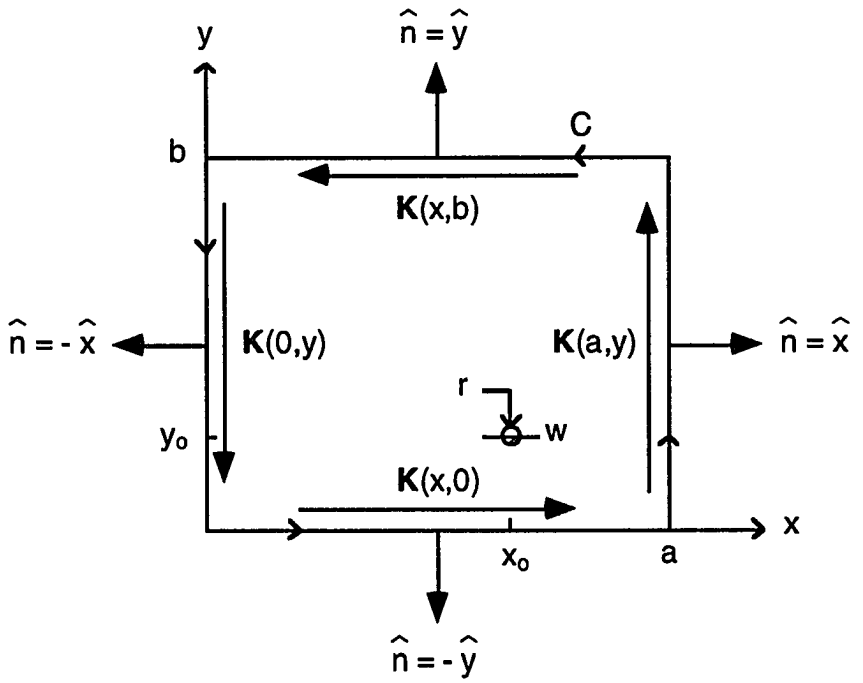

Figure 3-6. Magnetic current density distributions.

Table 3-1. Microstrip antenna and Rogers RT/Duroid parameters

Parameter	Value
a (example 1)	8.53 cm
b (example 1)	12.6 cm
x_o (example 1)	2.04 cm
y_o (example 1)	5.03 cm
a (example 2)	6.33 cm
b (example 2)	1.27 cm
x_o (example 2)	0.92 cm
y_o (example 2)	0.62 cm
Feed type	coaxial
Feed radius/width	254 μm
Thickness	711μm
Plating	Copper: 35.6 μm
Dielectric constant	2.33
Loss tangent	~ 0.001

The magnetic currents in the y direction are equal to

$$\mathbf{K}(0,y) = -\hat{y}\, d \begin{cases} \sum_{m=0}^{\infty} A_m \cos(\beta_m y) & , \quad 0 \le y \le y_o \\ \sum_{m=0}^{\infty} B_m \cos\beta_m (y-b) & , \quad y_o \le y \le b \end{cases} = \hat{y}\, K_y(0,y) \tag{3.44a}$$

$$\mathbf{K}(a,y) = \hat{y}\, d \begin{cases} \sum_{m=0}^{\infty} (-1)^m A_m \cos(\beta_m y) & , \quad 0 \le y \le y_o \\ \sum_{m=0}^{\infty} (-1)^m B_m \cos\beta_m (y-b) & , \quad y_o \le y \le b \end{cases} = \hat{y}\, K_y(a,y) \qquad . \quad (3.44b)$$

Since differential vector dl follows path C with a positive right hand sense it will always be parallel with the magnetic current, and the dot product will be unity. Thus, the Fourier transform defined in Eq. (3.30c) is

$$\tilde{K}_x = d \sum_{m=0}^{\infty} \left[A_m \int_0^a e^{jux} \cos(k_x x)\, dx - B_m e^{jvb} \int_0^a e^{jux} \cos(k_x x)\, dx \right]$$

which may be simplified to

$$\tilde{K}_x = d \sum_{m=0}^{\infty} \tilde{C}_{xm}(u) \left[A_m - B_m e^{jvb} \right] \qquad (3.45)$$

$$\tilde{C}_{xm}(u) = \int_0^a e^{jux} \cos(k_x x)\, dx = \frac{ju\left[(-1)^m e^{jua} - 1\right]}{k_x^2 - u^2} \quad .$$

The Fourier transform for the y-component of the magnetic current Eq. (3.30d) is

$$\tilde{K}_y = -d \sum_{m=0}^{\infty} \left[A_m \int_0^{y_o} e^{jvy} \cos(\beta_m y)\, dy + B_m \int_{y_o}^{b} e^{jvy} \cos\beta_m (y-b)\, dy \right]$$

$$+ d \sum_{m=0}^{\infty} (-1)^m e^{jua} \left[A_m \int_0^{y_o} e^{jvy} \cos(\beta_m y)\, dy + B_m \int_{y_o}^{b} e^{jvy} \cos\beta_m (y-b)\, dy \right]$$

which also may be simplified.

$$\tilde{K}_y = d\sum_{m=0}^{\infty} \psi_m \left[A_m \tilde{C}_{ym}^{-} + B_m \tilde{C}_{ym}^{+} \right] \tag{3.46}$$

$$\psi_m = (-1)^m e^{jua} - 1$$

$$\tilde{C}_{ym}^{-}(v) = \int_0^{y_o} e^{jvy} \cos(\beta_m y)\, dy = \frac{e^{jvy_o}\left[jv\cos(\beta_m y_o) + \beta_m \sin(\beta_m y_o)\right] - jv}{\beta_m^2 - v^2}$$

$$\tilde{C}_{ym}^{+}(v) = \int_{y_o}^{b} e^{jvy} \cos\beta_m(y-b)\, dy = \frac{jve^{jvb} - e^{jvy_o}\left[jv\cos\beta_m(y_o-b) + \beta_m \sin\beta_m(y_o-b)\right]}{\beta_m^2 - v^2}$$

These equations were evaluated numerically in order to determine the dimensions and feed location of the antenna to obtain the desired input impedance and resonant frequency of 50Ω and 1.15 GHz respectively. The results of this analysis are shown in Fig. 3-7. Since actual losses are often higher than those included in the cavity model, the input impedance antenna was designed to be slightly higher in an attempt to obtain an experimental value of 50Ω. The impedance loci for the devices were measured with an HP8753A network analyzer, and 74.5ps of electrical delay was added to compensate for the length of the SMA connector feed. The measured input impedance for the microstrip antenna in example 1 is plotted in Fig. 3-8. The input impedance is 48.1Ω at a resonant frequency of 1.1446 GHz which are very close to the design values. The theoretical and measured impedance loci for the resonator circuit of example 2 are shown in Figs. 3-9 and 3-10 respectively. Both the cavity model and experiment result in a resonant frequency of 1.5755 GHz, and a parallel resistance of about 1.4kΩ due to radiation, dielectric and conductor losses. Note that the agreement between experiment and theory is excellent in both cases. The measured locations of the higher order modes for example 1 are also in good agreement with theory.

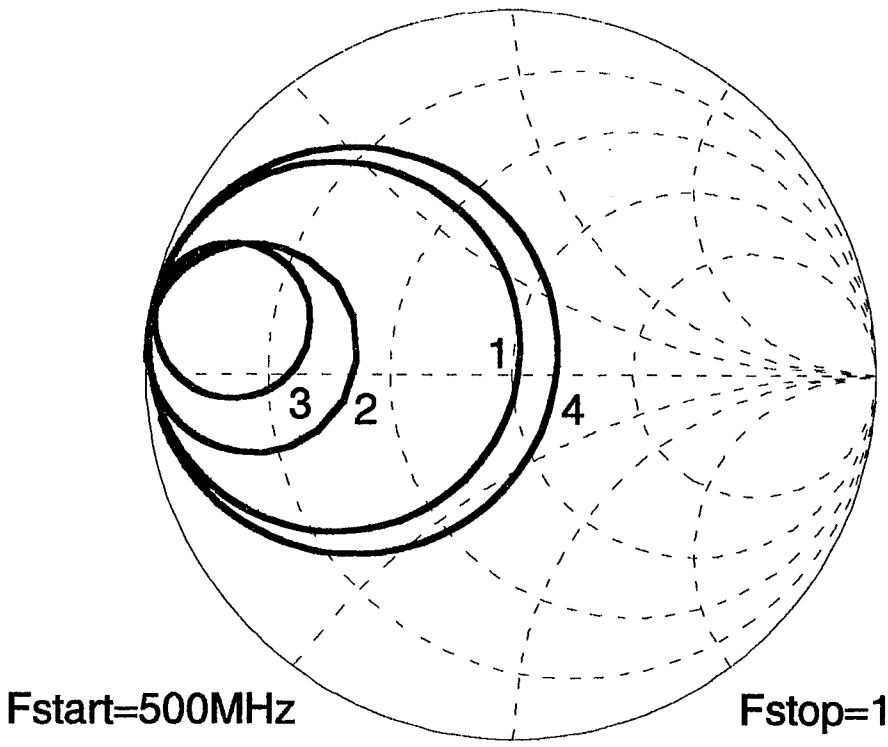

1: TM_{01} mode	2: TM_{10} mode	3: TM_{11} mode	4: TM_{20} mode
51.8Ω	20.2Ω	12.8Ω	64.0Ω
1.145GHz	778MHz	1.385GHz	1.556GHz

Figure 3-7. Predicted microstrip antenna impedance for example 1

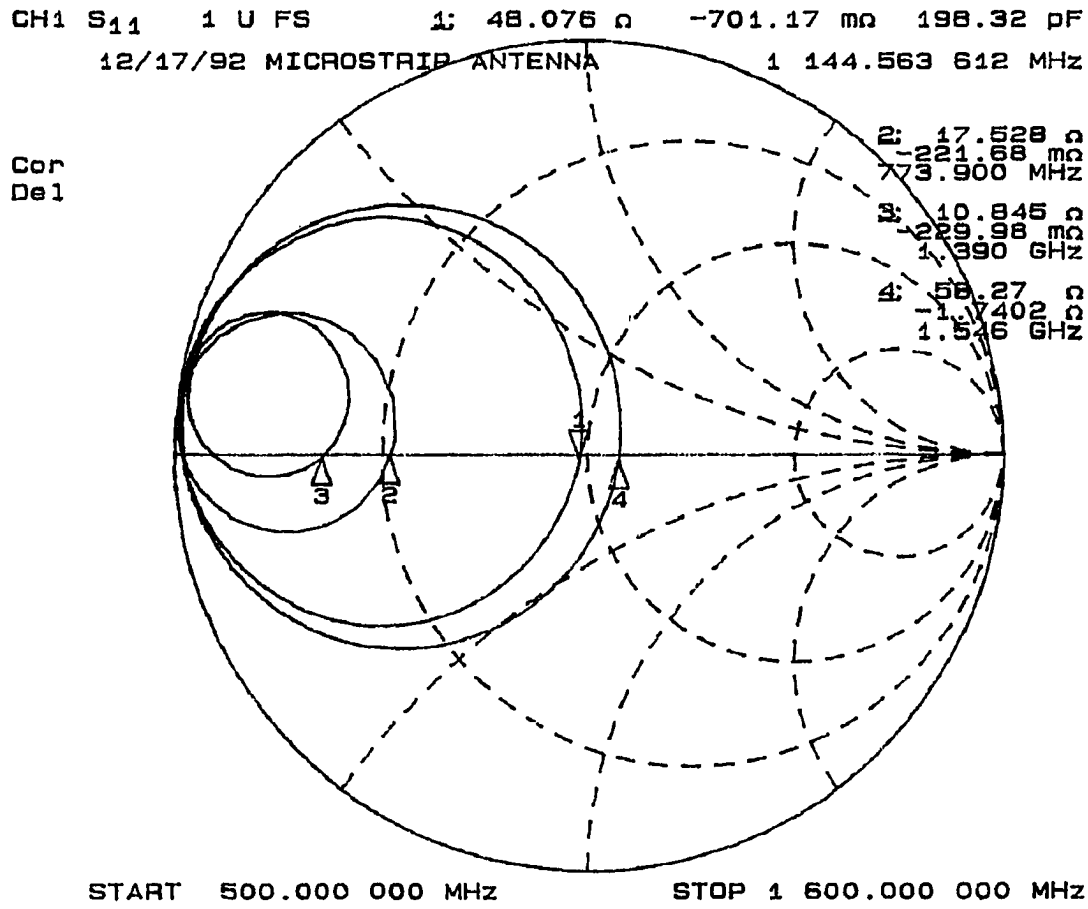

Figure 3-8. Measured microstrip antenna impedance for example 1

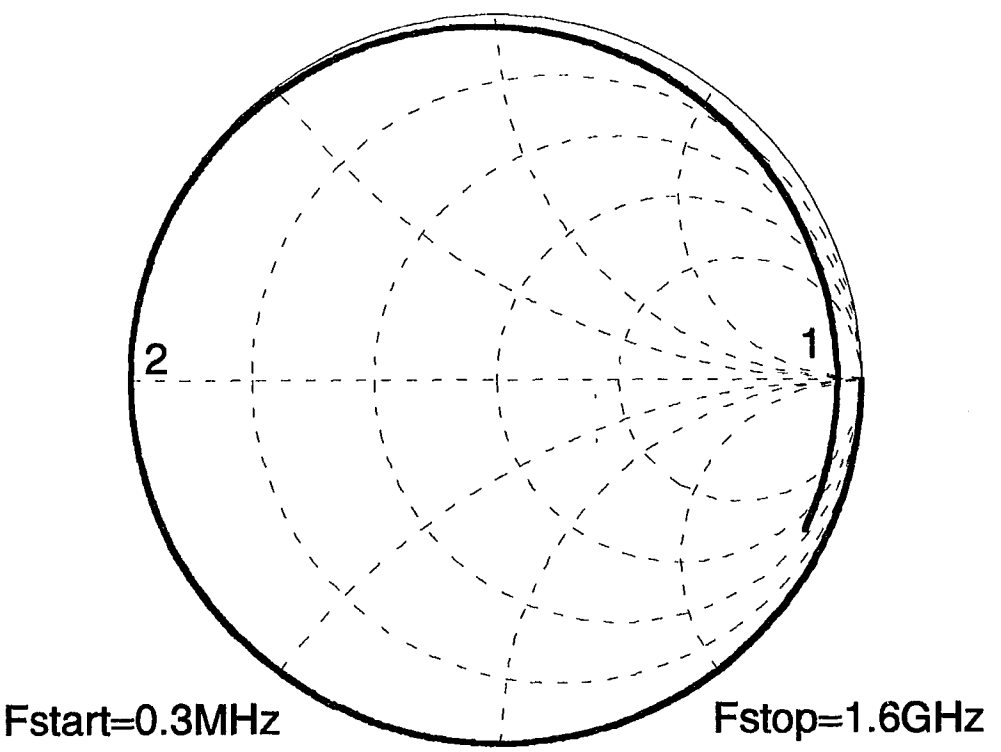

1: Parallel mode
1.463kΩ
1.575GHz

2: Series mode
45mΩ
880MHz

Figure 3-9. Predicted microstrip antenna impedance for example 2

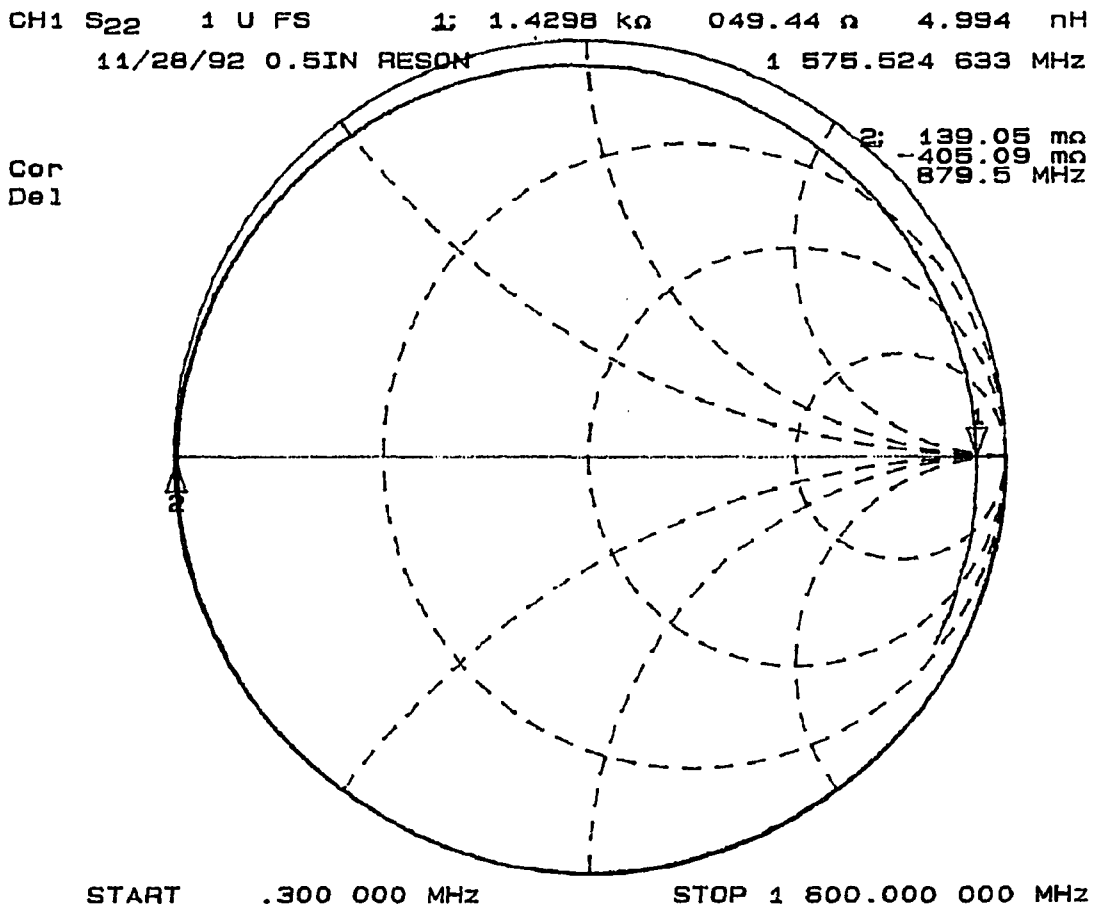

Figure 3-10. Measured microstrip antenna impedance for example 2

CHAPTER 4. RADIATION FROM PIEZOELECTRIC DEVICES

In this chapter a piezoelectric correction will be added to the microstrip antenna analysis discussed in Chapter 3 in order to predict the electromagnetic radiation characteristics of the bulk acoustic wave resonator depicted in Fig. 1-3. The predicted electromagnetic radiation spectrum is experimentally confirmed by measuring the radiated power from quartz and lithium niobate resonators. To the best of this authors knowledge, this is the first time that a bulk acoustic wave resonator has been analyzed as a microstrip antenna with a piezoelectric substrate. Therefore, the work presented in this chapter is believed to be unique, and is the most significant contribution of this thesis.

Single Mode Separation of the Coupled Wave Equation

It is shown in this section that if only one acoustic thickness mode is excited, the coupled wave equation Eq. (2.11) can be approximately separated into a z-dependent acoustic term and an x,y-dependent electromagnetic term. The subscript terminology is employed to specify the coordinates (x_1,x_2,x_3), and is related to the (x,y,z) specification as shown in Table 2-1. The conductor areas of the devices considered in Chapter 2 are electrically small, and the electric field strength is effectively constant over the surface of the conductor. If the conductor area is not electrically small, then the electric field strength may vary over the resonator surface. However, under the quasi-static approximation for piezoelectric devices the acoustic field will only couple to the irrotational part of the externally applied electric field. The irrotational part of the applied electric field is the DC mode which has no x_1 or x_2 dependence. Since the acoustic field couples only to the irrotational part of the applied electric field, under the assumption that only one acoustic thickness mode is excited the acoustic fields within the device will also have no x_1 or x_2 dependence. Thus, for the x_3 dependent acoustic variables the del operator may be approximated by

$$\nabla \approx \hat{x}_3 \frac{\partial}{\partial x_3} . \tag{4.1}$$

Assuming AC steady state fields, from Faraday's law and Ampere's law Eqs. (2.4) and (2.5), the wave equation for the x_3 directed electric field is

$$\nabla \times \nabla \times \mathbf{E} = -j\omega\mu\mathbf{J} + \omega^2\mu\mathbf{D} \tag{4.2}$$

where **J** is the x_3 directed source current density. From Eq. (4.1), the strain is related to the displacement by

$$S_{k3} = \nabla_s u_k = \frac{\partial u_k}{\partial x_3} . \tag{4.3}$$

In Chapter 2 a wave equation Eq. (2.37) was derived for the displacement within the device. Applying Eq. (4.3) to Eq (2.37), the acoustic wave equation may be written in terms of the x_3 dependent strain:

$$\frac{\partial^2 S_{k3}}{\partial x_3^2} + k_A^2 S_{k3} = 0 . \tag{4.4}$$

The subscript "A" has been added to the acoustic wave number so that it will not be confused with the electromagnetic wave number. Since the analysis is for a single acoustic mode, the constitutive relations are

$$D_3 = \varepsilon_{33} E_3 + e_{3k3} S_{k3} \tag{4.5}$$

$$T_{3k} = c_{3kk3} S_{k3} - e_{33k} E_3 . \tag{4.6}$$

Using the vector identity

$$\nabla \times \nabla \times \mathbf{E} = \nabla (\nabla \cdot \mathbf{E}) - \nabla^2 \mathbf{E}$$

and substituting Eq. (4.5) into Eq. (4.2) the coupled wave equation becomes

$$\nabla (\nabla \cdot \mathbf{E}) - \nabla^2 \mathbf{E} = -j\omega\mu \mathbf{J} + \omega^2 \mu(\varepsilon_{33} E_3 + e_{3k3} S_{k3})\, \hat{x}_3 \,. \tag{4.7}$$

From Gauss's law Eq. (2.6), Eq. (4.5) and Eq. (4.1) the divergence of the electric field is approximately equal to

$$\nabla \cdot \mathbf{E} = -\frac{e_{3k3}}{\varepsilon_{33}} \nabla \cdot S_{k3} \approx -\frac{e_{3k3}}{\varepsilon_{33}} \frac{\partial S_{k3}}{\partial x_3} \,.$$

Applying Eq. (4.1) again

$$\nabla (\nabla \cdot \mathbf{E}) \approx -\frac{e_{3k3}}{\varepsilon_{33}} \frac{\partial^2 S_{k3}}{\partial x_3^2} \hat{x}_3 \,.$$

Substituting this result into Eq. (4.7), canceling the x_3 unit vector and expanding the vector Laplacian in rectangular coordinates one obtains

$$\frac{\partial^2 E_3}{\partial x_1^2} + \frac{\partial^2 E_3}{\partial x_2^2} + \frac{\partial^2 E_3}{\partial x_3^2} + \omega^2 \mu \varepsilon_{33} E_3 - j\omega\mu J_3 = -\frac{e_{3k3}}{\varepsilon_{33}} \frac{\partial^2 S_{k3}}{\partial x_3^2} - \omega^2 \mu e_{3k3} S_{k3} \,. \tag{4.8}$$

Newton's law Eq. (2.22) for a single thickness mode is given by

$$\frac{\partial T_{3k}}{\partial x_3} = -\rho\omega^2 u_k \,. \tag{4.9}$$

Equating Eq. (4.9) to the partial with respect to x_3 of Eq. (4.6) one obtains

$$\frac{\partial T_{3k}}{\partial x_3} = c_{3kk3} \frac{\partial S_{k3}}{\partial x_3} - e_{33k} \frac{\partial E_3}{\partial x_3} = -\rho\omega^2 u_k \,.$$

Differentiating this result again with respect to x_3 and using Eq. (4.3) gives

$$c_{3kk3}\frac{\partial^2 S_{k3}}{\partial x_3^2} - e_{33k}\frac{\partial^2 E_3}{\partial x_3^2} = -\rho\omega^2\frac{\partial u_k}{\partial x_3} = -\rho\omega^2 S_{k3} \quad .$$

The second partial of the electric field with respect to x_3 may now be solved for:

$$\frac{\partial^2 E_3}{\partial x_3^2} = \frac{\rho\omega^2}{e_{33k}} S_{k3} + \frac{c_{3kk3}}{e_{33k}}\frac{\partial^2 S_{k3}}{\partial x_3^2} \quad .$$

Substituting this result into Eq. (4.8) and rearranging, the wave equation becomes

$$\frac{\partial^2 E_3}{\partial x_1^2} + \frac{\partial^2 E_3}{\partial x_2^2} + \omega^2\mu\varepsilon_{33}E_3 - j\omega\mu J_3 =$$

$$-\frac{1}{e_{33k}}\left[c_{3kk3} + \frac{e_{33k}\, e_{3k3}}{\varepsilon_{33}}\right]\frac{\partial^2 S_{k3}}{\partial x_3^2} - \frac{\omega^2}{e_{33k}}\left[\mu e_{33k}\, e_{3k3} + \rho\right] S_{k3} \quad . \qquad (4.10)$$

For useful piezoelectric materials:

$$\rho >> \mu e_{33k}\, e_{3k3} \quad .$$

Neglecting this term, the wave equation may be written as

$$\frac{\partial^2 E_3}{\partial x_1^2} + \frac{\partial^2 E_3}{\partial x_2^2} + \omega^2\mu\varepsilon_{33}E_3 - j\omega\mu J_3 = -\frac{\bar{c}_{3kk3}}{e_{33k}}\left[\frac{\partial^2 S_{k3}}{\partial x_3^2} + \frac{\rho\omega^2}{\bar{c}_{3kk3}} S_{k3}\right] \qquad (4.11)$$

where the stiffened elastic constant is

$$\bar{c}_{3kk3} = c_{3kk3} + e_{3k3}\, e_{33k} / \varepsilon_{33} \quad .$$

From Eq. (2.36) the acoustic wave number for a thickness mode is given by

$$k_A^2 = \rho\omega^2 / \bar{c}_{3kk3} .$$

The term in the square brackets of Eq. (4.11) is the one dimensional acoustic wave equation for the strain associated with a thickness mode and from Eq. (4.4) is equal to zero. Substituting Eq. (4.4) into Eq. (4.11), what is left is the two dimensional Helmholtz equation Eq. (3.1).

Thus, under the given assumptions the coupled wave equation may be approximately separated into an acoustic wave equation for the x_3-dependent strain and an electromagnetic wave equation for the x_1 and x_2 dependence. The x_1,x_2-dependent electric field is given by the mode matching solution for the 2D Helmholtz equation and is the externally applied electric field. The total electric field for the device is approximately equal to the superposition of a x_3-dependent acoustic term and the x_1,x_2-dependent electromagnetic term:

$$E_3^{tot}(x_1,x_2,x_3) = E_3(x_1,x_2) + \zeta(x_3) \qquad (4.12)$$

where $E_3(x_1,x_2)$ is the mode matching solution and $\zeta(x_3)$ is defined as the piezoelectric correction factor [7].

To determine the piezoelectric correction, recall that the electric flux density of a thickness mode resonator is completely supplied by the externally applied electric field $E_3(x_1,x_2)$ and is equal to

$$D_3 = \varepsilon_{33}E_3(x_1,x_2)$$

Substituting this result and Eq. (4.12) into Eq. (4.5) one obtains

$$D_3 = \varepsilon_{33}E_3(x_1,x_2) = \varepsilon_{33}[E_3(x_1,x_2) + \zeta(x_3)] + e_{3k3}S_{k3}$$

from which the piezoelectric correction factor is given by

$$\zeta(x_3) = -\frac{e_{3k3}}{\varepsilon_{33}} S_{k3} . \qquad (4.13)$$

Since it is assumed that only a single thickness mode is excited within the device, the displacement field is given by the one dimensional solution Eq. (2.45a), and the strain S_{k3} is then equal to

$$S_{k3} = \frac{\partial u_k}{\partial x_3} = - \frac{I e_{3k3}}{j\omega A \varepsilon_{33} c_{3kk3}} \left[\frac{\cos(k_A x_3 - \theta)}{\cos\theta} \right].$$

The piezoelectric correction factor is then equal to

$$\zeta(x_3) = - \frac{e_{3k3}}{\varepsilon_{33}} S_{k3} = \kappa^2 \frac{I}{j\omega \varepsilon_{33} A} \left[\frac{\cos(k_A x_3 - \theta)}{\cos\theta} \right]. \qquad (4.14)$$

Radiation From Bulk Acoustic Wave Resonators

From Eq. (4.12) the electric field within the device is equal to the mode matching result obtained in Chapter 3 with the addition of a piezoelectrically generated term. The radiated far fields from the piezoelectric term will then have to be vectorially added to the radiated far fields found in Chapter 3. Following the procedure outlined in Chapter 3, the substrate factor for the z-dependent piezoelectric term is

$$i_d^p = \frac{\theta}{k_A^2 - \beta^2} \left[\frac{k_A (\cos \beta d + 1)}{d \cos \beta d} - \frac{\beta \tan \beta d}{d \tan\theta} \right]$$

where the superscript "p" indicates piezoelectric. The radiation model for the piezoelectric term is a loop of constant magnetic current placed on the periphery of the device. The magnitude of this current for a 1A input current is

$$K^p = \int_0^d \zeta(z)\, dz = \frac{\kappa^2 d}{j\omega A \varepsilon_{33}} \left[\frac{\tan\theta}{\theta} \right].$$

Since the piezoelectric term has no x,y-dependence, the Fourier transforms are equal to

$$\tilde{K}_x^p(u,v) = K^p \int_0^a e^{jux} - e^{jvb}\, e^{jux}\, dx = -\frac{K^p}{ju}(1 - e^{jvb})(1 - e^{jua})$$

$$\tilde{K}_y^p(u,v) = K^p \int_0^b e^{jua}\, e^{jvy} - e^{jvy}\, dy = \frac{K^p}{jv}(1 - e^{jvb})(1 - e^{jua})$$

The radiated far fields for the piezoelectric term are found with Eq. (3.29b), however the Fourier transforms and substrate factor with the superscript "p" are used instead of Eq. (3.26), Eq. (3.45) and Eq. (3.46). The entire radiated far fields for the structure are the vector sum of the far fields from the piezoelectric term and the far fields computed in Chapter 3.

The reason for computing an effective quality factor in Chapter 3 was to incorporate the three different electrical loss mechanisms into the impedance calculation. The quality factor of an electromagnetic resonator as defined by Eq. (3.32) only has meaning at the electromagnetic resonant frequency of the cavity. Since the acoustic resonators are not necessarily electromagnetically resonant, the electrical losses will have to be incorporated into the impedance computation by some other means. An effective quality factor could be computed at acoustic resonance, however the only acoustic loss mechanism being considered in this study is viscous damping which can be incorporated into the impedance calculation through a complex elastic constant as in Eq. (2.51). The dielectric losses are included in the field computation by the use of a complex permittivity constant as shown in Fig. 3-1a. Assuming a 1A drive current, the input impedance will be equal to the average voltage over the feed:

$$V_{ave} = \frac{1}{w}\int_{x_o - w/2}^{x_o + w/2} V(x,y_o)\, dx \qquad (4.15)$$

where the rf voltage is

$$V(x,y) = -\int_0^d E_z(x,y) + \zeta(z)\, dz = -dE_z(x,y) - \frac{\kappa^2 d}{j\omega A \varepsilon_{33}}\left[\frac{\tan\theta}{\theta}\right].$$

Through the use of complex parameters, the acoustic and dielectric losses have been included in the calculation of the input impedance using Eq. (4.15). The conductor and radiative losses have not been included in the impedance calculation, and these losses may be modeled by the inclusion of an additional parallel resistance. The conductor and radiation losses for the acoustic resonator are computed with Eq. (3.36) and Eq. (3.37) except the electric field now given by Eq. (4.12). The conductance of this additional parallel resistance is related to these losses by

$$G = \frac{P_c + P_{rad}}{|V_{ave}|^2} . \tag{4.16}$$

The input admittance of the device is then approximately equal to

$$Y_{in} = \frac{1}{Z_{in}} \approx G + \frac{1}{V_{ave}} . \tag{4.17}$$

This approach to estimating the input impedance of a resonator has also been applied to microstrip antennas with good success [22]. The cavity model however produces somewhat more accurate results because the actual complex poles are included in the analysis of the lossy cavity [21,23].

In order to estimate the radiated power from the device, one must consider how the resonator is excited. The actual device is driven by a voltage source with some finite source impedance as shown in Fig. 4-1. Once the input impedance is known, the actual drive current and voltage across the device may be computed:

$$V = V_s \frac{Z_{in}}{Z_{in} + Z_o} \tag{4.18}$$

$$I = V_s \frac{1}{Z_{in} + Z_o}. \tag{4.19}$$

From the calculation of the additional conductance Eq. (4.16), the radiated electromagnetic power for a 1A drive current is available. An estimate of the electromagnetic power that is radiated from the device under the excitation shown in Fig. 4-1 may be obtained by scaling the result for a 1A input current as shown in Eq. (4.20)

$$P_{rad} = P_{rad}^{1A} \frac{|I|^2}{|1A|^2}. \tag{4.20}$$

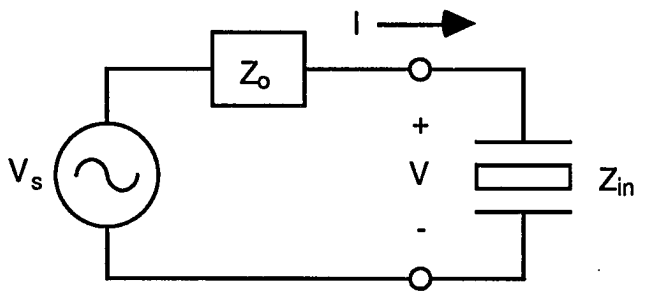

Figure 4-1. Bulk acoustic wave resonator excitation

Electrically Small Bulk Acoustic Wave Resonators

Due to the roughly four orders of magnitude difference between the electromagnetic and acoustic wavelengths in the substrate material, useful bulk acoustic wave resonators are almost always electrically small devices. If the resonators can be assumed to be electrically small, the analysis can be greatly simplified. For an electrically small microstrip circuit, the conductors are equipotential surfaces and only the DC mode is excited. The electric field is then irrotational and is related to the potential function by

$$\mathbf{E} = -\nabla\phi \,.$$

Since the substrate is on the order of half an acoustic wavelength thick, it is electrically thin and the substrate factors given by Eq. (3.22) are approximately equal to zero. In the limit as d approaches zero the expressions for the radiated far fields of an infinitesimal normalized horizontal magnetic current ribbon embedded in a grounded dielectric Eq. (3.25) and Eq. (3.27) reduce to [26]:

$$E_\theta^{hmx}(r,\theta,\varphi) = \frac{j\omega\mu_o}{2\pi\eta_o r} e^{-jk_o r} \sin\varphi \tag{4.21a}$$

$$E_\varphi^{hmx}(r,\theta,\varphi) = \frac{j\omega\mu_o}{2\pi\eta_o r} e^{-jk_o r} \cos\theta \cos\varphi \tag{4.21b}$$

$$E_\theta^{hmy}(r,\theta,\varphi) = -\frac{j\omega\mu_o}{2\pi\eta_o r} e^{-jk_o r} \cos\varphi \tag{4.21c}$$

$$E_\varphi^{hmy}(r,\theta,\varphi) = \frac{j\omega\mu_o}{2\pi\eta_o r} e^{-jk_o r} \cos\theta \sin\varphi \,. \tag{4.21d}$$

The radiation model for the antenna that is shown in Fig. 3-3 consists of a magnetic current ribbon around the periphery of the device. The magnetic current density for an arbitrary electric field is given by Eq. (3.18). From Eq. (3.20), the magnetic current density may be integrated over the substrate thickness to condense the current ribbon into a filamentary magnetic current.

$$\mathbf{K} = \int_0^d \mathbf{M}_s(z)\, dz = \int_0^d \mathbf{E} \times \hat{n}\, dz = (\hat{z} \times \hat{n}) \int_0^d E_z\, dz = -V(\hat{z} \times \hat{n}) \tag{4.22}$$

The radiation model therefore reduces to a loop of magnetic current placed around the periphery of the device, and the magnitude of the magnetic current is

equal to the voltage applied to the resonator. The total radiated far fields are now expressed as [26]:

$$E_\theta(r,\theta,\varphi) = \frac{j\omega\mu_o e^{-jk_o r}}{2\pi\eta_o r}\left[\tilde{K}_x(u,v)\sin\varphi - \tilde{K}_y(u,v)\cos\varphi\right] \tag{4.23a}$$

$$E_\varphi(r,\theta,\varphi) = \frac{j\omega\mu_o e^{-jk_o r}}{2\pi\eta_o r}\cos\theta\left[\tilde{K}_x(u,v)\cos\varphi + \tilde{K}_y(u,v)\sin\varphi\right] . \tag{4.23b}$$

where the Fourier transforms of the magnetic current are defined in Eq. (3.30). The radiated fields are functions of the voltage across the resonator which can be computed with Eq. (4.18) once the input impedance of the device is known. The radiated electromagnetic power may be estimated for a general electrically small bulk acoustic wave resonator as long as the input impedance function is available. Since the conductors are assumed to be equipotential surfaces and the electric field conservative, this formulation is valid for a general resonator. A three dimensional resonator is a multiple mode structure, and its electric field will be some complicated function of x,y and z. However, since the electric field is conservative, the line integral from one conductor to the other over any arbitrary path is equal to the voltage applied to the conductors. Thus, if the impedance of the resonator is available via a finite element computation or measurement, Eq. (4.22) is still valid as long as the device can be considered electrically small.

Bulk Acoustic Wave Resonator Radiation Examples

Consider an electrically small resonator having the same topology as the device shown in Fig. 3-6. The Fourier transforms are

$$\tilde{K}_x(u,v) = -V\int_0^a e^{jux} - e^{jvb}\,e^{jux}\,dx = \frac{V}{ju}(1 - e^{jvb})(1 - e^{jua})$$

$$\tilde{K}_y(u,v) = -V\int_0^b e^{jua}\,e^{jvy} - e^{jvy}\,dy = -\frac{V}{jv}(1 - e^{jvb})(1 - e^{jua})$$

and the radiated far fields become

$$E_\theta(r,\theta,\varphi) = \frac{V\omega\mu_o e^{-jk_o r}}{2\pi\eta_o r}(1 - e^{jua})(1 - e^{jvb})\left[\frac{\sin\varphi}{u} + \frac{\cos\varphi}{v}\right] \qquad (4.24a)$$

$$E_\varphi(r,\theta,\varphi) = -\frac{V\omega\mu_o e^{-jk_o r}}{2\pi\eta_o r}(1 - e^{jua})(1 - e^{jvb})\cos\theta\left[\frac{\sin\varphi}{v} + \frac{\cos\varphi}{u}\right]. \qquad (4.24b)$$

Thus for the case of a rectangular resonator, the radiated fields may be written in closed form as a function of the voltage across the device. The radiated field strength is directly proportional to the voltage applied to the device, and from the form of Eq. (4.18) one would expect a drop in the radiated power at series resonance and an increase in the radiated power at parallel resonance. To illustrate this point consider the resonator parameters listed in Table 4-1. Assuming that the devices are one dimensional, the input impedances may be estimated with Eq. (2.47) and the voltage across the devices computed with Eq. (4.18). Shown in Figs. 4-2, 4-3, 4-4 and 4-5 are the predicted input impedances for the devices as computed with Eq. (2.47), and the radiated power spectrums near the resonant modes for a 10V source with a 50Ω source impedance. As expected, for both cases there is a sharp drop in the radiated power at series resonance. There is also a rise in radiated power at parallel resonance, however, the increase is large for the lithium niobate device but barely visible for the quartz resonator. This is because the lithium niobate resonator has a lower impedance then the quartz device, and the increase in the voltage across the resonator due to the impedance increase at parallel resonance is much greater.

Both the mode matching method Eq. (4.20) and the electrically small technique Eq. (4.24) were used to compute the radiated power spectrums for the resonators being considered. For the quartz device, the power curves generated by the two different methods lay directly on top of one another as evident in Fig. 4-3. This implies that the electrically small approximation is very accurate for the quartz device near the fundamental mode resonance. For the case of the lithium niobate device, the two power curves can be resolved as shown in Fig. 4-5.

This is because the device is being operated at a higher frequency (~22.8MHz), and lithium niobate has a higher dielectric constant (ε_r=29) than quartz. The lithium niobate device is electrically larger than the quartz resonator and thus a more efficient radiator. This is why the mode matching method predicts a slightly larger amount of radiated power than the electrically small technique. The electrically small approximation for this example is less accurate. However, the values computed from the two methods differ by less than 1%, and the electrically small assumption still provides a good estimate of the total radiated power.

Table 4-1. Bulk acoustic wave resonator parameters

Parameter	AT quartz	Z lithium niobate
Mode	shear	longitudenal
Resonance	fundamental	1st overtone
a (cm)	5.0	5.0
b (cm)	5.0	5.0
d (μm)	292	485
c (N/m^2)	$29x10^9$	$245x10^9$
e (C/m^2)	-0.095	1.3
ε (F/m)	$3.63x10^{-11}$	$25.667x10^{-11}$
ρ (kg/m^3)	2650	4640
η ($N{\cdot}s/m^2$)	$8x10^{-2}$	$5x10^{-4}$
tanδ	0.0028	0.0028
f_s (MHz)	5.664	22.779
f_p (MHz)	5.684	22.806

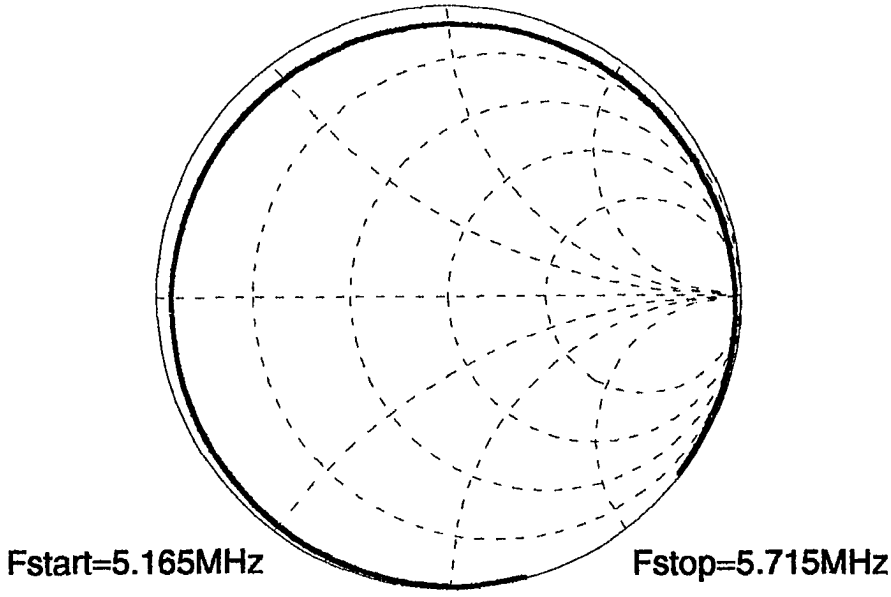

Figure 4-2. Predicted input impedance for the AT-quartz resonator

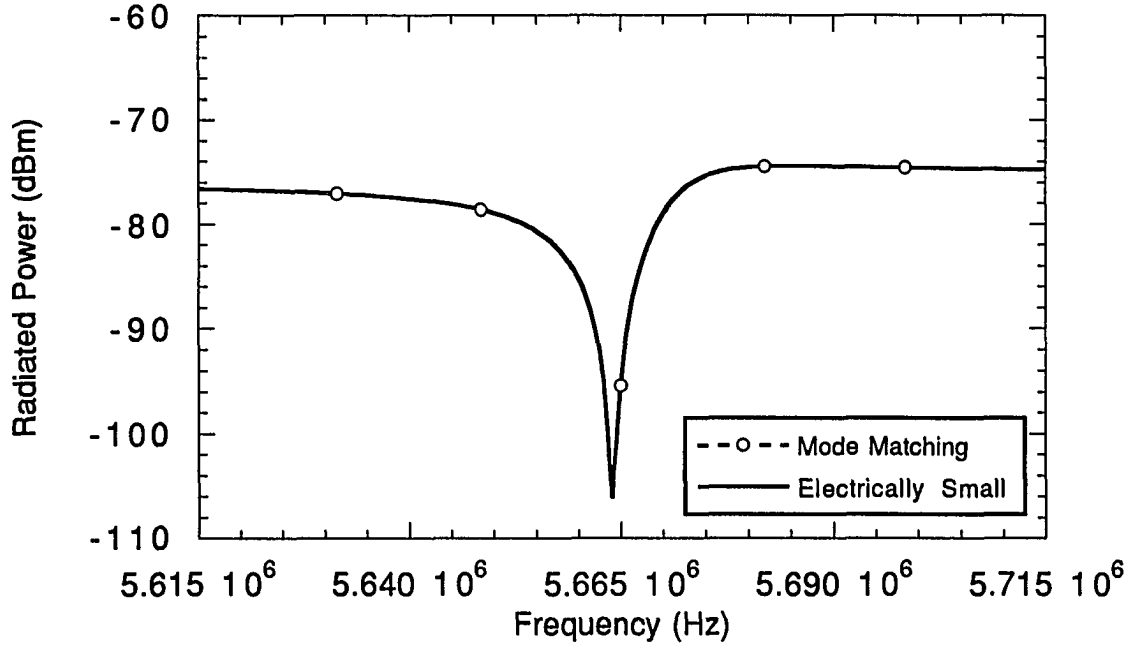

Figure 4-3. Predicted radiated EM power for the AT-quartz resonator

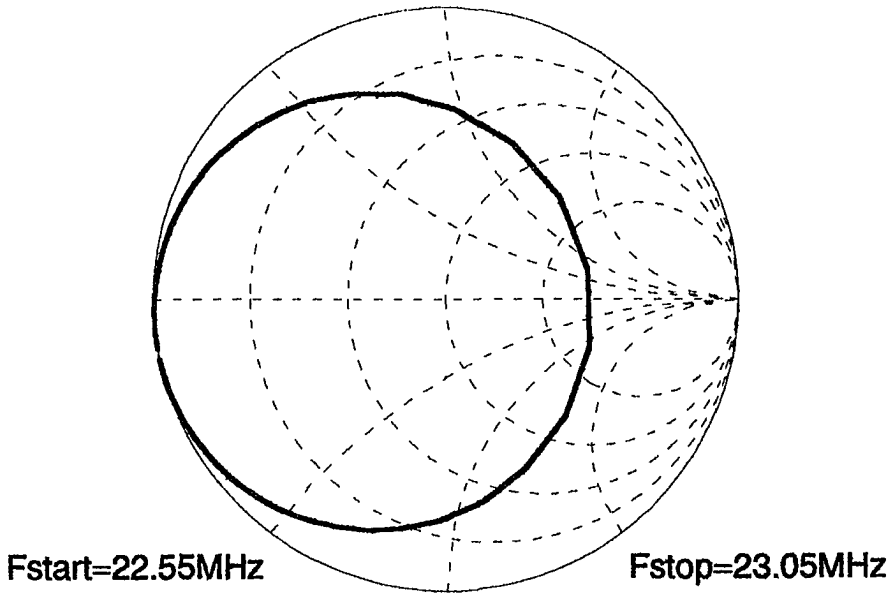

Figure 4-4. Predicted input impedance for the lithium niobate resonator

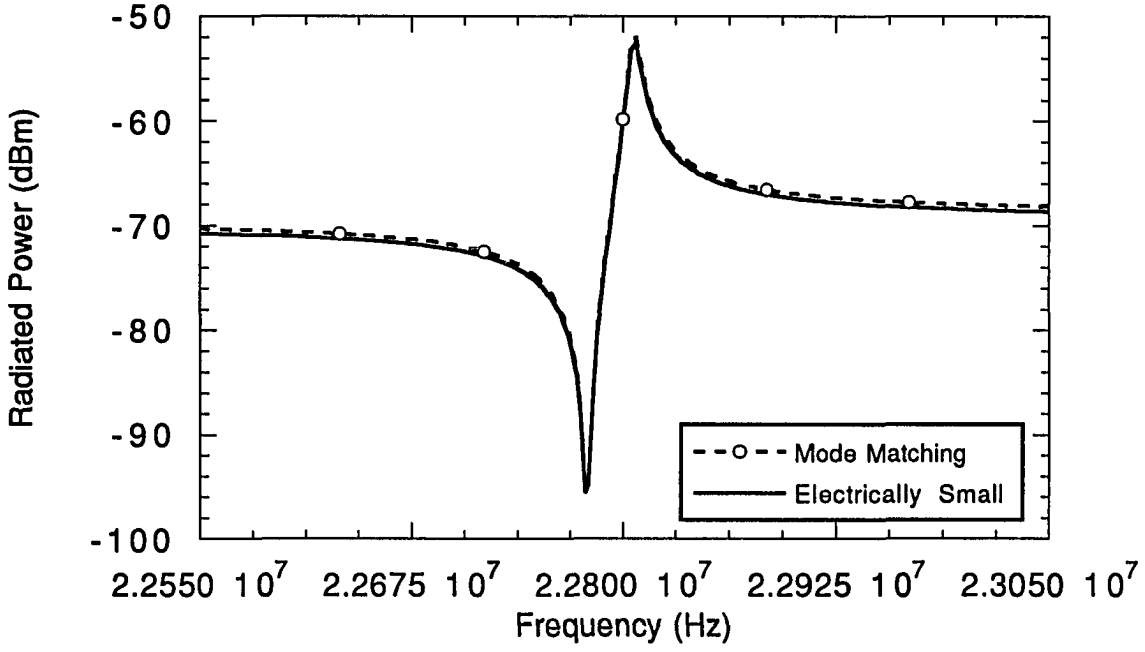

Figure 4-5. Predicted radiated EM power for the lithium niobate resonator

In order to verify the theoretical results, the resonators specified in Table 4-1 were fabricated on three inch wafers. The wafers were completely metalized on one side with approximately 0.5μm of aluminum. Using the same metalization, a 5cm by 5cm resonator with a 1.0cm by 0.6cm feed line was patterned on the other side as shown in Fig. 4-6. A block diagram for the test setup to measure the electromagnetic power being radiated from the devices is shown in Fig. 4-7.

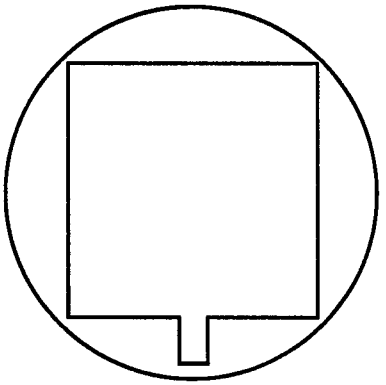

Figure 4-6. Bulk acoustic wave resonator topology

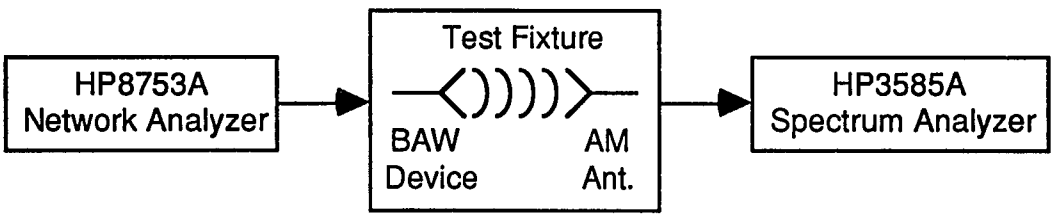

Figure 4-7. Test setup for measuring the radiated power spectrum

The resonator and receive antenna are mounted on a test fixture which is illustrated in Fig. 4-8. The resonator being tested is clamped to a copper clad printed circuit board. The clamps, with ordinary pencil eraser as a padding material, gently press the ground plane side of the wafer to the copper cladding making an electrical contact. The entire surface of the copper clad board is then the ground plane for the experiment. A 5.2cm by 5.2cm hole was cut in the board underneath of the resonator in order to provide a traction free surface for the back side of the device. The excitation is provided via a 10cm piece of 0.085in coaxial transmission line. An SMA connector is mounted on one end of the line, and the shield and dielectric have been stripped away from the other end exposing the center conductor. The outer shield of the line was then soldered to the copper clad board to provide a ground plane contact, and another clamp was used to press the center conductor of the line onto the feed pad of the resonator. The resonator is driven by an HP8753A network analyzer from which the input impedance is measured. On the edge of the board, an AM loopstick antenna is mounted about 12cm above the ground plane. The terminals of the antenna are connected to another SMA connector which serves as the input to an HP3585A spectrum analyzer. Electromagnetic radiation emanating from the device is picked up by the AM antenna and detected with the spectrum analyzer. The spectrum analyzer was set in a peak hold mode so that the detected radiated power may be displayed as a function of frequency.

The goal of this experiment was to verify the shape of the radiation spectrum predicted by theory and not to attempt to measure the total power radiated by the resonator. In other words, the experiment was performed to determine if the radiated power level really does fall off at series resonance and increase at parallel resonance. The absolute magnitude of the measured power spectrums cannot be compared with what is predicted by the theoretical calculation for the following reasons. First, what is predicted by theory is the total power radiated by the device where the Poynting vector has been integrated over the entire upper half space. In the experimental results, just the power picked up by the AM antenna is plotted. It would be very difficult if not impossible at these frequencies to experimentally integrate the total radiated power over the upper half space. Such a measurement would have to be performed in an anechoic

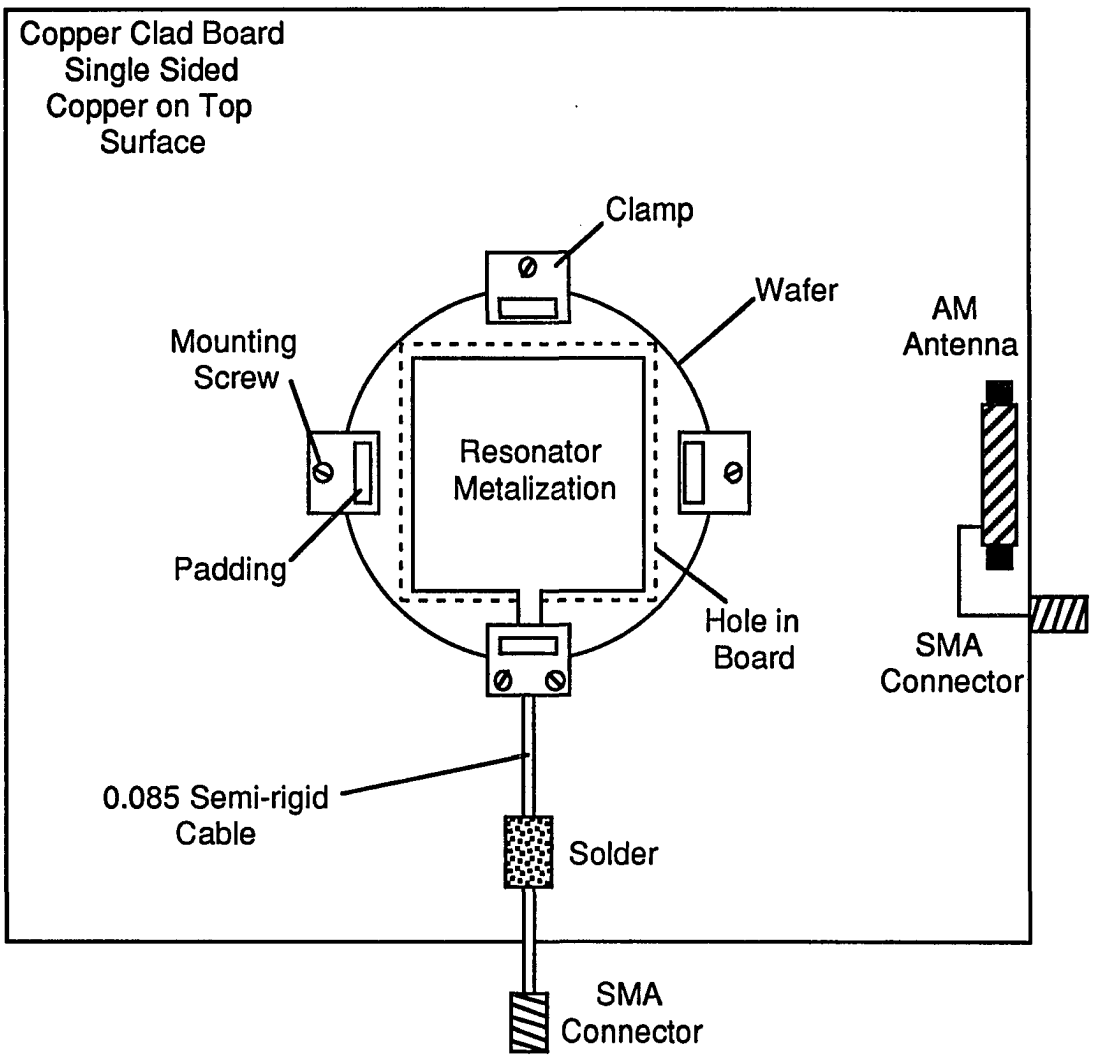

Figure 4-8. Bulk acoustic wave resonator test fixture

chamber and would require a complete characterization of the AM antenna. Second, the frequencies where these devices operate (5MHz~22MHz) are considerably higher than the frequency range that the AM antenna was designed for (~1MHz). Some of the incident power to the AM antenna is probably being reflected and not being detected by the spectrum analyzer. Third, the measurements were not made in an anechoic chamber, therefore reflections from various objects in the lab could alter the amount of power detected by the spectrum analyzer. Also, the distance separating the resonator from the AM antenna is only about 15cm which is probably not in the far field of either device. The theoretical calculation computes only the far fields of the antenna. If one were not in the far field, the $1/r^2$ power law would not be obeyed and the measured power would differ from what would be predicted by theory. With all of the above points in mind one could not hope to experimentally measure the total amount of power that was radiated from the bulk acoustic wave resonator.

The measured input impedances for the resonators are plotted in Figs. 4-9 and 4-10. The output power of the network analyzer was set to 23dBm in order to get the detected signal level well above the noise floor of the spectrum analyzer. The agreement between theory and measurement is fairly good except for the spurious modes which are not predicted by the one dimensional theory. The loss and thickness parameters listed in Table 4-1 were optimized to obtain agreement with the measured data. The experimental radiated power spectrums are plotted in Figs. 4-11 and 4-12. The shape of the measured power spectrum is in excellent agreement with the theoretical computation with the exception of the spurious modes. As predicted, at series resonance there is a rapid decrease in the radiated power from the resonators, and at parallel resonance there is an increase in the radiated electromagnetic power. Also consistent with the theoretical results is the relative magnitude of the radiated power increase at parallel resonance, which is large for the lithium niobate device and small for the quartz device. The results of this experiment support the analytical method described in this chapter for the computation of the radiated electromagnetic fields from a bulk acoustic wave resonator in the vicinity of acoustic resonance.

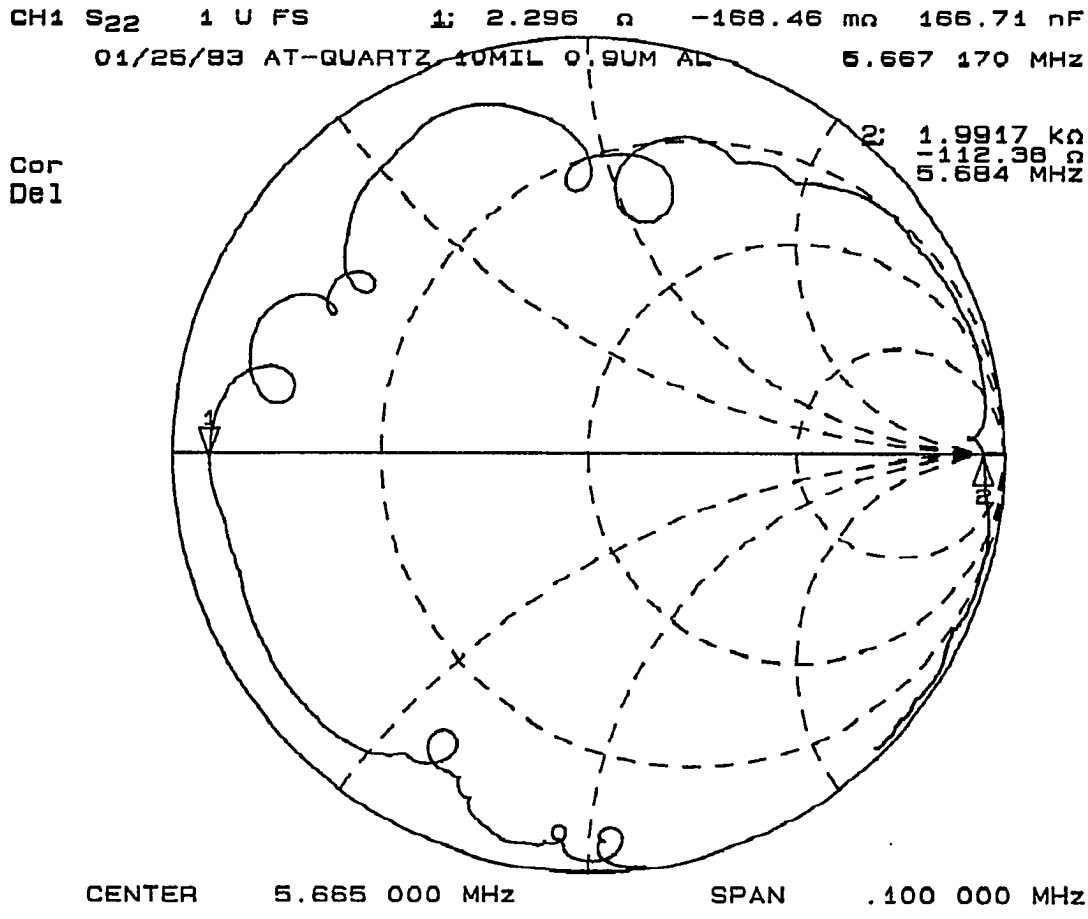

Figure 4-9. Measured input impedance for the AT-quartz resonator

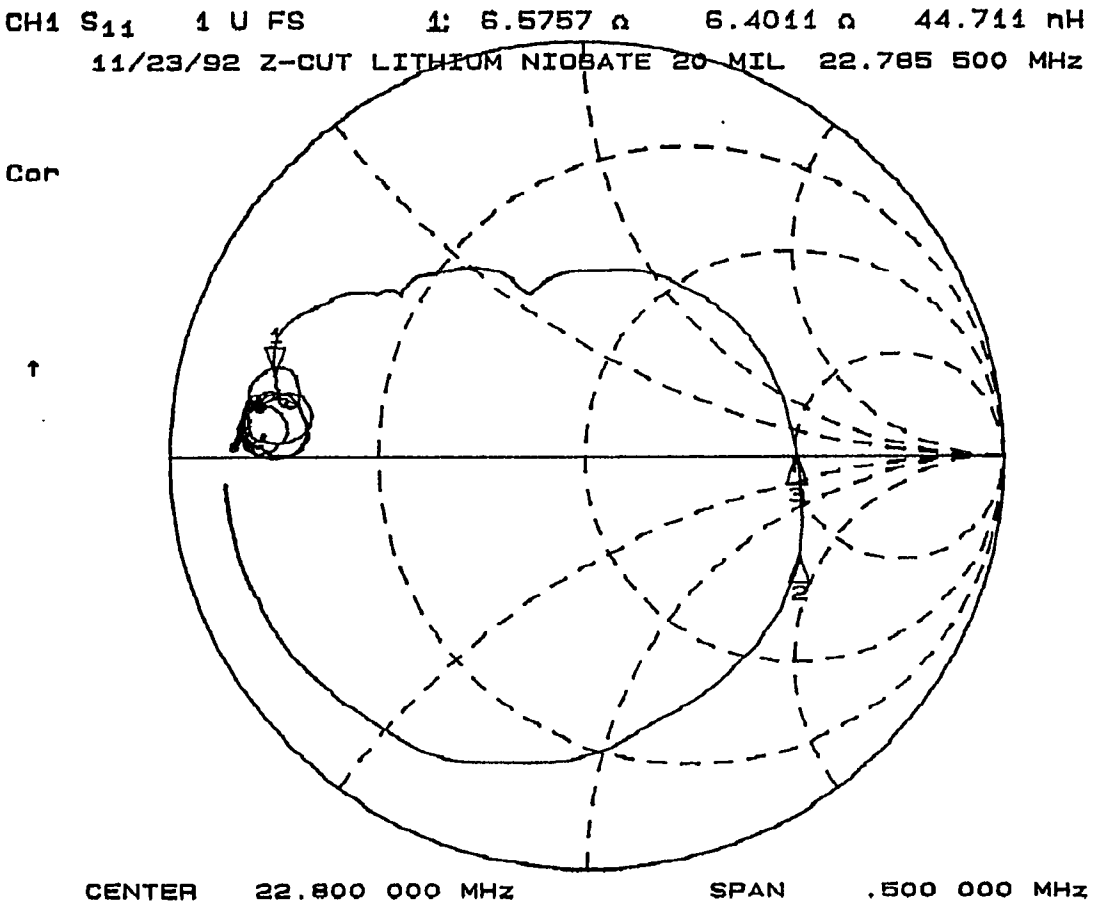

Figure 4-10. Measured input impedance for the lithium niobate resonator

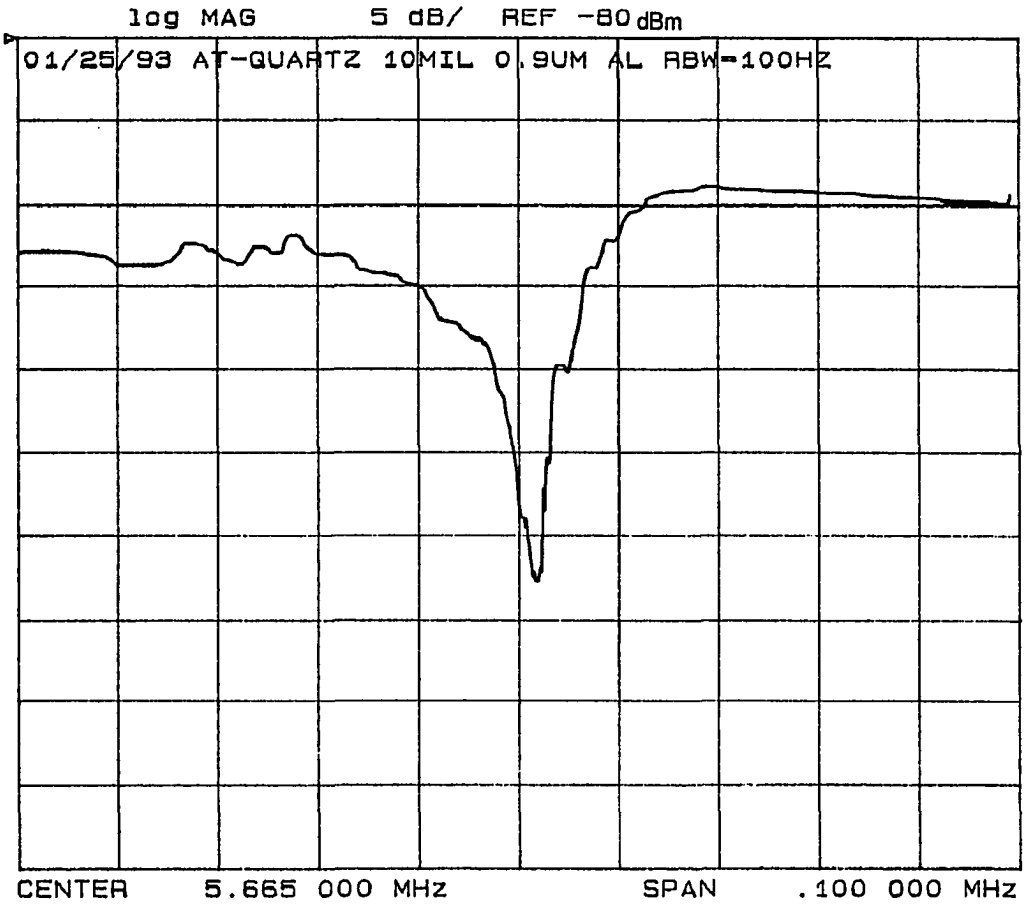

Figure 4-11. Measured radiated EM power for the AT-quartz resonator

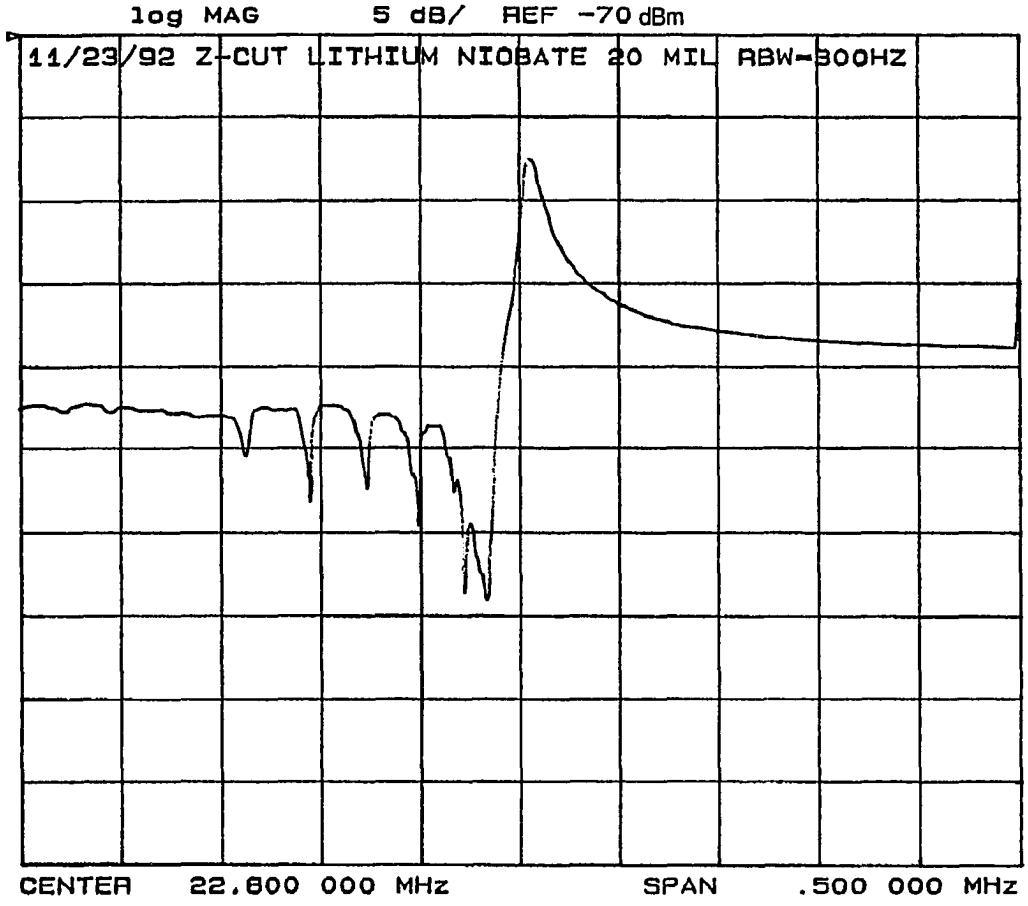

Figure 4-12. Measured radiated EM power for the lithium niobate resonator

CHAPTER 5. INTEGRATED MICROSTRIP ANTENNAS

Thin Metalizations

For the examples in Chapter 3, the copper metalization was many skin depths thick at the operating frequencies of the devices. Aluminum metalizations used in integrated circuit technology are typically 0.1μm to 2.0μm thick. Therefore for examples 1 and 2, a typical integrated circuit metalization would not even be one skin depth thick and the amount of energy dissipated in the conductors would increase. In order to accurately predict the performance of an integrated microstrip antenna, the effect of metalizations which are not many skin depths thick needs to be characterized.

First, consider the interface between a dielectric region and an infinitely thick conducting slab, where the fields in the dielectric region are known. The dielectric fields are computed assuming the conductor to be perfect, and for a microstrip antenna would be those found with the mode matching method. Boundary conditions dictate that the component of the magnetic field tangential to the interface must be continuous. For an interface located at z=0, the magnetic field penetrating into the conductor is given by

$$H = H_{tan}(z=0)\, e^{-\gamma z}$$

where the propagation constant for a good conductor is

$$\gamma = \sqrt{j\omega\mu\sigma - \omega^2\mu\varepsilon} \approx \sqrt{\frac{\omega\mu\sigma}{2}}\,(1+j) \quad . \tag{5.1}$$

The tangential magnetic field at z=0 is found from the mode matching solution. The magnetic field is in the form of a wave traveling into the conductor, and the connection between the magnetic field and the electric field is the intrinsic impedance of the medium. For a good conductor, the intrinsic impedance is

$$\eta = \sqrt{\frac{\omega\mu}{2\sigma}}\,(1+j) \quad . \tag{5.2}$$

For a conductor of thickness t, the metallic slab may be thought of as a transmission line of length t, impedance η and propagation constant γ [31]. Assuming that free space exists on the other side of the conductor, the line is then loaded with a real impedance of 377Ω. The transmission line model for the analysis of a thin conductor is illustrated in Fig. 5-1. The magnetic and electric fields within the conductor are modeled as the current and the voltage on the line respectively. Assuming that the input current i_1 is equal to 1A, the power loss per unit area for the conductor is then equal to

$$R_s = \mathrm{Re}\{v_1 + v_2 i_2^*\}. \tag{5.3}$$

Expressions for the port voltages and output current are easily obtained from the ABCD matrix for a segment of lossy transmission line:

$$v_1 = \eta \coth(\gamma t) - \frac{\eta^2 \mathrm{csch}^2(\gamma t)}{\eta \coth(\gamma t) + 377} \tag{5.4}$$

$$i_2 = \frac{-\eta \,\mathrm{csch}(\gamma t)}{\eta \coth(\gamma t) + 377} \tag{5.5}$$

$$v_2 = \frac{377\eta \,\mathrm{csch}(\gamma t)}{\eta \coth(\gamma t) + 377}. \tag{5.6}$$

Note that in the limit as t grows large, the port parameters approach

$$v_1 \to \eta \qquad v_2 \to 0 \qquad i_2 \to 0.$$

The power loss per unit area per unit current for a thick conductor is then

$$R_s = \mathrm{Re}\{\eta\} = \sqrt{\frac{\omega\mu}{2\sigma}} \tag{5.7}$$

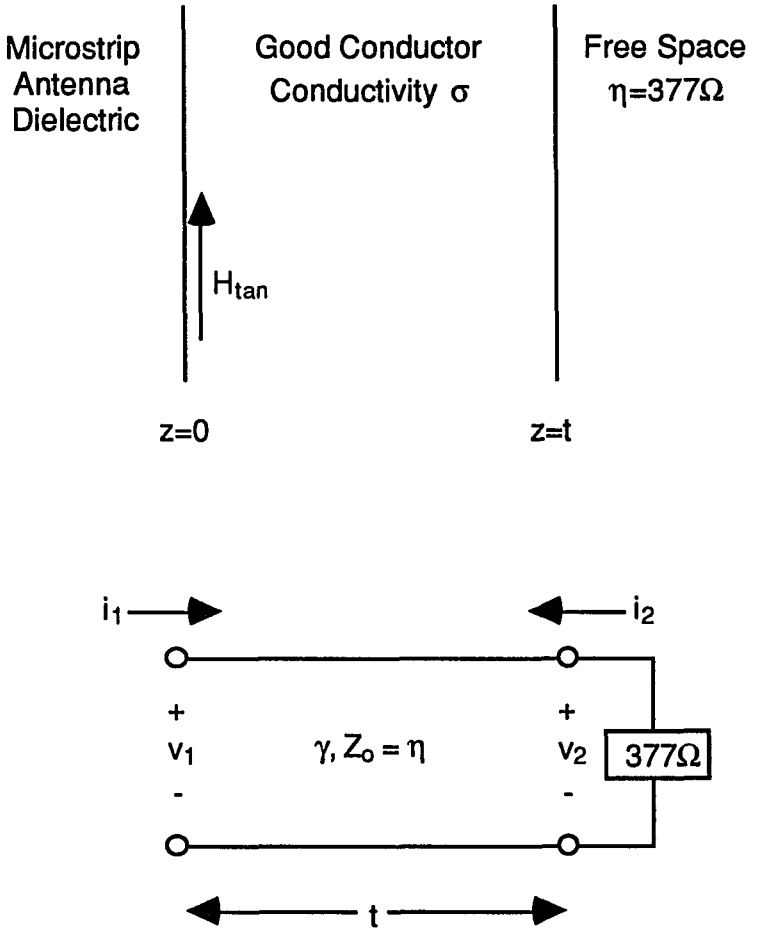

Figure 5-1. Transmission line model for good conductors

which is equal to the classical expression for the surface resistance of a good conductor. Thus, an effective surface resistance for the conducting layer is provided by Eq. (5.3), and the conductor losses are now calculated with

$$P_c = 2R_s \int_S |\mathbf{H}(d)|^2 \, dS \quad . \tag{5.8}$$

Since the thin conductor model is a transmission line model, it is also valid for the multilayer metalizations that are often used in hybrid and integrated microstrip circuits. To analyze multiple layers of different metals one would simply cascade the ABCD transmission line matrices for each layer, and compute the port voltages and output current for a 1A input current. An effective surface resistance is then obtained from Eq. (5.3).

Plots of the effective surface resistance versus conductor thickness for aluminum at frequencies of 1GHz and 2GHz are shown in Fig. 5-2. The losses are very large for extremely thin conductors and decrease rapidly as the conductor is made thicker. These additional losses will cause a decrease in the resonant resistance of the antenna. It appears that for aluminum at these frequencies, a conductor thickness of about 2μm is sufficient, and this metalization is obtainable with current integrated circuit technology. Shown in Fig. 5-3 are plots of the output current i_2 appearing at the other side of the conductor. This represents the current that tunnels through the conductor and would have to be added to the radiation model in Fig. 3-3. Note that with the exception of very thin metalizations, the current which appears on the top surface of the antenna is extremely small in comparison with the current on the bottom surface (i_1 =1A). For typical integrated circuit metalizations, at the frequency range of interest the current on the top surface of the microstrip antenna would radiate a very small amount of power in comparison with the other equivalent sources. Thus, the equivalent surface current on the top side of the antenna is neglected in the calculation of the power radiated from the antenna.

To experimentally confirm the results of the theoretical calculation concerning the effect of the metalization, microstrip antennas where fabricated at the MRC on nominally 254μm thick AT-quartz substrates. Since AT-quartz is

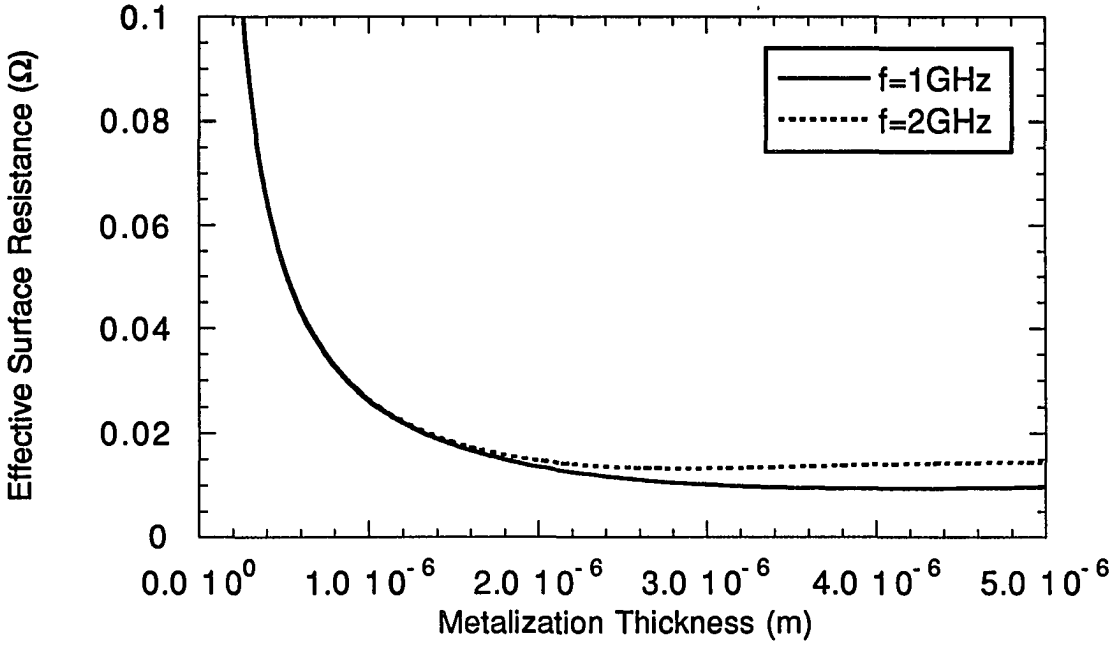

Figure 5-2. Effective surface resistance versus aluminum thickness

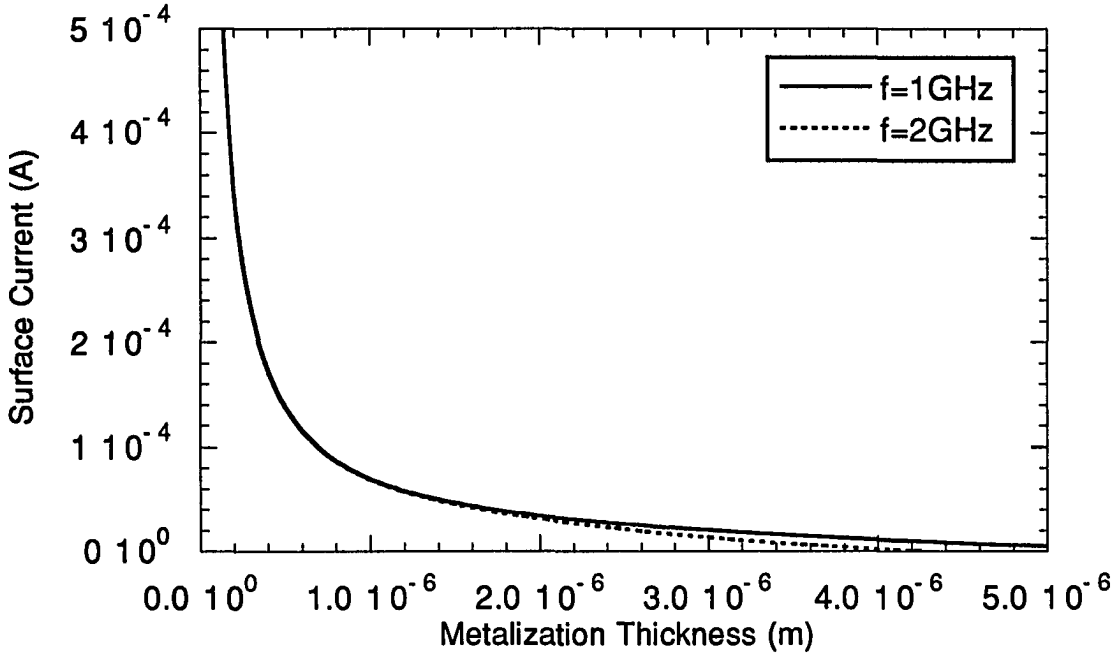

Figure 5-3. Surface current versus aluminum thickness

piezoelectric, the dielectric constant $\varepsilon^T = 4.6\varepsilon_0$ will have to be used in the cavity model calculation [7]. These antennas have exactly the same topology as the quartz resonators shown in Fig. 4-6, and the electromagnetic resonant frequency is about 1.4GHz. Acoustically, the resonator is operating at about the 125th overtone which would be so weakly excited that there would be no measurable effect on the input impedance. In other words, the AT-quartz resonators from Chapter 4 are being characterized as half wavelength long microstrip antennas, and the acoustic wave generation at the electromagnetic resonant frequency is neglected. The aluminum metalization thickness ranged from about 0.3μm to 2.0μm in order to observe of the effect on the resonant resistance of the antennas. The resonant resistance of the microstrip antennas was measured with an HP8753A network analyzer with the wafer mounted in the test fixture shown in Fig. 4-8. The section of coaxial transmission line was compensated for with the addition of 1.0723ns of electrical delay, and the effect of the feed line was backed out of the measured input impedance locus with Libra simulations. The experimental and theoretical results for the resonant resistance are shown in Fig. 5-4. Using Eq. (5.3) for the effective surface resistance, the resonant resistance computed with the cavity model is plotted as the solid curve for a wafer thickness of 254μm. Since the wafer thicknesses were found to vary between 254μm and 305μm, the 305μm curve is also plotted. The measured resistance at resonance for a variety of metalizations appear as the solid dots. Note that the agreement with theory is fairiy good, and all of the measured points fall within the tolerance range for the wafer thickness. The results of this experiment indicate that it is reasonable to model the effect of thin metalizations on microstrip antenna performance with the use of an effective surface resistance given by Eq. (5.3).

Radiation Efficiency

The primary function of an antenna is to radiate electromagnetic energy into free space. The figure of merit describing a particular antenna's ability to perform this function is the radiation efficiency. The radiation efficiency of an antenna is defined as the total radiated real power divided by the total real power absorbed by the antenna. This may be written as follows:

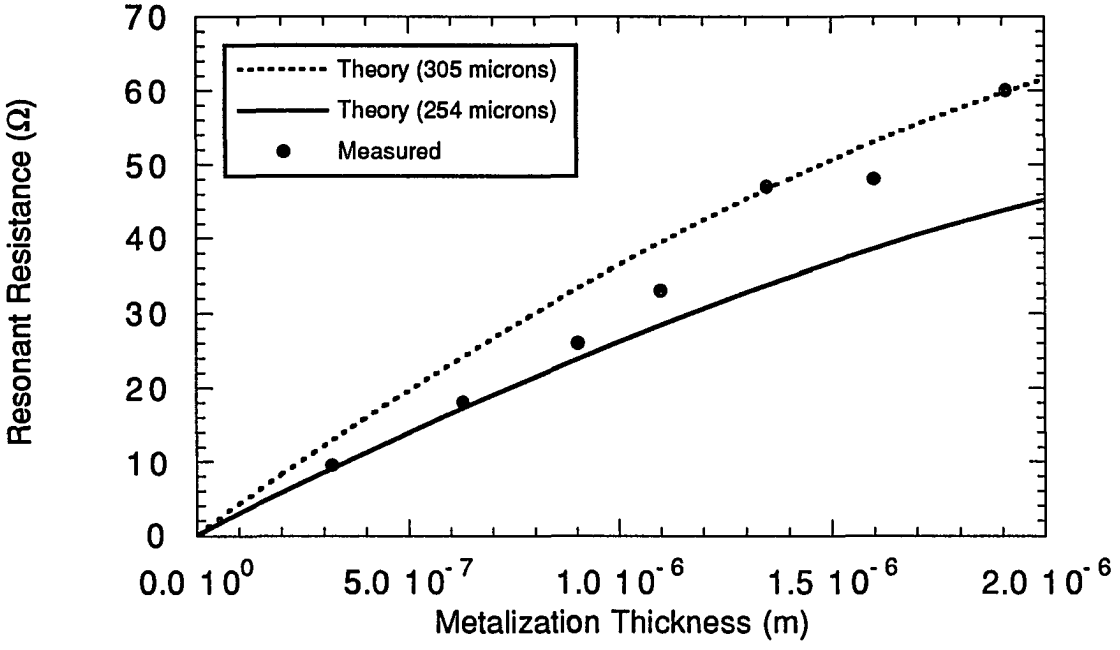

Figure 5-4. Microstrip antenna resonant resistance versus aluminum thickness

$$\xi = \frac{P_r}{P_r + P_d + P_c}. \tag{5.9}$$

The efficiency can also be expressed in terms of the individual quality factors:

$$\xi = \frac{1/Q_r}{1/Q_r + 1/Q_d + 1/Q_c}.$$

At the resonant frequency of the antenna, ω_o, the energies stored in the electric and magnetic fields are equal, and the dielectric and conductor quality factors are

$$1/Q_d = \tan\delta$$

$$1/Q_c = \frac{2R_s}{\mu d \omega_o}.$$

Substituting these results into the efficiency expression gives

$$\xi = \frac{1/Q_r}{1/Q_r + \tan\delta + \dfrac{2R_s}{\mu d \omega_o}}. \tag{5.10}$$

The resonant frequency for the TM_{01} mode is approximately

$$\omega_o = \frac{\pi}{L\sqrt{\varepsilon\mu}} \tag{5.11}$$

where L is the resonant length of the antenna.

Examining Eq. (5.10), in order to make an efficient microstrip antenna the following design rules must be followed. First, from Fig. 5-2, the thinner the metalization the larger R_s becomes which reduces the radiation efficiency of the antenna. Therefore, the metalization layer needs to made thick, such that the

effective surface resistance Eq. (5.3) is approximately equal to the thick metal value Eq. (5.7). Also from the efficiency relation, the antenna becomes more efficient as the substrate thickness, d, is increased. Note that as the substrate thickness approaches zero, so does the radiation efficiency of the microstrip antenna. If the effective surface resistance is reduced, then for a given efficiency, the substrate thickness can also be reduced. One way to reduce the effective surface resistance of the metalization by as many as two orders of magnitude over that of aluminum is to use a superconducting material. The use of superconducting materials could greatly improve the performance of integrated microstrip antennas on electrically thin substrates. Also for a set of microstrip antenna dimensions, the radiation efficiency is reduced for substrates with a high dielectric constant because the resonant frequency ω_o is decreased. Radiation efficiency may also be improved by decreasing the dielectric loss tangent of the substrate material. Another way to increase the radiation efficiency of a microstrip antenna which is not obvious from Eq. (5.10), is to increase the width of the antenna. Making the antenna wider increases the length of the radiating sides thus increasing the amount of power radiated into free space. This has the effect of increasing $1/Q_r$ in Eq. (5.10), and therefore increases the efficiency of the antenna.

Silicon dioxide (SiO_2) layers up to about 25μm thick may be realized with integrated circuit processing techniques and should be considered as a substrate material. As previously mentioned, the radiation efficiency of the antenna may be improved by reducing the dielectric constant and loss tangent of the substrate. A substrate with a dielectric constant near unity and a loss tangent close to zero may be obtained by selectively etching an SiO_2 layer, leaving the conducting patch supported by a series of posts. This is the so called "bed of nails" concept which is illustrated in Fig. 5-5 [1]. To investigate the feasibility of this structure, radiation efficiency versus resonant frequency calculations were made with the following parameters. For the pure SiO_2 substrate the dielectric constant and loss tangent were assumed to be 4.0 and 0.001 respectively [26]. To model the "bed of nails" substrate, a dielectric constant of 1.01 was used along with a loss tangent of 10^{-6}. For both cases the metalization is assumed to be 2μm of aluminum and the width of the antenna is 1.5 times the resonant length.

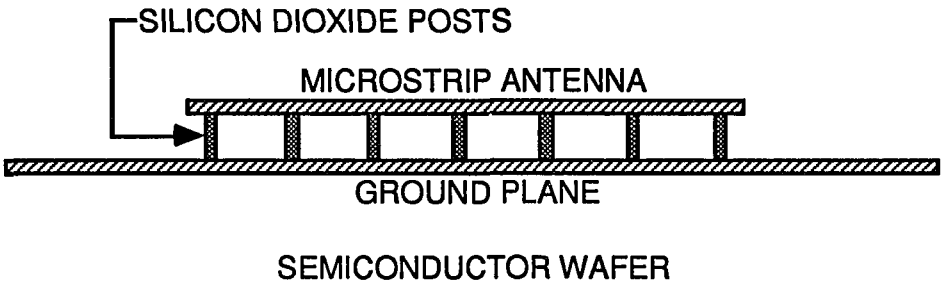

Figure 5-5. "Bed of nails" integrated microstrip antenna substrate concept

The calculations were made for both the pure SiO_2 and the "bed of nails" concepts over a frequency range of 1GHz to 50GHz with substrate thicknesses of 10μm, 15μm, 20μm and 25μm. The results are shown in Fig. 5-6 and Fig. 5-7. Note that in both cases an efficiency level greater than 10% is not realized until the operating frequency of the antenna is extended well above 10GHz. The radiation efficiencies for microstrip antennas on 25μm thick SiO_2 and "bed of nails" substrates were computed to be 0.30% and 0.47% respectively at 2GHz. Thus, for the 1GHz to 2GHz frequency range of interest, neither the pure SiO_2 or "bed of nails" substrate concepts obtain high enough radiation efficiency levels to be used in this work.

The inability to deposit a thick enough layer of dielectric material with standard integrated circuit processing technology is probably the most severe constraint limiting the ultimate performance of an integrated microstrip antenna. Closed cell foams could be used to realize substrates with dielectric constants near unity, and could possibly be deposited in a thick enough layer to overcome the substrate thickness problem without the use of superconductors. A material called thermoset microwave foam (TMF) has received some attention for its application to microstrip antennas [20]. Further investigation is however required to determine if TMF is a good candidate for an integrated microstrip antenna substrate material.

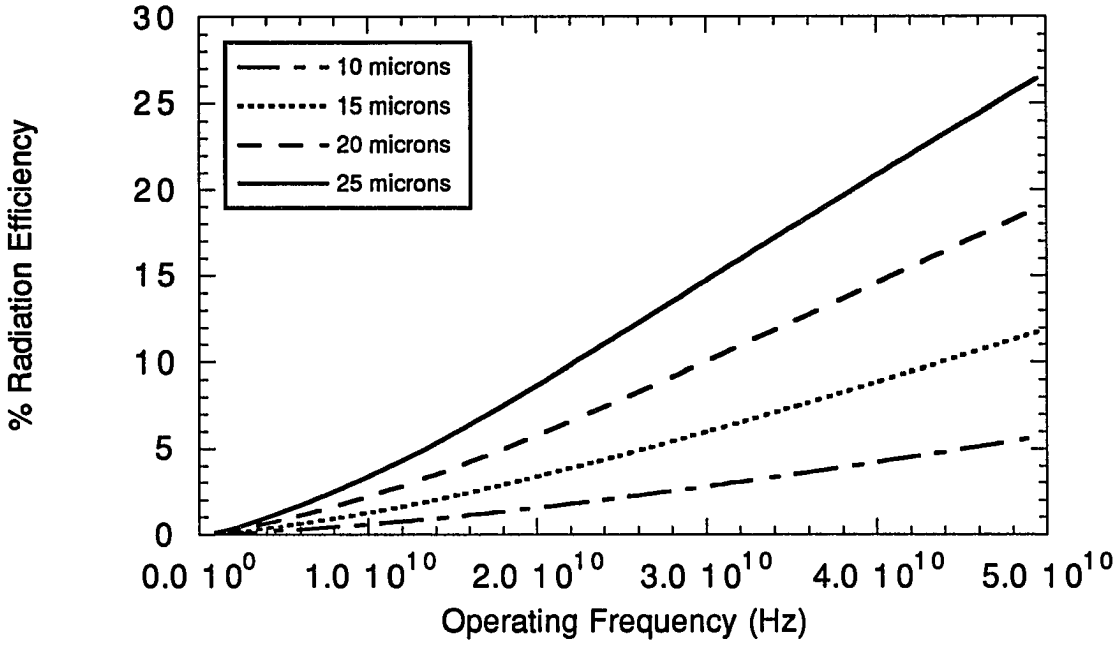

Figure 5-6. Radiation efficiency versus operating frequency: SiO_2

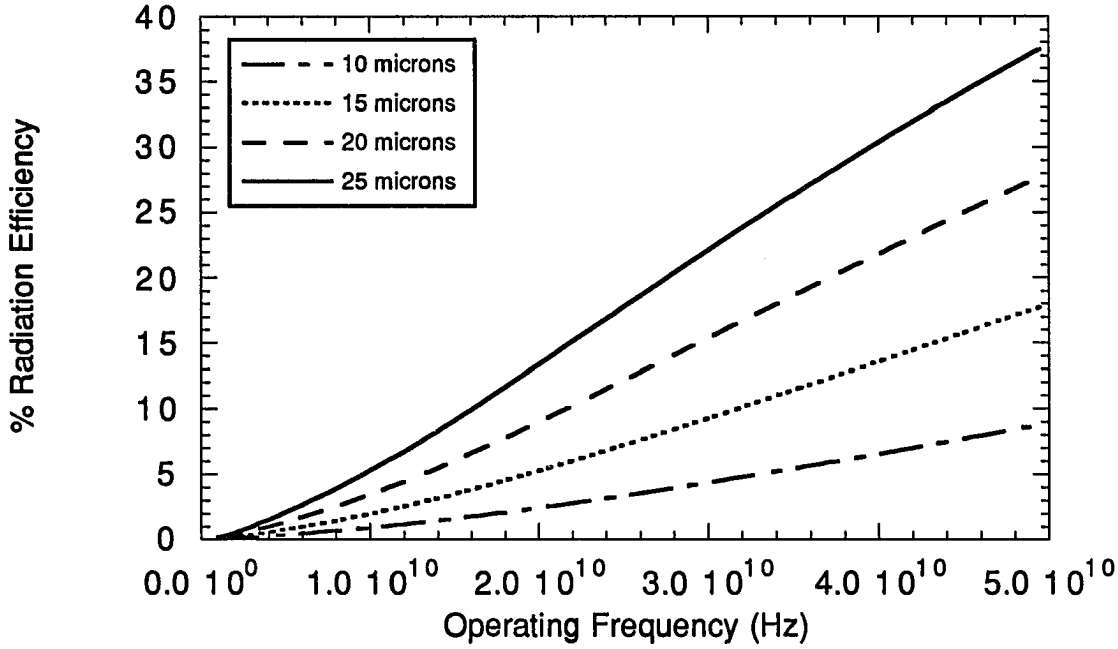

Figure 5-7. Radiation efficiency versus operating frequency: bed of nails

Integrated Microstrip Antenna Design

In this section, the steps required to design an integrated microstrip antenna are discussed. Design examples are presented for aluminum and superconducting metalizations on TMF substrates. Also, an analysis example is presented for an aluminum antenna on a 635μm thick gallium arsenide substrate. For the two design examples, system specifications require the antenna to have a radiation efficiency of at least 50% and it must fit on a three inch semiconductor wafer. The antenna is to be edge fed with a 1mm wide transmission line and have an input return loss greater than 20dB in a 50Ω system.

For the first design example, consider a 6.35cm long aluminum microstrip antenna on a TMF substrate material. The dielectric constant and loss tangent for TMF are approximately equal to 1.4 and 0.0006 respectively [20]. From Eq. (5.11), the resonant frequency of the antenna for the TM_{01} mode is approximately 2GHz. The first step is to determine the required thickness of the aluminum metalization. Examining Fig. 5-2, a 2.0μm thick layer of aluminum will result in an effective surface resistance which is about 98% of the thick metal value. Therefore, a 2μm aluminum metalization will be used. The next step is to use the cavity model at 2GHz and plot the efficiency versus substrate thickness curves for a number of different antenna widths. The results of this calculation are shown in Fig. 5-8, and from these curves the width of the antenna and the substrate thickness may be determined. From the plots, a 508μm thick substrate and 5.08cm wide antenna will satisfy the efficiency and size requirements.

Concerning the next design example, it was mentioned earlier in this chapter that the substrate thickness can be greatly reduced by the use of superconducting materials. To illustrate this point, plotted in Fig. 5-9 are the efficiency versus substrate thickness curves for a thick metalization with a surface impedance of 100μΩ. This metalization parameter is typical for the modeling of high temperature superconducting microstrip circuits [32]. From Fig. 5-9, a 50% radiation efficiency may now be realized with a 5.08cm wide antenna and only a 88.9μm thick TMF substrate. Note that the use of superconductors provides only a modest efficiency improvement for thick substrates.

It was determined where to feed the antennas to obtain a 50Ω impedance match with consecutive cavity model calculations at the resonant frequencies.

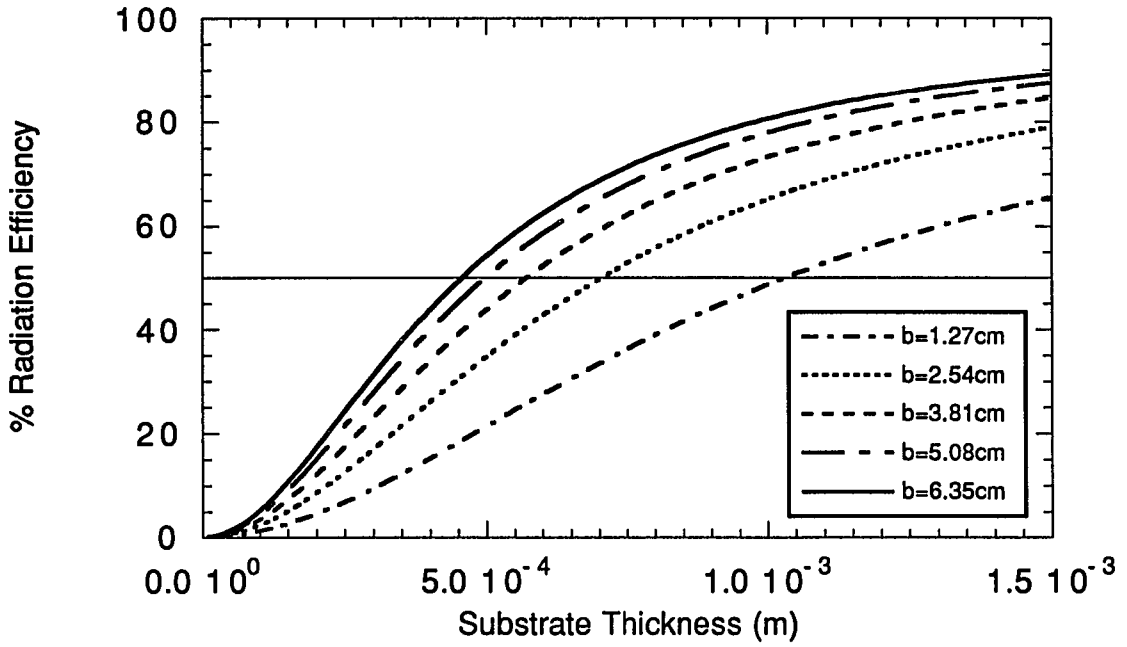

Figure 5-8. TMF/aluminum microstrip antenna radiation efficiency

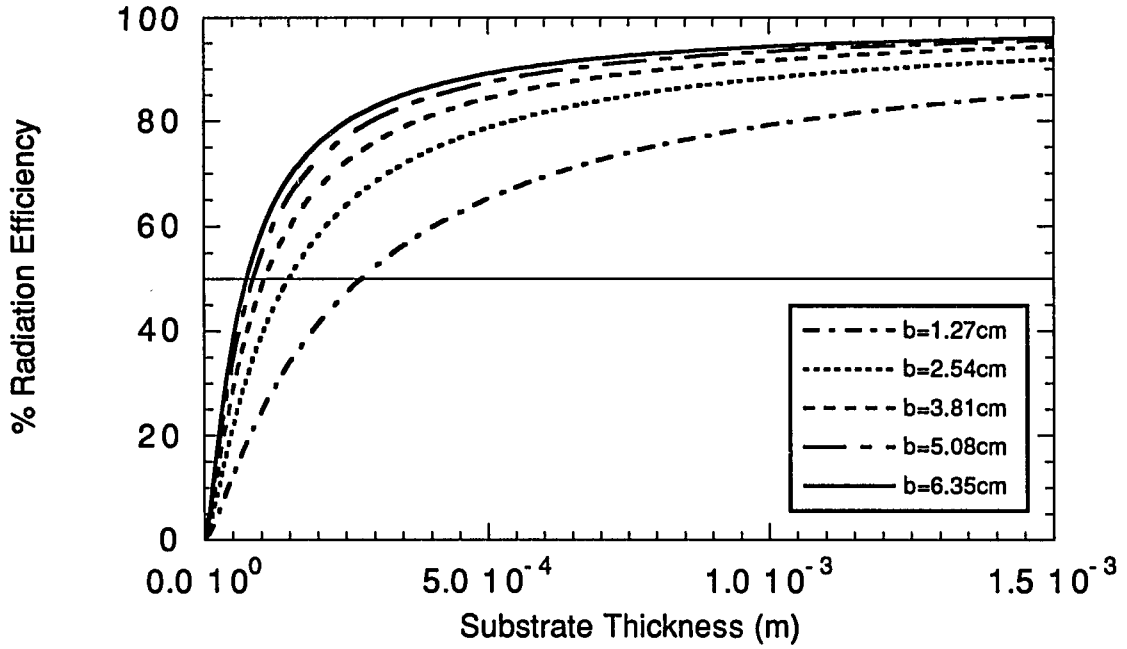

Figure 5-9. TMF/superconductor microstrip antenna radiation efficiency

The design and performance parameters for the two design examples are summarized in Table 5-1. The impedance loci and return loss curves for the antennas are plotted in Figs. 5-10 and 5-11. The computed resonant frequencies are slightly different than the values obtained with Eq. (5.11) due to the fringing fields at edges of the antennas. Both antennas meet the size and return loss specifications. Note that since the superconducting antenna is a high Q device, its bandwidth is considerably less than the aluminum antenna.

One way to overcome the problems associated with depositing a thick enough dielectric layer on top of the semiconductor wafer is to use the semiconductor wafer itself as the microstrip antenna substrate material. Semi-insulating 635μm thick GaAs wafers are available as a stock item and may be thick enough to obtain a reason level of radiation efficiency. Therefore, as a

Table 5-1. Design and performance parameters for the antenna examples

Parameter	TMF1	TMF2	GaAs
a	6.33 cm	6.33 cm	4.37 cm
b	5.08 cm	5.08 cm	1.04 cm
x_o	2.15 cm	2.19 cm	100 μm
y_o	0.00 cm	0.00 cm	0.00 cm
Thickness	508 μm	88.9 μm	635 μm
Plating	aluminum: 2.0μm	superconductor	aluminum: 0.4μm
Dielectric constant	1.4	1.4	13.0
Loss tangent	0.0006	0.0006	0.002
Feed probe	Microstrip: 1.0mm	Microstrip: 1.0mm	Microstrip: 100μm
Resonant frequency	1.984GHz	1.999GHz	995.5MHz
Radiation efficiency	50.5%	50.9%	0.75%
Resonant resistance	50.5Ω	50.4Ω	143.4Ω
3:1 VSWR banwidth	20.0MHz	3.5MHz	———

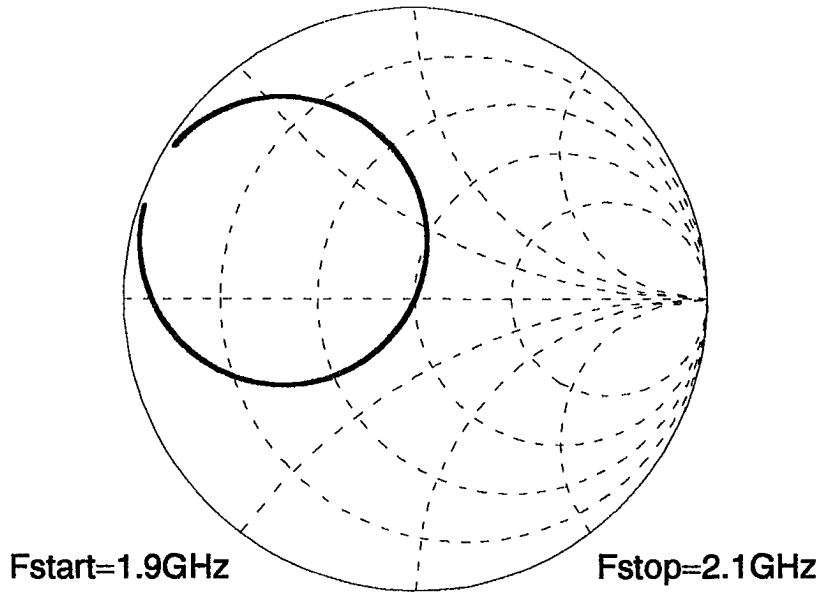

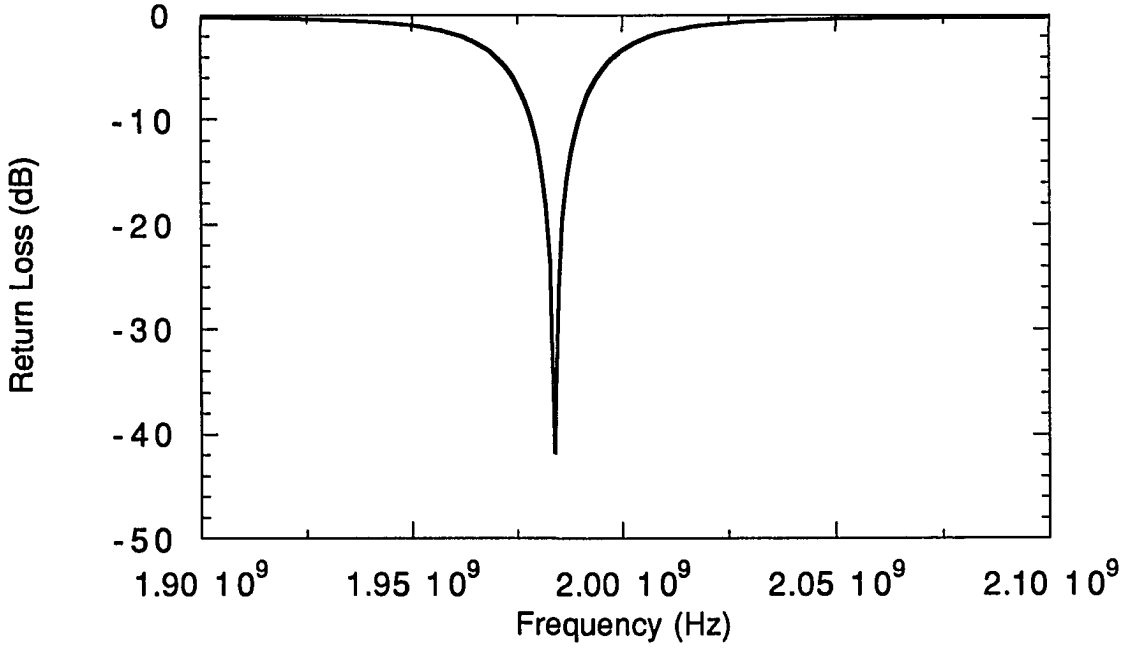

Figure 5-10. Frequency response of the TMF/aluminum microstrip antenna

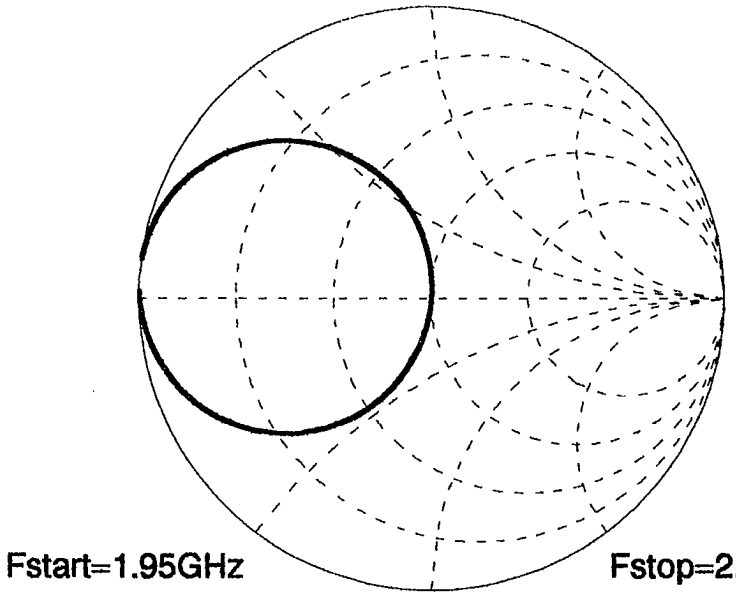

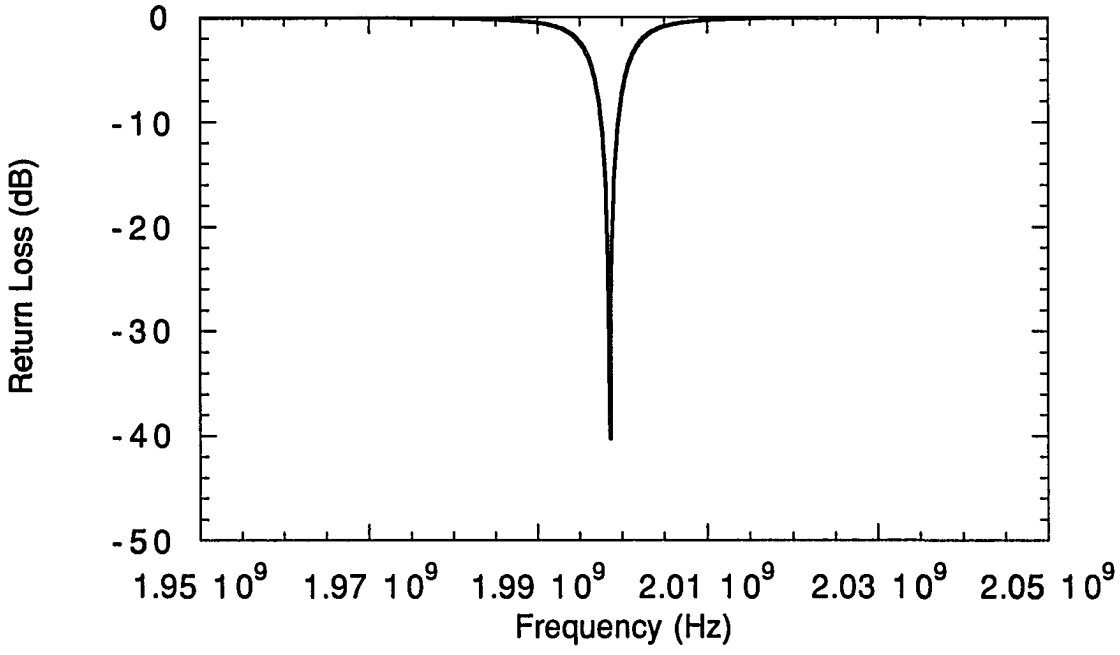

Figure 5-11. Frequency response of the TMF/superconductor microstrip antenna

third integrated antenna example consider the following analysis problem. A 4.37cm by 1.04cm microstrip antenna with 0.4μm thick aluminum metalization on a 635μm thick gallium arsenide substrate where the back side of the wafer is completely covered with the same metalization. The antenna is edge fed with a 100μm wide microstrip line and from Eq. (5.11) has an operating frequency of about 952MHz. An antenna similar to this example is being considered for use in a prototype overmoded acoustically driven antenna system. The antenna parameters are listed in Table 5-1 and the predicted impedance locus of the antenna is shown Fig. 5-12.

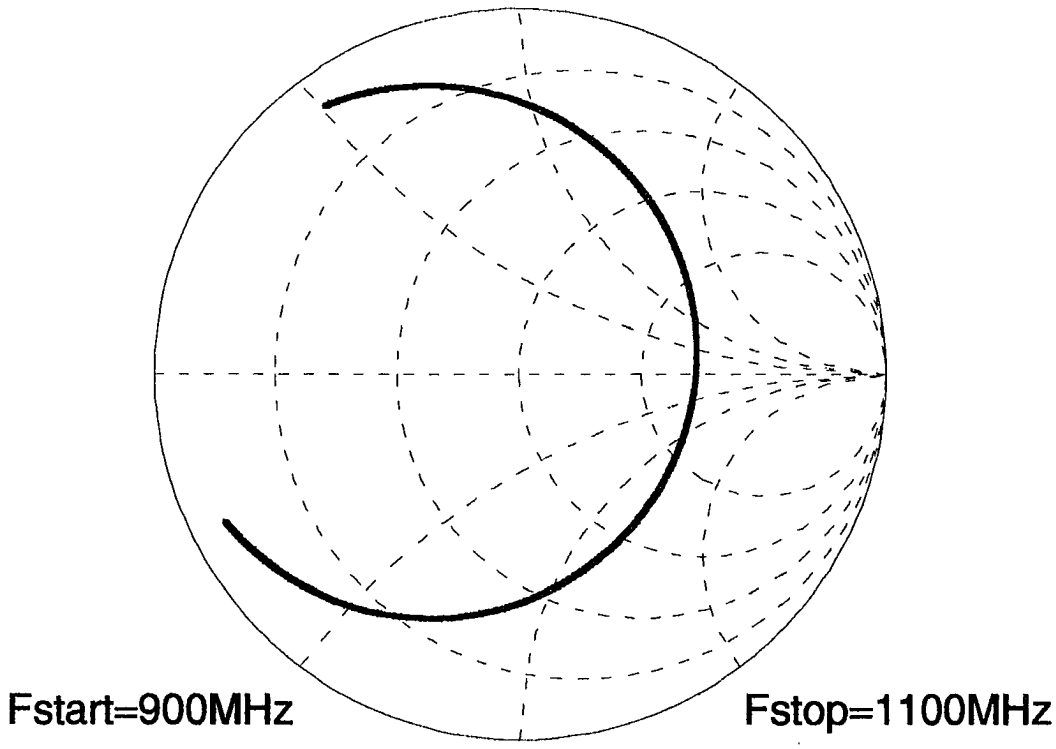

Figure 5-12. Predicted impedance locus for the GaAs microstrip antenna

The computed radiation efficiency of the antenna is only 0.75%. The low efficiency is due in part to the 0.4μm aluminum metalization. Shown in Fig. 5-13 are the efficiency versus thickness curves at 1GHz for a GaAs substrate with a 2.0μm thick aluminum metalization. From the figure, by using a 6.35cm wide microstrip antenna the efficiency could be improved to 12.5%. This is still a relatively inefficient radiator, and it appears that for the frequency range of interest (1GHz-2GHz), the dielectric constant of GaAs is too high for use as a practical microstrip antenna substrate material. At higher frequencies, an efficient microstrip antenna could possibly be constructed on a 635μm thick GaAs substrate.

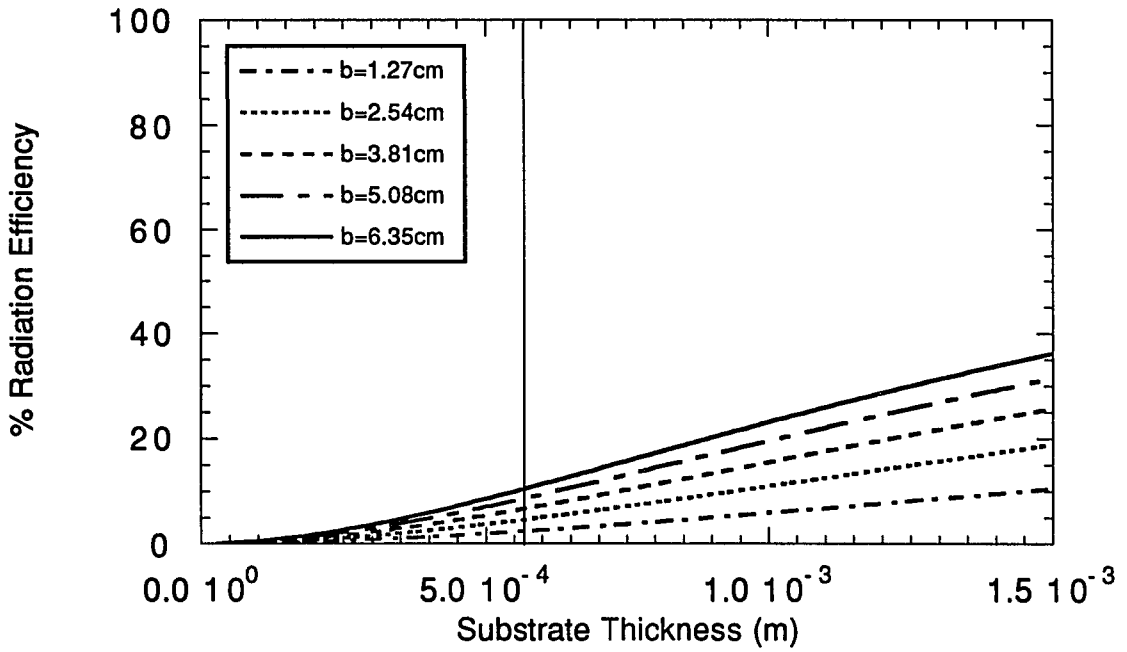

Figure 5-13. GaAs/aluminum microstrip antenna radiation efficiency

Acoustically Driven Integrated Microstrip Antennas

One of the original goals of this work was to analyze the acoustically driven microstrip antenna topologies shown in Fig. 1-1 and Fig. 1-2. The input impedance of the integrated microstrip antenna can be computed with the technique outlined in this chapter, and the y-parameter matrices for the stacked crystal filters were found in Chapter 2. The acoustically driven antenna system can be analyzed as a stacked crystal filter loaded with a microstrip antenna. The two port representation of the system is shown in Fig. 5-14.

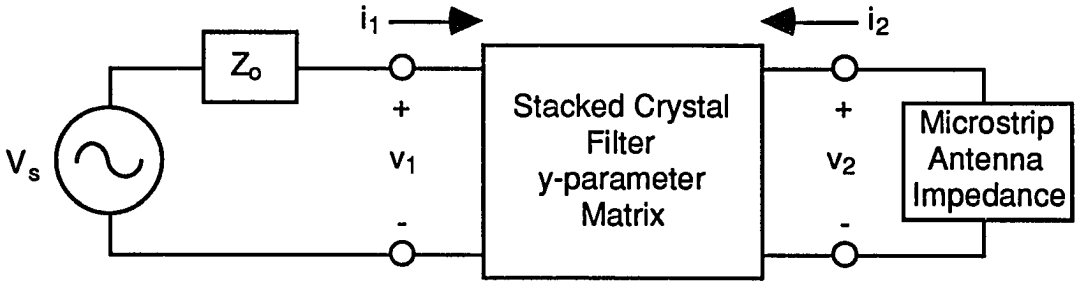

Figure 5-14. Two port representation of the acoustically driven antenna system

The parameters of interest for the system are the input impedance, radiated power, and system efficiency. Let the system efficiency be defined as the ratio of the total real power radiated by the microstrip antenna to the total real power incident from the source to the input of the stacked crystal filter expressed as:

$$\psi = \frac{P_r}{P_{inc}}. \tag{5.12}$$

The input impedance of the system may be computed from the y-parameters as

$$Y_{in} = \frac{1}{Z_{in}} = y_{11} - \frac{y_{12}y_{21}}{1 + y_{22}Z_a} \tag{5.13}$$

where Z_a is the input impedance of the microstrip antenna. The remaining system parameters are determined from the port currents and voltages:

$$i_2 = \frac{y_{21} V_s}{1 + y_{22} Z_a + y_{11} Z_o + Z_o Z_a \Delta} \tag{5.14a}$$

$$v_2 = \frac{y_{21} Z_l V_s}{y_{12} y_{21} Z_o Z_a - (1 + y_{11} Z_o)(1 + y_{22} Z_a)} \tag{5.14b}$$

$$v_1 = \frac{- v_2 (1 + y_{22} Z_a)}{y_{21} Z_a} \tag{5.14c}$$

$$i_1 = \frac{i_2 (y_{11} + Z_o \Delta)}{y_{21}} \tag{5.14d}$$

$$\Delta = y_{11} y_{22} - y_{12} y_{21} .$$

The real power which is absorbed by the microstrip antenna is equal to

$$P_{ant} = - \text{Re} \{ v_2 i_2^* \}$$

where the minus sign indicates that power is being absorbed by the load. From the radiation efficiency section of this chapter, the amount of power that will be radiated into free space by the microstrip antenna is related to the total power absorbed by the antenna through Eq. (5.9). The radiated power is then

$$P_r = \xi P_{ant} = - \xi \text{Re} \{ v_2 i_2^* \} \tag{5.15}$$

where ξ is the radiation efficiency of the microstrip antenna. The amount of real power which enters the stacked crystal filter is given by

$$P_{scf} = \text{Re} \{ v_1 i_1^* \} .$$

The incident real power from the source to the input of the stacked crystal filter is related to the reflection coefficient of the system and power entering the filter by

$$P_{inc} = \frac{P_{scf}}{1 - |\Gamma_{in}|^2} = \frac{\mathrm{Re}\{v_1 i_1^*\}}{1 - |\Gamma_{in}|^2} \tag{5.16}$$

where

$$\Gamma_{in} = \frac{Z_{in} - Z_o}{Z_{in} + Z_o}.$$

Substituting Eq. (5.15) and Eq. (5.16) into Eq. (5.12), the system efficiency is equal to

$$\psi = -\xi (1 - |\Gamma_{in}|^2) \frac{\mathrm{Re}\{v_2 i_2^*\}}{\mathrm{Re}\{v_1 i_1^*\}}. \tag{5.17}$$

As an acoustically driven integrated antenna example, consider a system consisting of an aluminum nitride fundamental mode stacked crystal filter driving the 1.984GHz TMF microstrip antenna that was analyzed in the previous section. From the stacked crystal filter analysis section in Chapter 2, a fundamental mode device operating at 1.984GHz would require 2.81μm thick aluminum nitride layers. The conductor dimensions are made to be 218x218μm to achieve maximum bandwidth in a 50Ω system [6]. The frequency response of the filter is shown in Fig. 5-15 where loss has been included in the calculation with the use of the following complex permittivity and elastic constants:

$$\hat{c}_{33} = (395 + j3.3) \times 10^9 \ \mathrm{N/m^2}$$
$$\hat{\varepsilon}_{33} = (9.5 - j0.25) \times 10^{-11} \ \mathrm{F/m}.$$

The input impedance locus and return loss results for the system are shown in Fig. 5-16. Note that the return loss plot has two nulls, one at the microstrip antenna resonance and another at a slightly lower frequency. Before resonance,

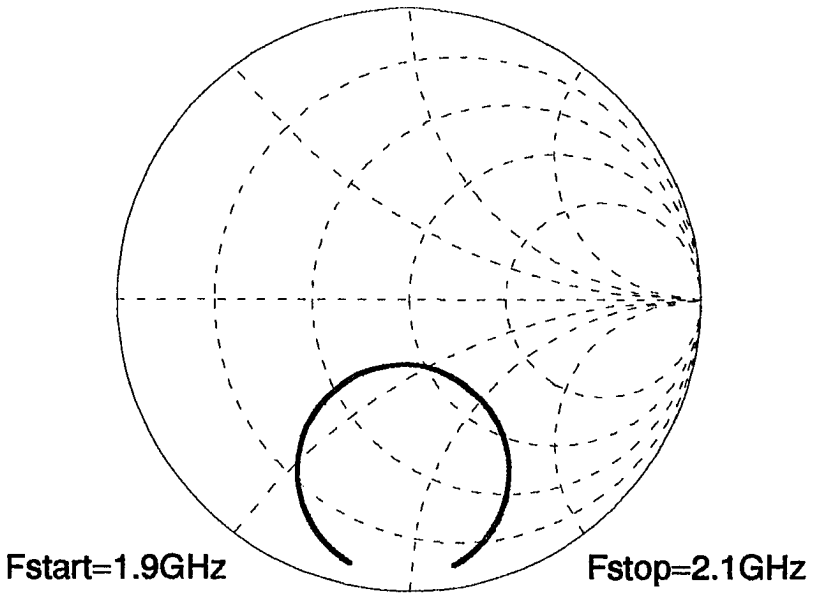

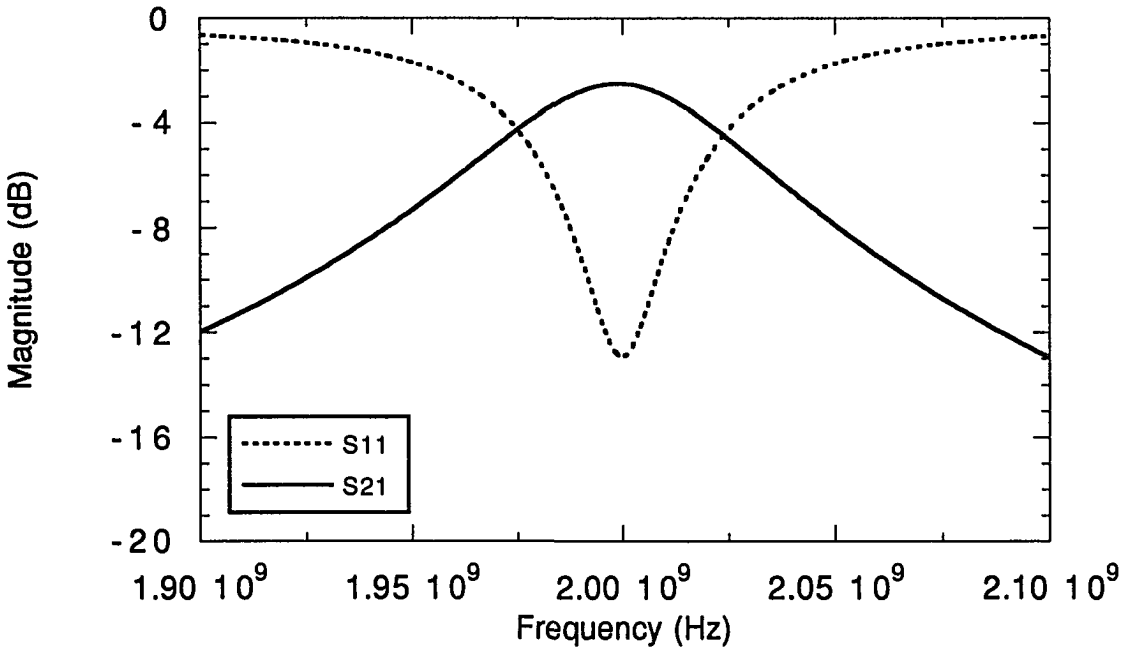

Figure 5-15. Frequency response of the fundamental mode stacked crystal filter

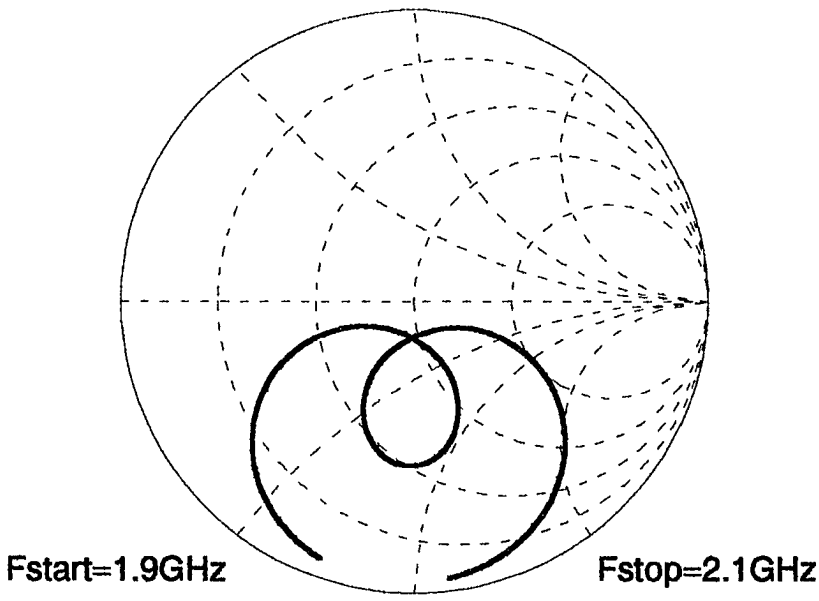

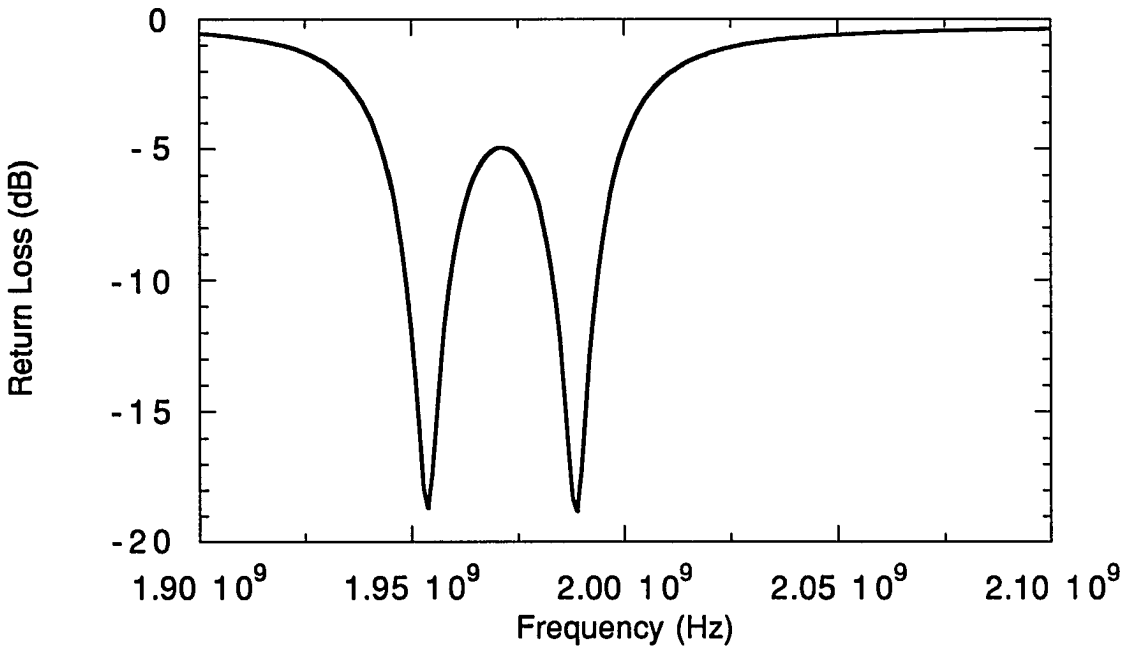

Figure 5-16. Frequency response of the acoustically driven TMF antenna system

the microstrip antenna has an inductive impedance which resonates with the capacitive impedance of the stacked crystal filter. The stacked crystal filter feed circuit therefore has a broadbanding effect on the input impedance of the system. External components may however be required to tune the input return loss of the system in order to maximize the bandwidth. The broadbanding effect can also be seen in the system efficiency and radiated power plots shown in Fig. 5-17 and Fig. 5-18 respectively. A maximum system efficiency of 27.9% was computed at a frequency of 1.982GHz. If the microstrip antenna had a 90% radiation efficiency, then about a 49.7% system efficiency could be achieved. The computed radiated power for a 1V-50Ω source is flat within 0.5dBm over a 33MHz bandwidth.

As a second example, consider an overmoded stacked crystal filter driving the 995.5MHz GaAs integrated microstrip antenna that was analyzed in the previous section. Recall, for this example the GaAs wafer itself is the microstrip antenna substrate. In an overmoded acoustically driven system the GaAs wafer is also the intervening substrate layer between the piezoelectric transducers. The topology of the system is shown in Fig. 5-19. From the overmoded filter analysis presented in Chapter 2, a 995.5MHz device with a 635μm GaAs wafer as the intervening non-piezoelectric layer requires 5μm thick AlN layers. The conductor dimensions for maximum bandwidth in a 50Ω system are 400μm by 400μm [6]. The frequency response of the filter is shown in Fig. 5-20 where loss has again been included by the use of complex coefficients. The complex elastic constant for the gallium arsenide substrate material is given approximately by [7],

$$c_s = (119 + j0.0952) \times 10^9 \text{ N/m}^2 .$$

Note that gallium arsenide is an acoustically lossy material which greatly increases the insertion loss of the overmoded filter. The frequency response of the acoustically driven antenna system is shown in Fig. 5-21. The system efficiency and radiated power plots for a 1V-50Ω source are shown in Figs. 5-22 and 5-23 respectively. A maximum system efficiency of 0.067% was computed at 956.6MHz. At this frequency, the inductive impedance of the microstrip antenna resonates with the capacitive impedance of the overmoded stacked crystal filter. The low system efficiency is due to the low radiation efficiency of the GaAs

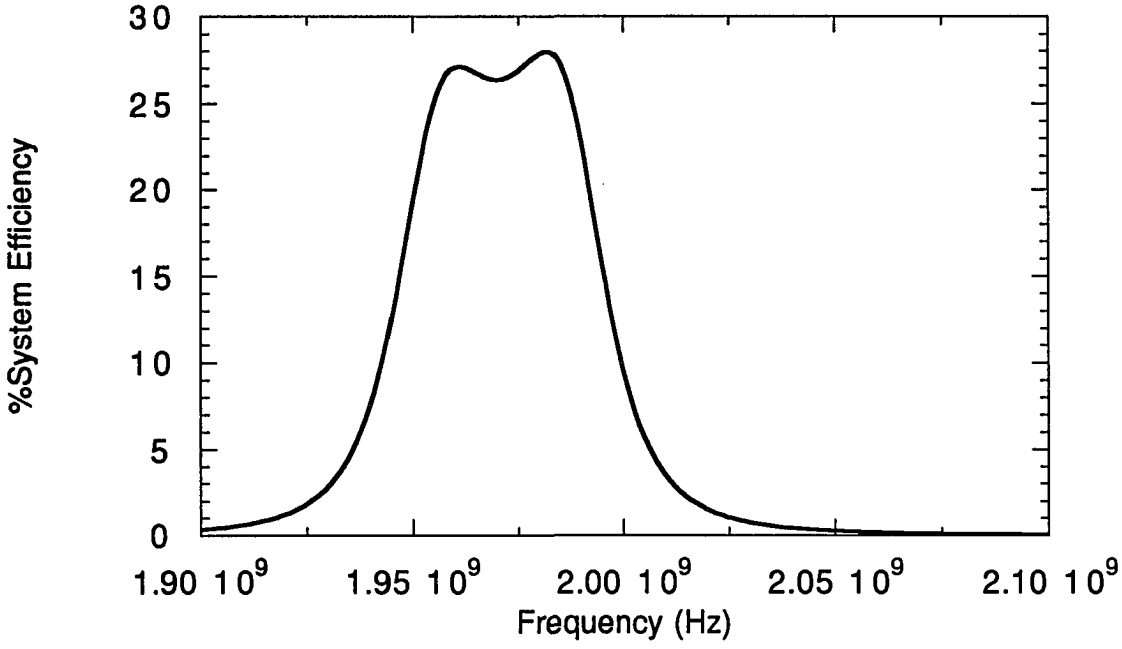

Figure 5-17. System efficiency for the acoustically driven TMF antenna system

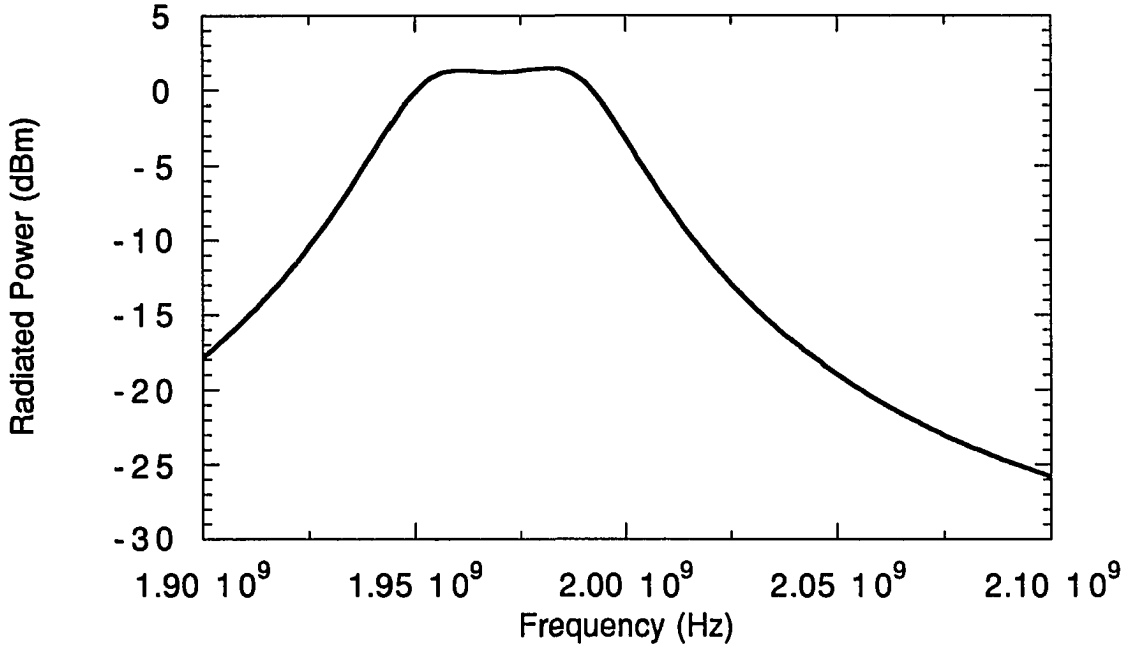

Figure 5-18. Radiated power for the acoustically driven TMF antenna system

microstrip antenna and the high losses in the stacked crystal filter. An integrated microstrip antenna on a gallium arsenide substrate driven by an overmoded AlN stacked crystal filter is therefore not practical.

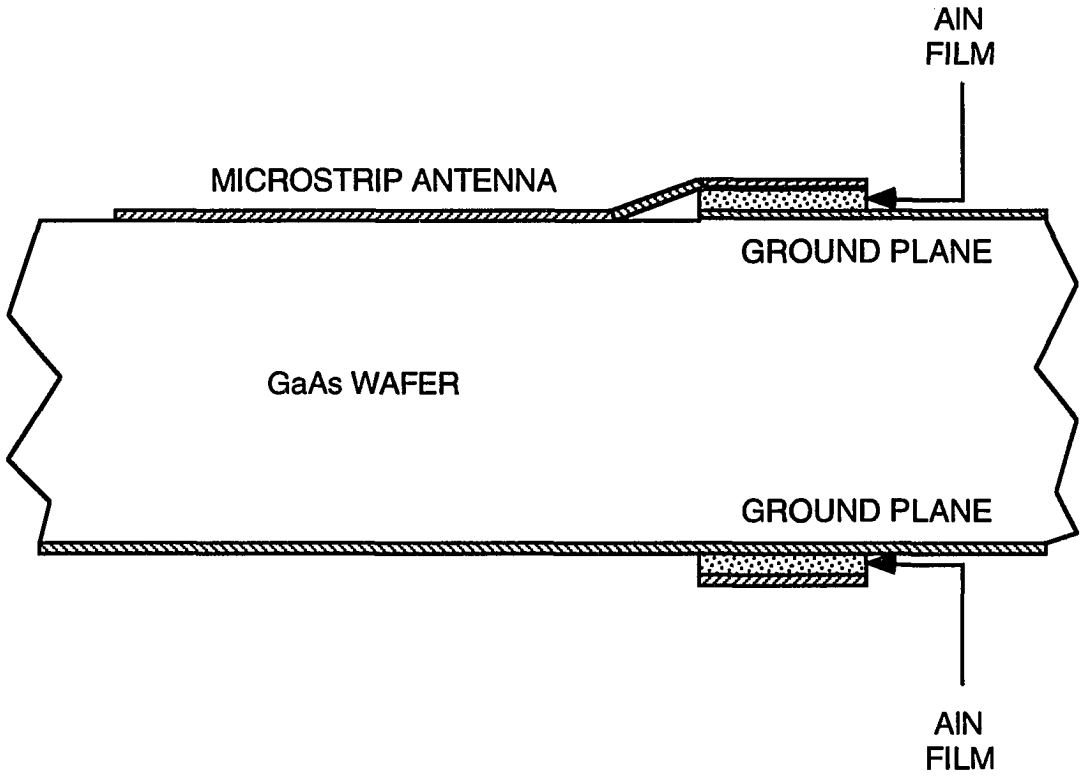

Figure 5-19. Overmoded acoustically driven GaAs integrated antenna

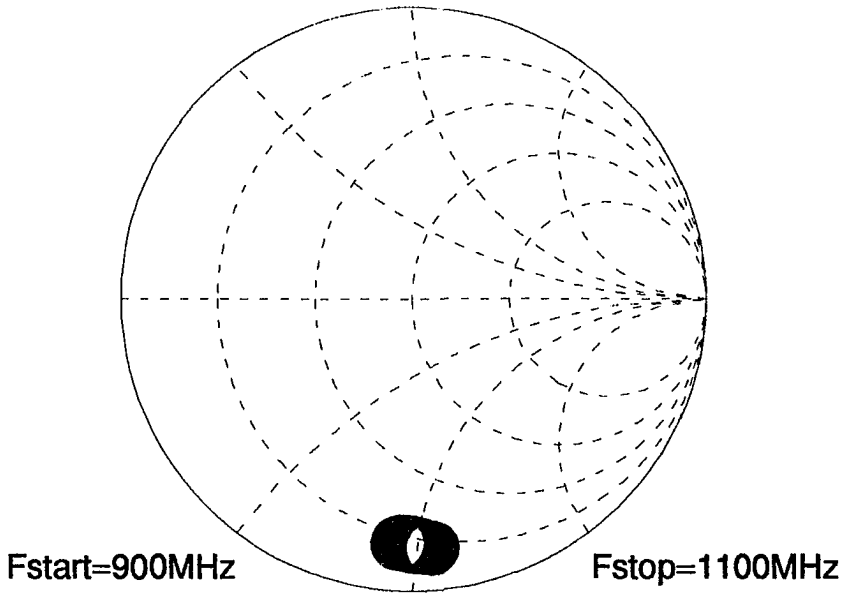

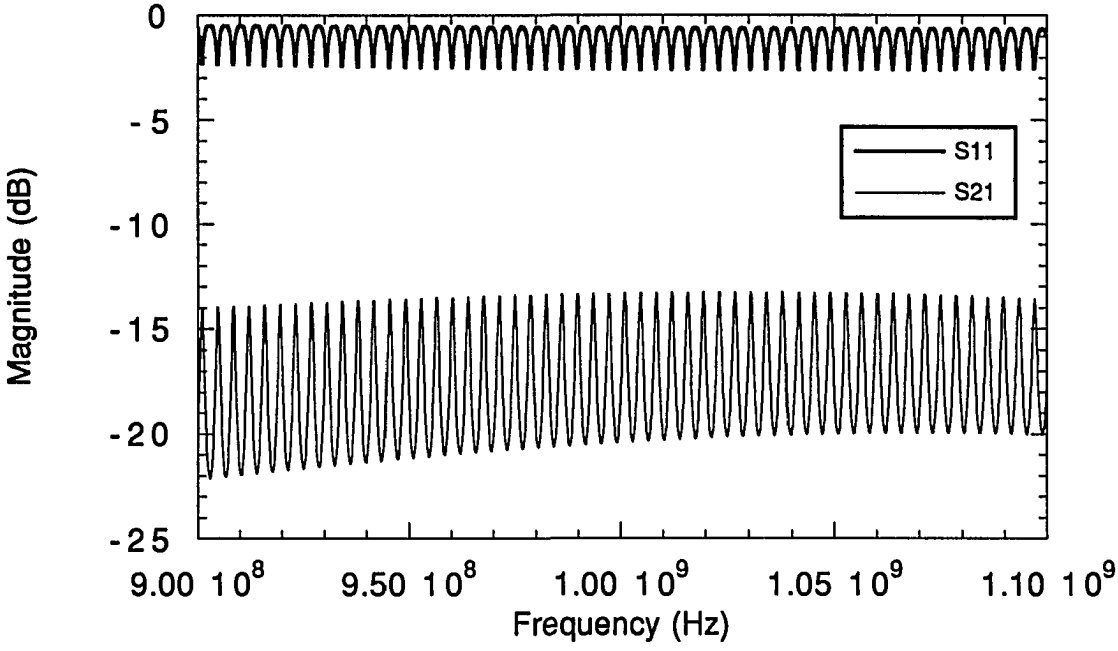

Figure 5-20. Frequency response of the overmoded stacked crystal filter

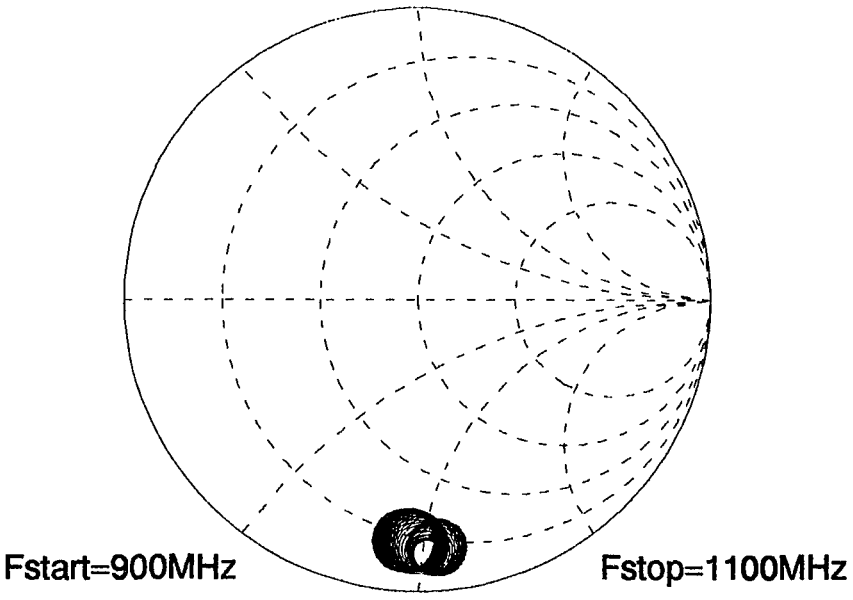

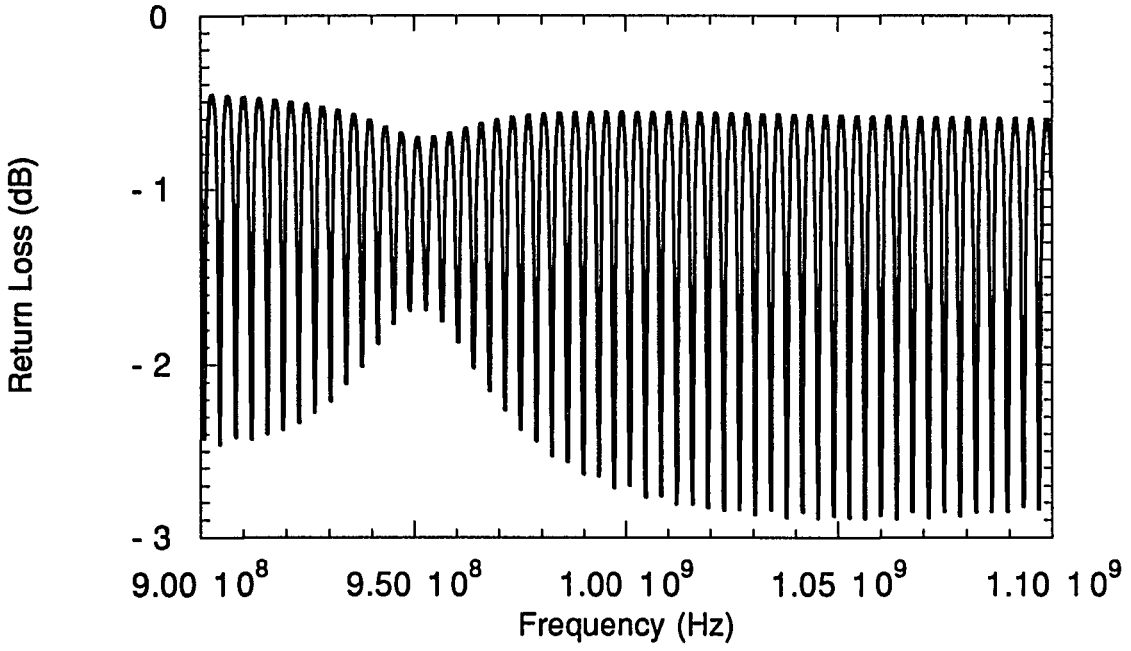

Figure 5-21. Frequency response of the overmoded GaAs antenna system

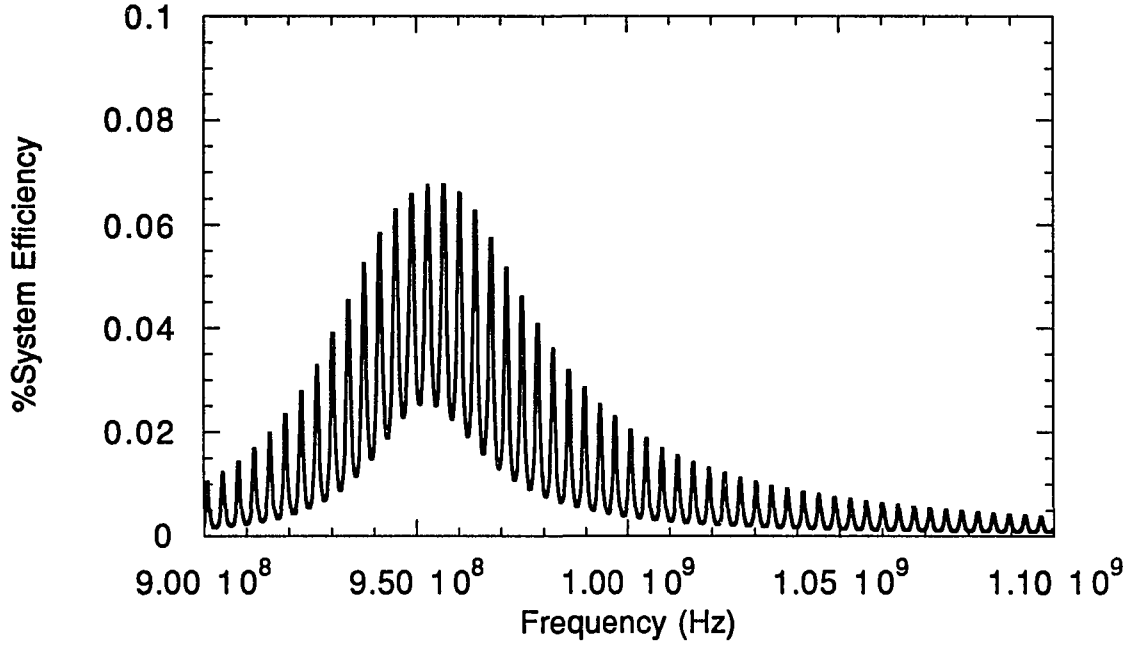

Figure 5-22. System efficiency for the acoustically driven GaAs antenna system

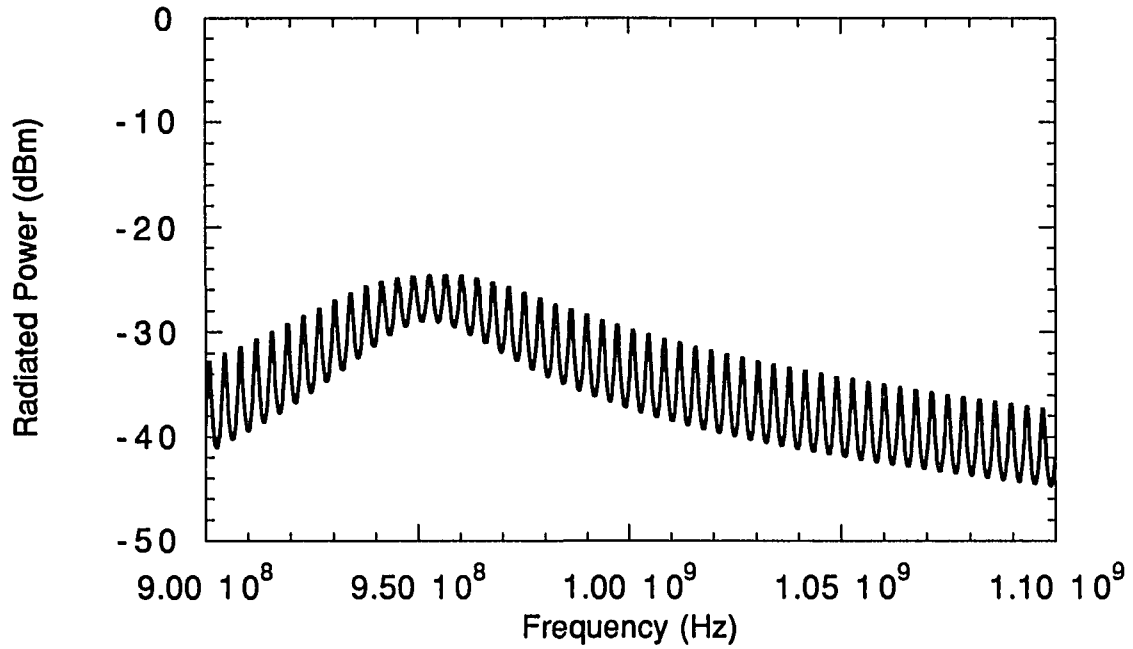

Figure 5-23. Radiated power for the acoustically driven GaAs antenna system

CHAPTER 6. SUMMARY AND RECOMMENDATIONS

The analysis of an acoustically driven integrated microstrip antenna system and the characterization of electromagnetic radiation from bulk acoustic wave devices at resonance has been presented. The antenna system consists of a fundamental mode or overmoded stacked crystal filter driving an integrated microstrip antenna. With this technology, completely integrated receiver systems could be realized where the antenna and electronics are separated by a conducting ground plane. Energy is acoustically coupled from the antenna, through the ground plane, to the electronic circuitry via the piezoelectric effect. On the radiating side of the structure resides a microstrip antenna and a piezoelectric transducer. To study the feasibility of such a system, the performance of microstrip antennas with thin substrates and metalizations was investigated. Like the microstrip antenna, the piezoelectric transducer is a resonant device and its electromagnetic radiation characteristics are also determined.

Assuming the excitation of only one acoustic mode, one dimensional analysis was used to characterize the acoustic devices. For the filter structures, only the terminal characteristics are required for the analysis of the acoustically driven antenna system, and the y-parameter matrices for these devices are derived. In order to characterize the electromagnetic radiation from a bulk wave device, knowledge of the fields within the resonator are required. For a thickness mode resonator, the electric flux density is supplied entirely by the externally applied electric field and therefore the acoustic and electric fields existing within the device are determined with the input current as the independent variable.

The integrated microstrip antennas that were studied are analyzed with the mode matching method and the cavity model. The electric field underneath the conducting patch is computed from the drive current by matching the resonant modes on either side of the feed. The surface equivalence principle is then applied and the microstrip antenna is replaced by equivalent sources. From the equivalent sources, the radiated far fields are determined. The effect of thin metalizations on the antenna characteristics are included by the use of an effective surface resistance. The effective surface resistance was determined by modeling the conductor as a transmission line loaded with an impedance of

377Ω. Microstrip antennas were fabricated in order to experimentally confirm the theoretical results.

It was found from the study that to realize an efficient microstrip antenna, constraints had to be placed on the thickness of the substrate and metalization. For the frequency range of interest, it was determined that a 2μm thick aluminum metalization is sufficient and is realizable with standard integrated circuit processing technology. Using this metalization and a substrate dielectric constant of 1.4, the substrate thickness needs to be 508μm to obtain a 50% radiation efficiency. Unfortunately, It is not possible to deposit a dielectric layer anywhere close to this thickness with standard integrated circuit processing techniques. Another way to increase the radiation efficiency is to use a superconductor instead of aluminum for the metalizations. Using a 100μΩ superconductor and a substrate dielectric constant of 1.4, a 50% radiation efficiency can be achieved with a substrate thickness of 88.9μm. This however is still too thick for standard integrated circuit dielectric film deposition methods. In an attempt to overcome the substrate thickness problem, 635μm thick gallium arsenide wafers were considered as a substrate material. Unfortunately, the use of a high dielectric constant substrate further lowers the radiation efficiency of the antenna. Due to the high dielectric constant of GaAs, it was found that a maximum radiation efficiency of only about 12.5% at 1GHz could be achieved. The key to the realization of an efficient integrated microstrip antenna for operation in the 1GHz to 10GHz frequency range is to identify a low dielectric constant substrate material that can be deposited in a thick layer. A possible candidate for such a substrate material is thermoset microwave foam (TMF). The feasibility of TMF as an integrated microstrip antenna substrate material requires further investigation, however, the theoretical results indicate that 2GHz antennas with near 90% radiation efficiency are realizable on a TMF substrate.

The radiated electromagnetic fields from bulk acoustic wave devices were computed by two different techniques. For the first method, the coupled wave equation is separated into a z-dependent term governed by an acoustic wave equation and an x,y-dependent term governed by the two dimensional Helmholtz equation. The separation is approximately valid under the assumption that only one z-dependent acoustic mode is excited. The solution of the Helmholtz

equation is provided by the mode matching method, and the solution of the z-dependent acoustic wave equation is found from the one dimensional bulk acoustic wave resonator analysis. The total electric field, from which the radiation characteristics may be determined, is the superposition of the x,y and z-dependent terms. For the second method, the resonator is assumed to be electrically small and the electric field is then conservative. This formulation is valid for a multimoded structure as long as the impedance of the resonator is available. This technique is restricted to electrically small devices, however, it is much easier to apply than the mode matching method. The results obtained by the two methods were found to differ by less than 1% for the resonators considered. Both methods predict a null in the radiated electromagnetic power at series resonance and an increase in the radiated power at parallel resonance. This result was experimentally confirmed by measuring the electromagnetic power radiated from quartz and lithium niobate resonators.

Using the results of the stacked crystal filter and microstrip antenna analysis, the performance parameters of the acoustically driven integrated antenna system were determined. The system characteristics of interest are the input impedance, system efficiency, and radiated power. For an antenna on a 508μm thick TMF substrate driven by a fundamental mode aluminum nitride stacked crystal filter, a maximum system efficiency of 27.9% at 2GHz was predicted. The stacked crystal filter also serves as an impedance matching section, increasing the bandwidth of the system. By further increasing the substrate thickness or by using superconducting materials, the system efficiency of the acoustically driven integrated microstrip antenna system could be pushed near 50%.

BIBLIOGRAPHY

1. R. J. Weber, S. G. Burns, C. F. Campbell, and R. O'Toole, "Applications of AlN Thin Film Resonator Topologies as Antennas and Sensors," in *1992 IEEE MTT-S Microwave Symp. Dig.*, pp. 161-164.

2. L. W. Couch, *Digital and Analog Communication Systems.* New York: Macmillan Publishing Co., 1987.

3. A. D. Ballato, "Transmission-Line Analogs for Stacked Piezoelectric Crystal Devices," in *Proc. 1972 IEEE Symp. on Frequency Control*, pp. 86-91.

4. A. D. Ballato, and T. Lukaszek, "A Novel Frequency Selective Device: The Stacked Crystal Filter," in *Proc. 1973 IEEE Symp. on Frequency Control*, pp. 262-269.

5. A. D. Ballato, H. L. Bertoni, and T. Tamir, "Systematic Design of Stacked-Crystal Filters by Microwave Network Methods," *IEEE Trans. Microwave Theory Tech.*, vol. 22, pp. 14-25, Jan. 1974.

6. K. M. Lakin, "Equivalent Circuit Modeling of Stacked Crystal Filters," in *Proc. 1981 IEEE Symp. on Frequency Control*, pp. 257-262.

7. J. F. Rosenbaum, *Bulk Acoustic Wave Theory and Devices.* Boston: Artech House, 1988.

8. B. A. Auld, *Acoustic Fields and Waves in Solids. Vol. I - Vol. II.* Malabar, Florida: Robert E. Krieger Publishing Co., 1990.

9. E. Langer, S. Selberherr, P. A. Markowich, and C. A. Ringhoffer, "Numerical Analysis of Acoustic Wave Generation in Anisotropic Piezoelectric Materials," in *Proc. 1982 IEEE Ultrasonics Symp.*, pp. 350-353.

10. P. Lloyd, and M. Redwood, "Finite-Difference Method for the Investigation of the Vibration of Solids and the Evaluation of the Equivalent-Circuit Characteristics of Piezoelectric Resonators I, II," *Jour. Acoust. Soc. Am.*, vol. 39, pp. 346-361, 1966.

11. K. M. Lakin, "Analysis of Composite Resonator Geometries," in *Proc. 1983 IEEE Symp. on Frequency Control*, pp. 320-324.

12. C. F. Campbell, and R. J. Weber, "Two Dimensional Finite Difference Method for the Analysis of Piezoelectric Devices," in *Proc. 1992 IEEE Ultrasonics Symp.*, pp. 477-481.

13. R. Holland, and E. P. EerNisse, *Design of Resonant Piezoelectric Devices.* Cambridge, Ma: The MIT Press, 1969.

14. R. L. Jungermann, P. Bennet, A. R. Selfridge, B. T. Khuri-Yakub, and G. S. Kino, "Measurement of Normal Surface Displacements for the Characterization of Rectangular Acoustic Array Elements," *Jour. Acoust. Soc. Am.*, vol. 76, pp. 516-524, Aug. 1984.

15. H. Allik, and T. J. R. Huges, "Finite Element Method for Piezoelectric Vibration," *International Journal for Numerical Methods in Engineering*, vol. 2, pp. 151-157, 1970.

16. R. Lerch, "Simulation of Piezoelectric Devices by Two- and Three-Dimensional Finite Elements," *IEEE Trans. Ultrason. Ferroelec. Freq. Contr.*, vol. 37, pp. 233-247, May 1990.

17. R. Lerch, "Finite Element Analysis of Piezoelectric Transducers," in *Proc. 1988 IEEE Ultrasonics Symp.*, pp. 643-654.

18. Y. Kagawa, and T. Yamabuchi, "Finite Element Simulation of Two-Dimensional Electromechanical Resonators," *IEEE Trans. Sonics Ultrason.*, vol. 21, pp. 275-283, Oct. 1974.

19. D. M. Pozar, and D. R. Jackson, class notes from "Short Course on the Analysis and Design of Microstrip Antennas and Arrays," *1992 IEEE APS Int. Symp.*

20. J. R. James, and P. S. Hall, *Handbook of Microstrip Antennas.* London: Peter Perengrinus Ltd., 1989.

21. Y. T. Lo, and S. W. Lee, *Antenna Handbook.* New York: Van Nostrand Reinhold Co., 1988.

22. Y. T. Lo, D. Soloman, and W. F. Richards, "Theory and Experiment on Microstrip Antennas," *IEEE Trans. Antennas Propagat.*, vol. 27, pp. 137-145, Mar. 1979.

23. W. F. Richards, Y. T. Lo, and D. D. Harrison, "An Improved Theory for Microstrip Antennas and Applications," *IEEE Trans. Antennas Propagat.*, vol. 29, pp. 38-46, Jan. 1981.

24. T. Itoh, *Numerical Techniques for Microwave and Millimeter-Wave Passive Structures.* New York: John Wiley & Sons, 1989.

25. T. Okoshi, *Planar Circuits for Microwaves and Lightwaves.* New York: Springer-Verlag, 1985.

26. C. A. Balanis, *Advanced Engineering Electromagnetics.* New York: John Wiley & Sons, 1989.

27. P. C. Y. Lee, "Electromagnetic Radiation from an AT-Cut Quartz Plate Under Lateral Field Excitation," in *Proc. 1988 IEEE Ultrasonics Symp.*, pp. 407-411.

28. P. C. Y. Lee, Y. G. Kim, and J. H. Prevost, "Electromagnetic Radiation from Doubly Rotated Piezoelectric Crystal Plates Vibrating at Thickness Frequencies," in *Proc. 1989 IEEE Ultrasonics Symp.*, pp. 423-428.

29. R. D. Mindlin, "Electromagnetic Radiation from a Vibrating Quartz Plate," *Int. J. Solids Structures*, vol. 9, pp. 697-702, 1972.

30. K. Tsubouchi, and N. Mikoshiba, "Zero Temperature Coefficient Saw Delay Line on AlN Epitaxial Films," in *Proc. 1983 IEEE Ultrasonics Symp.*, pp. 299-310.

31. R. Horton, B. Easter, and A. Gopinath, "Variation of Microstrip Losses with Thickness of Strip," *Electronic Letters*, vol. 7, pp. 490-491, Aug. 1971.

32. Z. Shen, C. Wilker, P. Pang, and W. L. Holstein, "High Tc Superconductor-Sapphire Microwave Resonator with Extremely High Q-Values up to 90k," in *1992 IEEE MTT-S Microwave Symp. Dig.*, pp. 193-196.

ACKNOWLEDGEMENTS

This work was supported by the Department of Electrical Engineering and Computer Engineering, Iowa State University and by a Department of Education fellowship. I would like to thank the Iowa State University Microelectronics Research Center and staff for the use of measurement equipment and fabrication facilities. I would like to express gratitude to my major professor Dr. Robert J. Weber for his guidance throughout the progress of this investigation and for proofreading the final draft of this thesis. I would also like to thank Dr. David T. Stephenson for his guidance concerning the antenna aspects of this work and for serving on my committee. I am also indebted to my other committee members, Dr. Stanley G. Burns, Dr. Rajbir S. Dahiya, Howard Shanks, and Dr. Hsung-Cheng Hsieh. I would also like to thank Dave Schmidt, Al Landin and Dr. Alan Constant for processing the antenna wafers, and Crystal Technology, Inc and P. R. Hoffman Materials Processing Corp. for supplying the lithium niobate and quartz wafers. A very special thanks goes to my parents William and Holly Campbell, and to my wife Angie for boundless support, encouragement and patience.

APPENDIX A: 2D FINITE DIFFERENCE PAPER

TWO DIMENSIONAL FINITE DIFFERENCE METHOD FOR THE ANALYSIS OF PIEZOELECTRIC DEVICES*

C. F. CAMPBELL and R. J. WEBER

Department of Electrical Engineering and Computer Engineering
Iowa State University, Ames, Iowa 50011

ABSTRACT

A general finite difference technique is described for the AC steady state analysis of two dimensional piezoelectric devices. The method is formulated to accommodate anisotropic and inhomogeneous material as well as variable mesh spacings such that irregular boundaries may be modeled. The method is then applied to bulk acoustic wave resonator and stacked crystal filter structures. For the resonator analysis, the results are compared with published data.

INTRODUCTION

In this paper the well known finite difference method is applied for the AC steady state analysis of two dimensional piezoelectric devices. This technique has been used by Lloyd and Redwood to study contour mode vibrations in thin rectangular plates, Langer et al for the transient analysis of SAW devices, and Lakin for composite bulk acoustic wave resonator analysis [1,2,3]. The purpose of this work is to generalize the finite difference techniques that appear in the literature and to compare the results with published data.

THEORY

Assuming linear material and steady state sinusoidal time dependence; the quasi-static equations for the modeling of piezoelectric devices are Newton's law, Gauss's law and the constitutive relations respectively as given below [4]:

$$\frac{\partial T_{ij}}{\partial x_i} = -\rho\omega^2 u_j \tag{1}$$

$$\frac{\partial D_i}{\partial x_i} = 0 \tag{2}$$

$$T_{ij} = c_{ijkl}\frac{\partial u_k}{\partial x_l} + e_{kij}\frac{\partial \phi}{\partial x_k} \tag{3}$$

$$D_i = e_{ikl}\frac{\partial u_k}{\partial x_l} - \varepsilon_{ik}\frac{\partial \phi}{\partial x_k} \tag{4}$$

In a two dimensional problem, no variation is permitted in the x_3 direction, and from (1,2,3,4) the following set of coupled partial differential equations may be derived where k=1,2,3 is summed for each j=1,2,3.

$$c_{1jk1}\frac{\partial^2 u_k}{\partial x_1^2} + (c_{1jk2}+c_{2jk1})\frac{\partial^2 u_k}{\partial x_1 \partial x_2} + c_{2jk2}\frac{\partial^2 u_k}{\partial x_2^2} + e_{11j}\frac{\partial^2 \phi}{\partial x_1^2} + (e_{21j}+e_{12j})\frac{\partial^2 \phi}{\partial x_1 \partial x_2} + e_{22j}\frac{\partial^2 \phi}{\partial x_2^2} = -\rho\omega^2 u_j \tag{5}$$

$$e_{1k1}\frac{\partial^2 u_k}{\partial x_1^2} + (e_{1k2}+e_{2k1})\frac{\partial^2 u_k}{\partial x_1 \partial x_2} + e_{2k2}\frac{\partial^2 u_k}{\partial x_2^2} - \varepsilon_{11}\frac{\partial^2 \phi}{\partial x_1^2} - (\varepsilon_{12}+\varepsilon_{21})\frac{\partial^2 \phi}{\partial x_1 \partial x_2} - \varepsilon_{22}\frac{\partial^2 \phi}{\partial x_2^2} = 0 \tag{6}$$

After [2,3], equations (5,6) are written in a more general form by letting k=1,2,3,4 and j=1,2,3,4 where $u_4 = \phi$.

$$A_{jk}\frac{\partial^2 u_k}{\partial x_1^2} + (B_{jk}+C_{jk})\frac{\partial^2 u_k}{\partial x_1 \partial x_2} + D_{jk}\frac{\partial^2 u_k}{\partial x_2^2} = \lambda_j u_j \tag{7}$$

$$\lambda_j = \begin{cases} -\rho\omega^2 & j = 1,2,3 \\ 0 & j = 4 \end{cases}$$

A_{jk}, B_{jk}, C_{jk}, D_{jk} written in contracted notation are,

A_{jk}	k=1	k=2	k=3	k=4
j=1	c_{11}	c_{16}	c_{15}	e_{11}
j=2	c_{16}	c_{66}	c_{56}	e_{16}
j=3	c_{15}	c_{56}	c_{55}	e_{15}
j=4	e_{11}	e_{16}	e_{15}	$-\varepsilon_{11}$

B_{jk}	k=1	k=2	k=3	k=4
j=1	c_{16}	c_{12}	c_{14}	e_{21}
j=2	c_{66}	c_{26}	c_{46}	e_{26}
j=3	c_{56}	c_{25}	c_{45}	e_{25}
j=4	e_{16}	e_{12}	e_{14}	$-\varepsilon_{12}$

C_{jk}	k=1	k=2	k=3	k=4
j=1	c_{16}	c_{66}	c_{56}	e_{16}
j=2	c_{12}	c_{26}	c_{25}	e_{12}
j=3	c_{14}	c_{46}	c_{45}	e_{14}
j=4	e_{21}	e_{26}	e_{25}	$-\varepsilon_{21}$

D_{jk}	k=1	k=2	k=3	k=4
j=1	c_{66}	c_{26}	c_{46}	e_{26}
j=2	c_{26}	c_{22}	c_{24}	e_{22}
j=3	c_{46}	c_{24}	c_{44}	e_{24}
j=4	e_{26}	e_{22}	e_{24}	$-\varepsilon_{22}$

1051-0117/92/0000-0477 $1.00 © 1992 IEEE

Defining $Q_{ij} = T_{ij}$ for j = 1,2,3 and $Q_{ij} = D_i$ for j = 4, the constitutive relations in general form become,

$$Q_{1j} = \mathbf{A}_{jk}\frac{\partial u_k}{\partial x_1} + \mathbf{B}_{jk}\frac{\partial u_k}{\partial x_2} \tag{8}$$

$$Q_{2j} = \mathbf{C}_{jk}\frac{\partial u_k}{\partial x_1} + \mathbf{D}_{jk}\frac{\partial u_k}{\partial x_2} \tag{9}$$

FINITE DIFFERENCE APPROXIMATION

The region of interest is discretized by a finite difference mesh of cells consisting of nine mesh points as shown in figure 1. The four quadrants may be of different materials and mesh spacings.

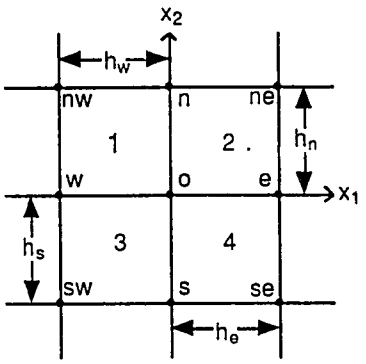

Figure 1

The partial derivatives are replaced with the following finite difference approximations [5],

$$\frac{\partial^2 f}{\partial x_1 \partial x_2} = \frac{f_n - f_o}{\beta_{nn}} + \frac{f_s - f_o}{\beta_{ss}} + \frac{f_e - f_o}{\beta_{ee}} + \frac{f_w - f_o}{\beta_{ww}}$$

$$+ \frac{f_{sw} - f_o}{\beta_{sw}} + \frac{f_{se} - f_o}{\beta_{se}} + \frac{f_{ne} - f_o}{\beta_{ne}} + \frac{f_{nw} - f_o}{\beta_{nw}} + O(h^2) \tag{10}$$

$$\frac{\partial^2 f}{\partial x_1^2} = \frac{f_e - f_o}{\beta_e} + \frac{f_w - f_o}{\beta_w} + O(h^2) \tag{11}$$

$$\frac{\partial^2 f}{\partial x_2^2} = \frac{f_n - f_o}{\beta_n} + \frac{f_s - f_o}{\beta_s} + O(h^2) \tag{12}$$

$$\frac{\partial f}{\partial x_1} = \frac{f_e - f_o}{\alpha_e} + \frac{f_w - f_o}{\alpha_w} + O(h^2) \tag{13}$$

$$\frac{\partial f}{\partial x_2} = \frac{f_n - f_o}{\alpha_n} + \frac{f_s - f_o}{\alpha_s} + O(h^2) \tag{14}$$

$$\beta_{nn} = \frac{h_e h_w h_n (h_n + h_s)}{h_s (h_e - h_w)} \qquad \beta_{ss} = \frac{h_e h_w h_s (h_n + h_s)}{h_n (h_w - h_e)}$$

$$\beta_{ee} = \frac{h_e h_s h_n (h_e + h_w)}{h_w (h_n - h_s)} \qquad \beta_{ww} = \frac{h_n h_w h_s (h_e + h_w)}{h_e (h_s - h_n)}$$

$$\beta_{se} = \frac{-(h_e + h_w)(h_n + h_s)}{h_w h_n / h_s h_e} \qquad \beta_{sw} = \frac{(h_e + h_w)(h_n + h_s)}{h_e h_n / h_s h_w}$$

$$\beta_{nw} = \frac{-(h_e + h_w)(h_n + h_s)}{h_e h_s / h_n h_w} \qquad \beta_{ne} = \frac{(h_e + h_w)(h_n + h_s)}{h_w h_s / h_n h_e}$$

$$\beta_e = h_e(h_e + h_w)/2 \qquad \beta_w = h_w(h_w + h_e)/2$$

$$\beta_n = h_n(h_n + h_s)/2 \qquad \beta_s = h_s(h_s + h_n)/2$$

$$\alpha_e = \frac{h_e (h_e + h_w)}{h_w} \qquad \alpha_w = \frac{-h_w (h_e + h_w)}{h_e}$$

$$\alpha_n = \frac{h_n (h_n + h_s)}{h_s} \qquad \alpha_s = \frac{-h_s (h_n + h_s)}{h_n}$$

Substituting these into (7), the following set of four difference equations result corresponding to j=1,2,3,4:

$$\frac{u_k^e}{Z_{jk}^e} + \frac{u_k^w}{Z_{jk}^w} + \frac{u_k^n}{Z_{jk}^n} + \frac{u_k^s}{Z_{jk}^s} + \frac{u_k^{sw}}{Z_{jk}^{sw}} + \frac{u_k^{se}}{Z_{jk}^{se}} + \frac{u_k^{nw}}{Z_{jk}^{nw}} + \frac{u_k^{ne}}{Z_{jk}^{ne}} + \frac{u_k^o}{Z_{jk}^o} = 0 \tag{15}$$

The finite difference impedances are defined as,

$$\frac{1}{Z_{jk}^e} = \frac{\mathbf{A}_{jk}}{\beta_e} + \frac{\mathbf{B}_{jk} + \mathbf{C}_{jk}}{\beta_{ee}} \qquad \frac{1}{Z_{jk}^{se}} = \frac{\mathbf{B}_{jk} + \mathbf{C}_{jk}}{\beta_{se}}$$

$$\frac{1}{Z_{jk}^w} = \frac{\mathbf{A}_{jk}}{\beta_w} + \frac{\mathbf{B}_{jk} + \mathbf{C}_{jk}}{\beta_{ww}} \qquad \frac{1}{Z_{jk}^{sw}} = \frac{\mathbf{B}_{jk} + \mathbf{C}_{jk}}{\beta_{sw}}$$

$$\frac{1}{Z_{jk}^n} = \frac{\mathbf{D}_{jk}}{\beta_n} + \frac{\mathbf{B}_{jk} + \mathbf{C}_{jk}}{\beta_{nn}} \qquad \frac{1}{Z_{jk}^{nw}} = \frac{\mathbf{B}_{jk} + \mathbf{C}_{jk}}{\beta_{nw}}$$

$$\frac{1}{Z_{jk}^s} = \frac{\mathbf{D}_{jk}}{\beta_s} + \frac{\mathbf{B}_{jk} + \mathbf{C}_{jk}}{\beta_{ss}} \qquad \frac{1}{Z_{jk}^{ne}} = \frac{\mathbf{B}_{jk} + \mathbf{C}_{jk}}{\beta_{ne}}$$

$$\frac{1}{Z_{jk}^o} = -\left[\frac{1}{Z_{jk}^e} + \frac{1}{Z_{jk}^w} + \frac{1}{Z_{jk}^n} + \frac{1}{Z_{jk}^s} + \frac{1}{Z_{jk}^{sw}} + \frac{1}{Z_{jk}^{se}} + \frac{1}{Z_{jk}^{nw}} + \frac{1}{Z_{jk}^{ne}} + \lambda_j \delta_{jk}\right]$$

where δ_{jk} is the Kronecker delta function. The finite difference approximations for the constitutive relations are obtained from (8,9). For the x_1 direction,

$$Q_{1j} = \frac{u_k^e}{Z_{jk}^e} + \frac{u_k^w}{Z_{jk}^w} + \frac{u_k^n}{Z_{jk}^n} + \frac{u_k^s}{Z_{jk}^s} + \frac{u_k^o}{Z_{jk}^o} \tag{16}$$

with finite difference impedances,

$$\frac{1}{Z^e_{jk}} = \frac{A_{jk}}{\alpha_e} \qquad \frac{1}{Z^w_{jk}} = \frac{A_{jk}}{\alpha_w} \qquad \frac{1}{Z^n_{jk}} = \frac{B_{jk}}{\alpha_n} \qquad \frac{1}{Z^s_{jk}} = \frac{B_{jk}}{\alpha_s}$$

$$\frac{1}{Z^o_{jk}} = -\left[\frac{1}{Z^e_{jk}} + \frac{1}{Z^w_{jk}} + \frac{1}{Z^n_{jk}} + \frac{1}{Z^s_{jk}}\right]$$

and the x_2 direction,

$$Q_{2j} = \frac{u^e_k}{Z^e_{jk}} + \frac{u^w_k}{Z^w_{jk}} + \frac{u^n_k}{Z^n_{jk}} + \frac{u^s_k}{Z^s_{jk}} + \frac{u^o_k}{Z^o_{jk}} \qquad (17)$$

with finite difference impedances

$$\frac{1}{Z^e_{jk}} = \frac{C_{jk}}{\alpha_e} \qquad \frac{1}{Z^w_{jk}} = \frac{C_{jk}}{\alpha_w} \qquad \frac{1}{Z^n_{jk}} = \frac{D_{jk}}{\alpha_n} \qquad \frac{1}{Z^s_{jk}} = \frac{D_{jk}}{\alpha_s}$$

$$\frac{1}{Z^o_{jk}} = -\left[\frac{1}{Z^e_{jk}} + \frac{1}{Z^w_{jk}} + \frac{1}{Z^n_{jk}} + \frac{1}{Z^s_{jk}}\right]$$

To illustrate how the finite difference equations are applied, consider the following resonator geometry. A two dimensional device of rectangular cross section, surrounded by air, with a potential difference applied between the top and bottom surface via massless conductors. Since the air provides no restoring force, traction free boundary conditions need to be applied on the top, bottom and sides of the resonator. Also, assume that the dielectric constant of the material is large compared to unity, and that the no fringing electric field condition must be enforced on the sides. These conditions are represented mathematically by,

$$n_i Q_{ij} = 0$$

The upper left hand corner of such a device is shown in figure 2 by the thick dashed lines. Since the fields do not vary in the x_3 direction, assume $u_3 = 0$.

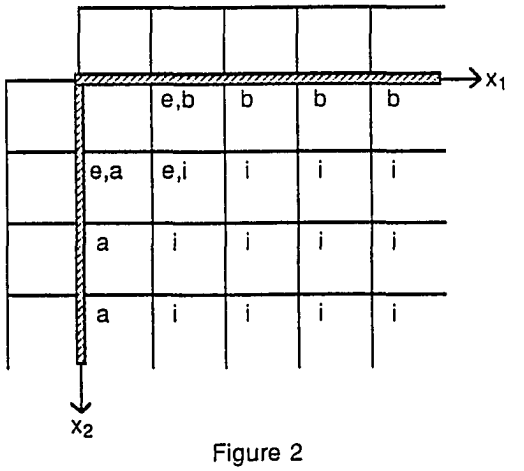

Figure 2

After [1], the material is assumed to extend one node beyond the device. At the nodes labeled "i", (15) is applied for j=1,2,4 and k=1,2,4. For the nodes labeled "a" both (15) and (16) are applied for j=1,2,4 and k=1,2,4. However, at the nodes labeled "b" (15) and (17) are applied for j=1,2 and k=1,2 only, because the potential is known along this surface. At the corners the normal vector is discontinuous, and the traction free boundary conditions are indeterminate [1]. Instead of applying the difference equations at these nodes, the displacements may extrapolated from the surrounding nodes with an extrapolation equation. As suggested by Lloyd and Redwood, the following extrapolation equation was used at the nodes labeled "e" for k=1 and k=2, to include the corner nodes in the matrix equation.

$$u^o_k - \frac{1}{2}\left[u^n_k + u^s_k + u^e_k + u^w_k\right] + \frac{1}{4}\left[u^{ne}_k + u^{sw}_k + u^{se}_k + u^{nw}_k\right] = 0 \qquad (18)$$

This is a finite difference approximation to,

$$\frac{\partial^2 u_k(o)}{\partial x_1^2} = \frac{1}{2}\frac{\partial^2 u_k(n)}{\partial x_1^2} + \frac{1}{2}\frac{\partial^2 u_k(s)}{\partial x_1^2}$$

and forces the continuity of the second derivatives. Following the procedure outlined above for the entire mesh, one obtains a sparse matrix equation, the solution of which is an approximation for the fields within the device. Once these fields are known, the parameters of interest (impedance, resonant frequency, etc.) may be computed by various methods [1,4].

RESULTS

In order to test the validity of the method, device geometries were analyzed where results exist in the literature for comparison. In the first example, a two dimensional PZT-5H resonator of rectangular cross section was analyzed with variational techniques by Jungermann et al [6]. This device was then analyzed by the finite difference method for comparison of the calculated resonant frequencies.

Frequency (MHz)	f_{s1}	f_{p1}	f_{s2}	f_{p2}
Measured [6]	0.91	1.22	2.45	2.51
Theoretical [6]	0.99	1.29	2.47	2.49
Finite Difference	0.94	1.26	2.46	2.49

As a second example, in a finite element study by Lerch [7] various two dimensional transducers of rectangular cross section were analyzed. These devices were made of a PZT like material called Siemens-Vibrit-420 and in each case are 2mm thick. Shown in figures 3-5 are plots of the results to compare the finite element and finite difference analysis. The format follows that of Lerch [7].

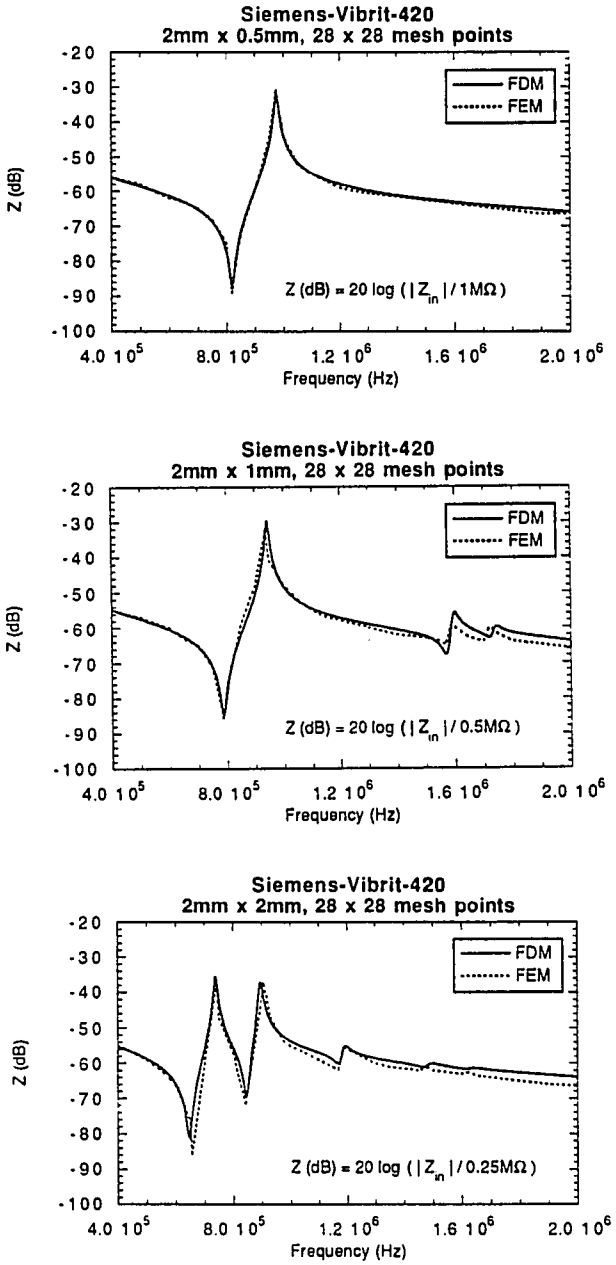

Figures 3-5

In both the examples, the agreement with the finite difference method is good. The high frequency disagreement with the finite element method is most likely due to the courseness of the finite difference mesh that was used for the calculation. Also, the data given in [7] for Siemens-Vibrit-420 was for lossless material, and in this work an imaginary portion was added to obtain approximate agreement with the coupling strengths observed by Lerch. Some of the disagreement may be due to uncertainty in the estimate for the imaginary parts of the material constants.

In a composite resonator structure, a layer of nonpiezoelectric material is acoustically coupled to the device [3]. To handle this material inhomogeneity one may take advantage of the analogy between the finite difference equations (15,16,17) and node voltage equations from electrical network theory [8]. In order to preserve the continuity of the fields across the material interface, the finite difference impedances are combined in parallel as shown figure 6.

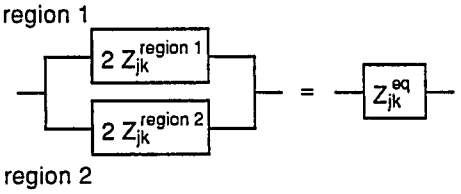

Figure 6

For example, the transducer from figure 4 was analyzed again except that the device now consists of a 1.5mm thick layer of Vibrit-420 and 0.5mm thick layer of silicon. The results of the finite difference simulation are shown in figure 7. Note that the resonant frequencies of two of the modes increase which is consistent with the larger acoustic velocity of silicon and suggests that these are thickness modes. One of the modes however remains virtually unchanged which would suggest that it is probably a lateral mode.

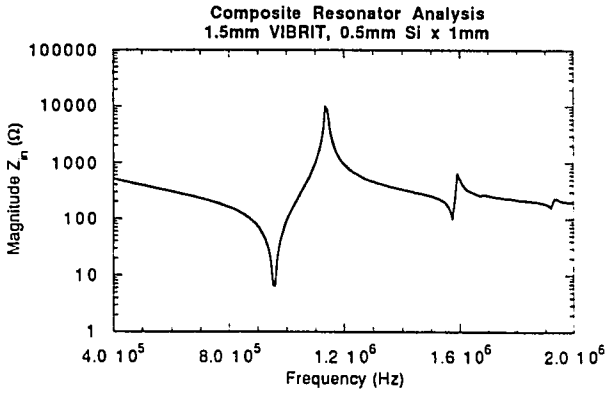

Figure 7

Two port piezoelectric devices may also be analyzed with the finite difference method. The y-parameters of a two port device are computed by grounding one of the ports and applying a potential of unity magnitude to the other port. This defines boundary conditions for the electric potential function, and y_{11} and y_{21} will be equal to currents i_1 and i_2 respectively directed into the device. The port currents are found by numerically evaluating,

$$i = j\omega \int_A \vec{D} \cdot d\vec{S} \qquad (19)$$

where the integral is over the conducting surface, and the electric flux density is found with the finite difference method. To find y_{12} and y_{22} the procedure is repeated with the other port grounded. For example, consider the stacked crystal filter shown in figure 8.

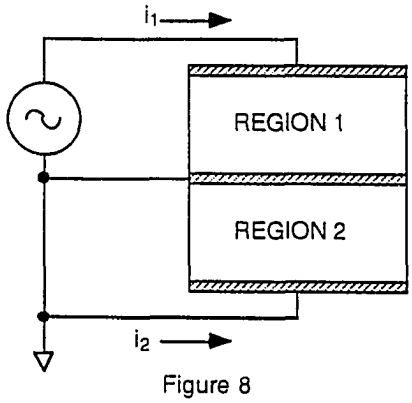

Figure 8

To determine the frequency response of the filter, one of the ports is grounded, and a unit potential is imposed on the top conductor and zero potential on the grounded conductors. The fields within the device are then determined with the finite difference method. From these fields, currents i_1 and i_2 are computed from which the y-parameters of the two port are easily found. Shown in figure 9 is the result of the analysis of a tall, thin two dimensional aluminum nitride stacked crystal filter. Note the spurious responses due to the finite width dimensions.

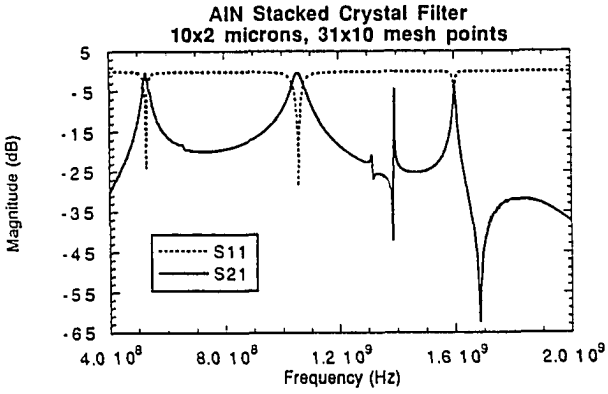

Figure 9

CONCLUSIONS

A finite difference method for the AC steady state analysis of two dimensional piezoelectric devices has been presented. Transducers of rectangular cross section were analyzed and good agreement with results from the literature were obtained. The electrical network analogy with the finite difference equations was applied to analyze composite resonator structures. Finally, the finite difference analysis of two port devices was discussed, and the method was applied to a stacked crystal filter topology.

REFERENCES

1. Lloyd, P. and Redwood, M. "Finite-Difference Method for the Investigation of the Vibration of Solids and the Evaluation of the Equivalent-Circuit Characteristics of Piezoelectric Resonators I, II." Jour. Acoust. Soc. Am., 39, 2 (1966), 346-361.

2. Langer, E., Selberherr, S., Markowich, P. A. and Ringhoffer, C. A. "Numerical Analysis of Acoustic Wave Generation in Anisotropic Piezoelectric Materials." IEEE 1982 Ultrasonics Symposium, 350-353.

3. Lakin, F.M. "Analysis of Composite Resonator Geometries." Proceedings of the 37th Annual Symposium of Frequency Control, 1983, 320-324.

4. IEEE Std. 176-1978, IEEE Standard On Piezoelectricity.

5. Hall, C.A., and Porsching, T.A. Numerical Analysis of Partial Differential Equations. Englewood Cliffs, New Jersey : Printice Hall, Inc., 1990.

6. Jungermann, R. L., Bennet, P., Selfridge, A. R., Khuri-Yakub, B. T. and Kino, G. S. "Measurement of Normal Surface Displacements for the Characterization of Rectangular Acoustic Array Elements." Jour. Acoust. Soc. Am., 76 (August, 1984), 516-524.

7. Lerch, R. "Simulation of Piezoelectric Devices by Two-and Three-Dimensional Finite Elements." IEEE Transactions On Ultrasonics Vol. 37, No 2. (May, 1990), 233-247.

8. Hoole, S.R. Computer-Aided Analysis and Design of Electromagnetic Devices.New York : Elsevier, 1989.

* This work was supported by a U. S. Dept. of Commerce grant through the Center for Advanced Technology Development, and the Department of Electrical Engineering and Computer Engineering, Iowa State University. The graduate student was supported by a U. S. Dept. of Education Fellowship.

APPENDIX B: EM RADIATION FROM BAW DEVICES PAPER

CALCULATION OF RADIATED ELECTROMAGNETIC POWER FROM BULK ACOUSTIC WAVE RESONATORS

C. F. CAMPBELL and R. J. WEBER

Department of Electrical Engineering and Computer Engineering
Iowa State University, Ames, Iowa 50011

ABSTRACT

In this paper, a general technique for calculating the radiated electromagnetic fields from an electrically small bulk acoustic wave resonator in the vicinity of acoustic resonance is presented. The BAW resonator is analyzed as an electrically small microstrip antenna on a piezoelectric substrate. By the application of the surface equivalence principle, the device is replaced by equivalent sources. The radiated far fields found from the equivalent sources are integrated over the upper half plane to determine the total amount of radiated EM power as a function of frequency. The result is general enough to characterize the electromagnetic radiation from arbitrarily shaped metalizations, and the antenna pattern and polarization of the radiation may also be determined. The theoretical results are experimentally confirmed by measuring the radiated EM power spectrum from lithium niobate and quartz resonators.

INTRODUCTION

With the use of piezoelectric films, the operating frequency of bulk acoustic wave resonators has been extended into the microwave frequency range [1]. As the resonant frequency of these devices continues to increase, spurious electromagnetic radiation will become more of a problem. Some prior work of note has been done on radiation from piezoelectric crystals. Mindlin and Lee have computed the radiated power from bare rotated quartz plates at thickness mode frequencies [2,3,4]. The work being proposed here differs from the prior work of Mindlin and Lee in that a bulk acoustic wave device is analyzed as a microstrip antenna with a piezoelectric substrate.

THEORY

Shown in Figure 1 is a rectangular bulk acoustic wave resonator where the piezoelectric layer and ground plane are assumed to extend to infinity. Due to the large difference between the electromagnetic and acoustic wavelengths in the piezoelectric substrate material, useful bulk acoustic wave resonators are almost always electrically small devices. The BAW resonator may be considered electrically small if the perimeter is less than 0.3 times the EM wavelength in the substrate material [5]. In an electrically small device, the conductors are considered equipotential surfaces

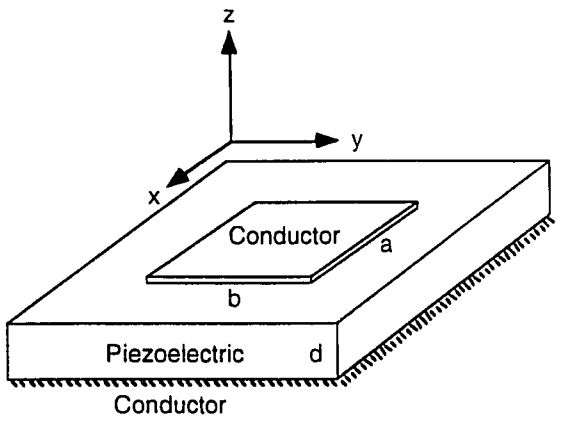

Figure 1

and the electric field is conservative. This is consistent with the quasi-static approximation for piezoelectric devices where the electric field is assumed to be irrotational and is related to the potential function by [6]

$$\mathbf{E} = -\nabla\phi \tag{1}$$

In order to estimate the radiated electromagnetic power from the device shown in Figure 1, the radiated fields must be found. One way to compute the radiated far fields is to apply the surface equivalence principle to the structure. The idea behind the surface equivalence principle is to surround the source by a closed surface S, and place equivalent sources on the closed surface. The equivalent sources will produce the same far fields outside of the closed surface as did the original source, but produce null fields inside the surface. The equivalent sources are electric and magnetic surface currents given by the following [7]:

$$\mathbf{M_s} = \mathbf{E} \times \hat{n} \tag{2}$$

$$\mathbf{J_s} = \hat{n} \times \mathbf{H} \tag{3}$$

The fields **E** and **H** are the actual electric and magnetic source fields that exist within the resonator. Since the electric field is assumed to be irrotational, the magnetic field of the device is equal to zero and only Eq. (2) needs to be considered. Summarized in Figure 2 is the

ACCEPTED: 1993 IEEE SYMPOSIUM ON FREQUENCY CONTROL

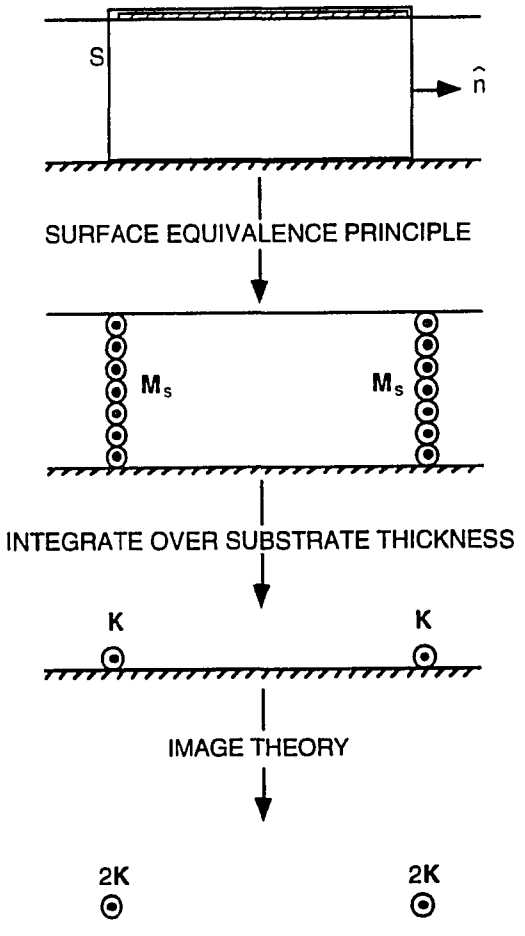

Figure 2

evolution of the electromagnetic radiation model for the BAW resonator.

First, the surface equivalence principle is applied by surrounding the structure with a closed surface S. If the conductors can be assumed to be perfect, the tangential electric field at the conductor surfaces must be zero and the magnetic surface current placed on the top and bottom of the closed surface S is also zero. The magnetic surface currents on the sides of the surface S are not zero and are the main source of the radiated fields as shown in the second part of Figure 2. Note, that in the radiation model, a ribbon of magnetic current density placed at the periphery of the device. Since the thickness of the substrate is on the order of an acoustic wavelength, it is electrically very thin, and the effect of the substrate on the radiated far fields is negligible [8]. The magnetic current density can then be integrated over the substrate thickness and condensed into a filamentary magnetic current loop **K** over an infinite ground plane as shown in the third illustration of Figure 2. The ground plane can then be removed with image theory, and the radiation model valid for the upper half plane is shown in the last part of Figure 2.

From Eq. (2), the magnetic current at the sides of closed surface S for an arbitrary electric field is equal to

$$\mathbf{K} = \hat{x}\,K_x + \hat{y}\,K_y = \int_0^d \mathbf{M}_s\,dz = \int_0^d \mathbf{E} \times \hat{n}\,dz$$

$$= (\hat{z} \times \hat{n}) \int_0^d E_z\,dz = -V(\hat{z} \times \hat{n}) \qquad (4)$$

The radiation model for the BAW resonator, valid for the upper half plane, reduces to a loop of magnetic current placed at the periphery of the device as in Figure 3.

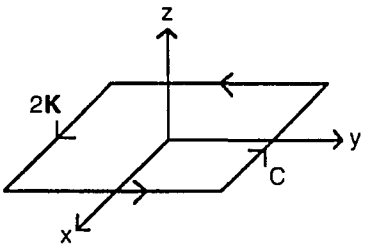

Figure 3

From Eq. (4), the magnitude of the magnetic current is equal to the voltage applied to the resonator. Since the conductors are assumed to be equipotential surfaces and the electric field conservative, this result is also valid for a three dimensional bulk acoustic wave resonator. A three dimensional device is a multiple mode structure and its electric field will be some complicated function of x,y and z. However, since the electric field is conservative, the line integral from one conductor to the other over any arbitrary path is equal to the voltage applied to the device. Assuming that the device is driven by a voltage source V_s with source impedance Z_o, from elementary circuit analysis the voltage across the device is equal to

$$V = V_s \frac{Z_{in}}{Z_{in} + Z_o} \qquad (5)$$

where Z_{in} is the impedance of the resonator.

The magnetic current in the radiation model can be computed with Eq. (4) once the input impedance of the device is known. Thus, if the impedance of the resonator is available via the Mason model, finite element computation, or measurement, Eq. (4) is valid as long as the device can be considered electrically small. The radiated far fields from an arbitrary loop of magnetic current impressed on the ground plane are [7]

$$E_\theta(r,\theta,\varphi) = \frac{j\omega\mu_o e^{-jk_o r}}{2\pi\eta_o r}\left[\tilde{K}_x(u,v)\sin\varphi - \tilde{K}_y(u,v)\cos\varphi\right] \qquad (6)$$

$$E_\varphi(r,\theta,\varphi) = \frac{j\omega\mu_o e^{-jk_o r}}{2\pi\eta_o r}\cos\theta\left[\tilde{K}_x(u,v)\cos\varphi + \tilde{K}_y(u,v)\sin\varphi\right] \qquad (7)$$

The Fourier transforms of the source are defined as

$$\tilde{K}_x(u,v) = \int_C K_x\, e^{j(ux+vy)}\, \hat{x} \cdot dl \qquad (8)$$

$$\tilde{K}_y(u,v) = \int_C K_y\, e^{j(ux+vy)}\, \hat{y} \cdot dl \qquad (9)$$

where

$$u = k_o \sin\theta \cos\varphi \qquad v = k_o \sin\theta \sin\varphi$$

$$k_o = \omega\sqrt{\varepsilon_o \mu_o} \qquad \eta_o = \sqrt{\frac{\mu_o}{\varepsilon_o}}$$

$$\varepsilon_o = 8.854 \times 10^{-12}\ \text{F/m} \qquad \mu_o = 4\pi \times 10^{-7}\ \text{H/m}$$

The total amount of electromagnetic power that is radiated by the bulk acoustic wave resonator into the upper half plane is equal to

$$P_{rad} = \frac{1}{\eta_o}\int_0^{2\pi}\int_0^{\pi/2} \left|\hat{\theta}\, E_\theta + \hat{\varphi}\, E_\varphi\right|^2 r^2 \sin\theta\, d\theta\, d\varphi \qquad (10)$$

RESULTS

Consider the electrically small resonator shown in Figure 1. From Eqs. (8,9) the Fourier transforms are

$$\tilde{K}_x(u,v) = \frac{V}{ju}\,(1 - e^{jvb})\,(1 - e^{jua}) \qquad (11)$$

$$\tilde{K}_y(u,v) = -\frac{V}{jv}\,(1 - e^{jvb})\,(1 - e^{jua}) \qquad (12)$$

For the case of a rectangular resonator, the radiated far fields may be written in closed form as a function of the impedance of the device. Examining Eq. (5), one would expect a drop in the radiated power at series resonance and an increase in the radiated power at parallel resonance.

To verify this, 5cm by 5cm bulk acoustic wave resonators were fabricated on 3 inch AT-cut quartz and Z-cut lithium niobate wafers. The quartz and lithium niobate wafers are 11.5mil and 19.1mil thick respectively, and the metalization is 0.9 microns of aluminum. The back side of the wafers are completely metalized, and the resonators are patterned on the front side. To apply the theory, the resonators were considered one dimensional and the input impedance was estimated with the Mason model [6]. The predicted total radiated power from the resonators for a 10V-50ohm source is plotted in Figures 4 and 5. The analysis was done for the fundamental thickness mode resonance of the quartz device and the first overtone thickness mode resonance of the lithium niobate resonator. Note that for both cases, the theory predicts a decrease in the

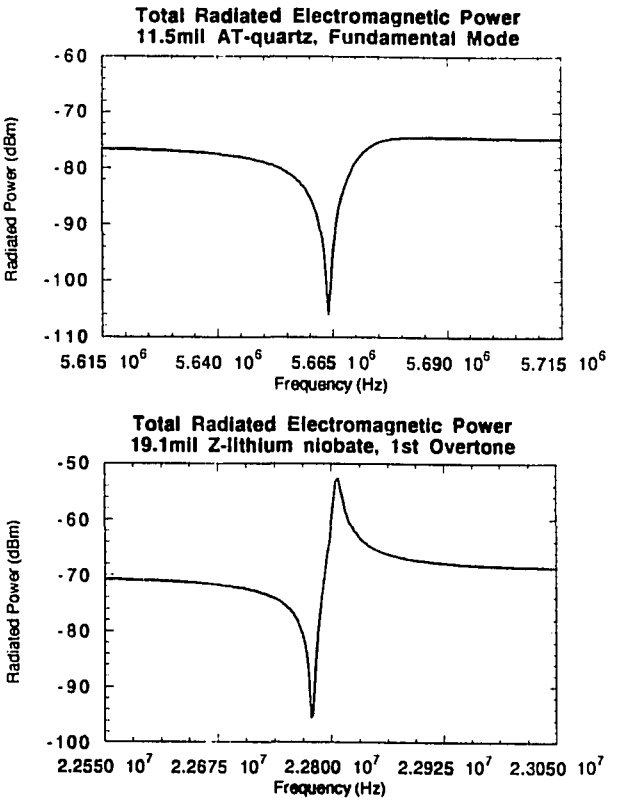

Figures 4-5

radiated power at series resonance and an increase in the radiated EM power at parallel resonance. Viscous damping loss was included in the calculation by the use of a complex elastic constant

$$\hat{c} = c + j\omega\eta$$

where an estimate of the viscosity is obtained from the reported attenuation constants for quartz and lithium niobate [6,9].

To experimentally verify the theoretical results, the devices were driven by an HP8753A network analyzer, and the radiated power was picked up by an AM loopstick antenna. The AM antenna is connected to an HP3585A spectrum analyzer that is set in a peak hold mode so that the detected power may be displayed as a function of frequency. The goal of this experiment was to verify the shape of the radiation spectrum predicted by theory and not to attempt to measure the total power radiated by the resonator. What is predicted by theory is the total power radiated by the device when the Poynting vector has been integrated over the entire upper half space. For the experimental results, just the power picked up by the AM antenna is plotted. Thus, the absolute magnitude of the measured power spectrums cannot be compared with what is predicted by the theoretical calculation.

Shown in Figure 7 is the measured radiated EM power for the quartz resonator near the fundamental thickness mode. The radiated power from the lithium niobate device near the first overtone of the thickness mode is plotted in Figure 8. In both cases the radiated power drops off at series resonance and increases at parallel resonance. For the measurements, the output power of the network analyzer was set to 23dBm in order to get the detected signal level well above the noise floor of the spectrum analyzer. The measured radiated power spectrum is in excellent agreement with the theoretical computation with the exception of the spurious lateral modes which will not be predicted by the Mason model. Also consistent with the theoretical results is the relative magnitude of the radiated power increase at parallel resonance which is large for the lithium niobate device and small for the quartz device.

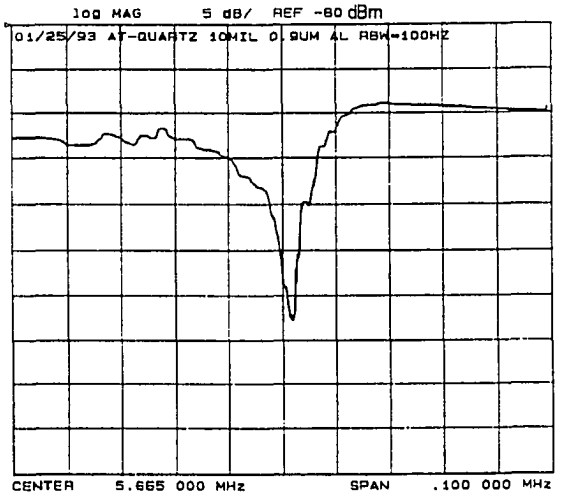

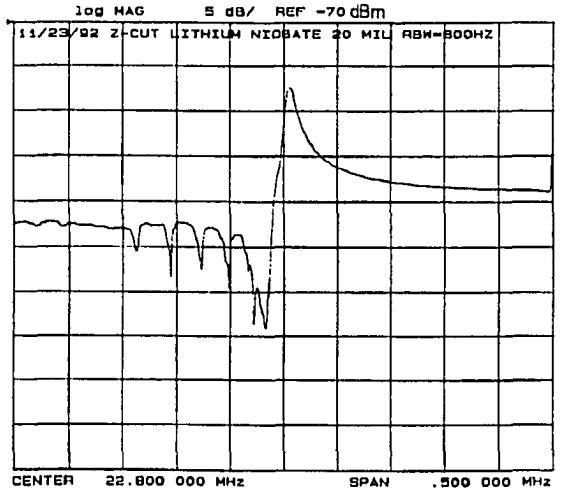

Figures 7-8

CONCLUSIONS

A technique for the calculation of the radiated electromagnetic power from electrically small BAW resonators has been presented. The method is valid for general BAW resonators as long as the impedance of the device is available. The theoretical results for the radiation spectrum were experimentally verified for AT-cut quartz and Z-cut lithium niobate resonators, and good agreement was obtained between experiment and theory for the shape of the radiation spectrums.

ACKNOWLEDGEMENTS

This work was supported by a U. S. Dept. of Commerce grant through the Center for Advanced Technology Development, and the Department of Electrical Engineering and Computer Engineering, Iowa State University. The graduate student was supported by a U. S. Dept. of Education Fellowship. The authors would also like to thank Crystal Technology,Inc. and P.R. Hoffman Materials Processing Corp. for supplying the lithium niobate and quartz wafers.

REFERENCES

[1] K. M. Lakin, "Modeling of Thin Film Resonators and Filters." *1992 IEEE MTT-S International Microwave Symposium*, pp. 149-152.

[2] P. C. Y. Lee, "Electromagnetic Radiation from an AT-Cut Quartz Plate Under Lateral Field Excitation." *IEEE 1988 Ultrasonics Symposium*, pp. 407-411.

[3] P. C. Y. Lee, Y. G. Kim, and J. H. Prevost, "Electromagnetic Radiation from Doubly Rotated Piezoelectric Crystal Plates Vibrating at Thickness Frequencies." *IEEE 1989 Ultrasonics Symposium*, pp. 423-428.

[4] R. D. Mindlin, "Electromagnetic Radiation From a Vibrating Quartz Plate." *Int. J. Solids Structures*, 9, pp. 697-702, 1972.

[5] W. L. Stutzman, and G. A. Thiele, *Antenna Theory and Design*. New York: John Wiley & Sons, 1981.

[6] J. F. Rosenbaum, *Bulk Acoustic Wave Theory and Devices*. Boston: Artech House, 1988.

[7] C. A. Balanis, *Advanced Engineering Electromagnetics*. New York: John Wiley & Sons, 1989.

[8] Y. T. Lo, and S. W. Lee, *Antenna Handbook*. New York: Van Nostrand Reinhold Co., 1988.

[9] B. A. Auld, *Acoustic Fields and Waves in Solids*. Vol. I - Vol. II. Malabar, Florida: Robert E. Krieger Publishing Co., 1990.